Fluctuations and Interactions of Brownian particles in multiple Optical Traps

Antoine Bérut

N° National de Thèse : 2015ENSL1003

THÈSE

en vue de l'obtention du grade de

Docteur de l'Université de Lyon,
délivré par l'École Normale Supérieure de Lyon

Discipline : **Physique**

Laboratoire de Physique de l'ENS de Lyon

École Doctorale de Physique et d'Astrophysique de Lyon

Présentée et soutenue publiquement le 7 juillet 2015
par **M. Antoine BÉRUT**

Fluctuations and Interactions of Brownian Particles in Multiple Optical Traps

---

Directeur de Thèse : M. Sergio CILIBERTO

Devant la commission d'examen formée de :

Monsieur	Sergio CILIBERTO	*CNRS*	Directeur
Monsieur	Massimiliano ESPOSITO	*Université du Luxembourg*	Rapporteur
Madame	Elisabeth GUAZZELLI	*CNRS*	Examinatrice
Monsieur	François LADIEU	*CEA*	Rapporteur
Monsieur	Artyom PETROSYAN	*CNRS*	Co-encadrant
Monsieur	Ken SEKIMOTO	*Université Paris VII*	Examinateur

Laboratoire de Physique
École Normale Supérieure de Lyon
46, allée d'Italie
69007 Lyon

École doctorale de Physique et
Astrophysique de Lyon
4, Rue Enrico Fermi
69622 Villeurbanne Cedex

Acknowledgements

I first would like to thank the English speaking reader who will forgive me for writing my acknowledgements in French.

Je voudrais d'abord remercier mon directeur de thèse Sergio Ciliberto pour son encadrement durant ces trois années. Son enthousiasme et ses très vastes compétences scientifiques ont permis de donner une direction à mon travail et de me motiver à continuer même lorsque des problèmes surgissaient. Je veux également remercier mon co-encadrant Artem Petrosyan, qui m'a continuellement accompagné et m'a apporté ses multiples connaissances expérimentales ainsi que de nombreux conseils. Je tiens à leur exprimer toute ma gratitude à tous les deux pour leur disponibilité et pour la confiance qu'ils m'ont accordée tout au long de ma thèse.

Je remercie ensuite toutes les personnes qui m'ont apporté leur aide à différentes étapes de ma thèse. Artak Arakelyan pour avoir recodé en C l'algorithme de traitement d'image qui nous a permis de gagner un temps précieux dans l'analyse des données. Eric Lutz et Raoul Dillenschneider pour leur aide sur le principe de Landauer. David Lacoste et Christian Van den Broeck pour m'avoir aiguillé sur les égalités de Jarzynski généralisées qui ont permis d'interpréter les résultats expérimentaux. Krzysztof Gawędzki pour son travail sur la procédure optimale d'effacement de l'information. Ruben Gomez-Solano pour ses réponses à mes questions sur un travail vieux de plusieurs années. Denis Bartolo pour son aide concernant la microfluidique. Céleste Odier pour le temps conséquent qu'elle a passé à m'aider pour tenter de réaliser un canal microfluidique parfait. Et enfin Alberto Imparato pour son aide sur les résolutions d'équations de Fokker-Planck.

Je remercie également Massimiliano Esposito, François Ladieu, Elisabeth Guazzelli et Ken Sekimoto pour avoir accepté de faire partie de mon jury de thèse, pour leur lecture attentive de mon manuscrit et les intéressantes discussions qui en ont suivi.

Je suis aussi reconnaissant envers de très nombreuses personnes (j'espère ne pas en oublier) qui ont contribué par leur sympathie et leur bonne humeur à faire de ces trois années au laboratoire une expérience agréable. Les membres (parfois temporaires) de l'équipe : Antoine Naert, Ludovic Bellon, Audrey Steinberger, Caroline Crauste, Justine Laurent, Tianjun Li, Felipe Aguilar Sandoval, Ignacio Martinez, Isaac Theurkauff, Denis Cottinet, Mickaël Geitner, Anne Le Cunuder et Clémence Devailly. Mes différents co-bureaux (qui n'ont pas tous partagé mon bureau simultanément malgré le manque de place au laboratoire) : Clémence à nouveau, Robin Guichardaz, Maxime Champion, Pierre Lidon, Michel Fruchart et Christophe Brouzet. Le gang des thésards qui vont manger à la cantine à 11h42 pour éviter la queue (méthode brevetée, fonctionne dans au moins 50 % des cas) : David Lopes Cardozo, Etienne Thibierge, Arnaud Baguet, Daniele Malpetti, Christoph Charles, Clément Tauber, Irénée Frérot, Jean-Yonnel Chastaing,

Jean-Baptiste Caussin, Timothée Verdier, et à nouveau Michel, Robin, Maxime, Pierre et Céleste. Ainsi que tous les autres membres du laboratoire, et en particulier Julien Bernaud qui a souvent manipé dans la même salle que moi, et Sylvain Joubaud, Eric Freyssingeas, Jeremy Ferrand, Cendrine Faivre-Moskalenko et Valérie Vidal avec qui j'ai donné des TD d'optique pour mon monitorat. Merci à tous pour les nombreuses conversations scientifiques (ou non) que nous avons pu avoir.

Je voudrais également exprimer une petite pensée à tous les professeurs que j'ai pu avoir pendant ma scolarité, et qui ont sans doute tous un peu contribué à me faire aimer les sciences et à continuer mes études.

Le nombre de pages n'étant pas limité, je remercie chaleureusement David, Loren, Mickaël, Charlotte, Thibaut, Bérénice, Marion et Pierre-Marie (même si ce dernier ne répondait pas aux mails) pour leur amitié. Je remercie également Clément, Florent, Baptiste, Adrien, Sofiane, Dorian et Axel pour les nombreux bons moments que nous avons passé devant des jeux vidéo ou de société (malgré leur aversion souvent injustifiée pour les personnages que je choisis). Ainsi que le Pr. Chen pour m'avoir fait confiance en l'an 2000 pour mener à bien la classification des différentes espèces vidéoludiques de Kanto.

Je remercie enfin mes parents Marc et Annie qui m'ont toujours encouragé et laissé choisir la voie que je voulais pendant mes études, ma sœur France avec qui j'ai grandi, ainsi que Sophie pour tous les moments que nous vivons ensemble et pour avoir consciencieusement relu mon manuscrit alors qu'elle est biologiste de formation.

Abstract/Résumé

English:

We experimentally study the fluctuations of Brownian micro-particles trapped with optical tweezers arranged in various spatial configurations. We give a general description of the experimental set-up and detail four different experiments we conducted. We first use a single particle in a double-well potential to model a two-state memory system. We verify the Landauer principle on the minimal energetic cost to erase one bit of information at the quasi-static limit, and we use a detailed version of a fluctuation theorem to retrieve the expected energetic bound at any speed of the memory erasure procedure. We then use two particles in two different traps to study the hydrodynamic interactions between two systems kept at different effective temperatures. Contrary to what was previously observed, we show that the sol-gel transition of gelatine does not provide any anomalous fluctuations for the trapped particle when the sample is quenched below gelification temperature. Therefore, this system is not a good candidate to study effective temperatures. We show however that an effective temperature is created when a well chosen random noise is added on one trap position. We demonstrate that the random forcing on one particle induces an instantaneous correlation between the two particles motions, and an energy exchange from the virtually hot particle to the cold one, which is in equilibrium with the thermal bath. We show a good agreement between the experimental data and the predictions from an hydrodynamic coupling model. Finally, we describe the use of microfluidic channels to create a shear flow at the micron size, and we discuss the possibility to interpret the force due to the shear flow in terms of an effective temperature by testing a fluctuation-dissipation relation.

Français :

Nous avons étudié expérimentalement les fluctuations de micro-particules browniennes piégées à l'aide de pinces optiques dans un réseau de puits de potentiels voisins. Nous donnons un descriptif général du montage expérimental, puis détaillons quatre utilisations différentes du système. Nous avons d'abord utilisé une unique particule dans un double puits de potentiel pour modéliser un système mémoire à deux niveaux, avec lequel nous avons vérifié le principe de Landauer sur le coût minimal en énergie pour l'effacement d'un bit d'information, dans la limite quasi-statique. Nous avons également appliqué une version détaillée d'un théorème de fluctuation à la procédure d'effacement de l'information pour retrouver la limite énergétique attendue, quelle que soit la vitesse de la procédure d'effacement de l'information. Nous avons ensuite étudié l'interaction hydrodynamique entre deux particules dont l'une est soumise à une température effective. Nous avons montré qu'il n'y a pas de fluctuations anormales lors de la transition sol-gel de la gélatine, contrairement à ce qui avait été observé précédemment, et que ce système ne pouvait donc pas être utilisé pour étudier des températures effectives. En revanche, nous avons montré que l'ajout d'un forçage aléatoire bien choisi sur la position d'un piège créait une température effective pour la particule piégée. Nous avons montré qu'un tel forçage d'une des particules était à l'origine d'une corrélation instantanée des mouvements des deux particules, et s'accompagnait d'un échange de chaleur de la particule virtuellement chaude à la particule froide en équilibre avec le bain thermique. Nous avons obtenu un bon accord entre les données expérimentales et les prédictions d'un modèle de couplage hydrodynamique. Enfin, nous décrivons l'utilisation de canaux microfluidiques pour réaliser un écoulement cisaillé à l'échelle micrométrique, et nous discutons de la possibilité d'interpréter un cisaillement en terme de température effective en testant une relation de fluctuation-dissipation.

Contents

Introduction

At the micro-scale, thermal agitation plays an important role. Even when a fluid is at rest from the macroscopic point of view, its microscopic molecules are constantly moving in random directions. For example, in a still glass of water at room temperature the water molecules have an average instantaneous speed of $\sim 500\,\mathrm{m}\cdot\mathrm{s}^{-1}$. This effect is visible on bigger scales as any object immersed in a fluid may be shifted by the collisions with the fluid's molecules. As a consequence, any immersed particle will randomly diffuse in the fluid, if its size is not too big compared to that of the fluid's molecules (typically a few Å). An example of such a diffusion is shown in figure 1. It represents the 2D positions of the center of mass of a 1 µm-radius sphere in water at room temperature, recorded for 10 s.

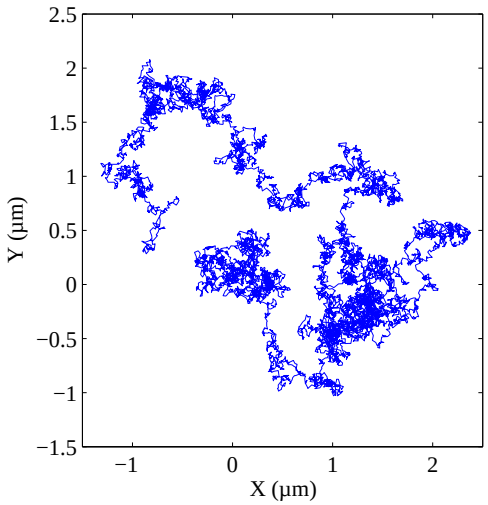

Figure 1: Example of the 2D displacement of a spherical particle (radius $R = 1\,\mu\mathrm{m}$), in water at room temperature. The trajectory is 10 s long, with an aquisition rate of 1000 Hz.

This effect has been known for a very long time: in "De rerum natura", the Roman poet Lucretius already noted that tiny dust particles suspended in air move in multiple directions in the absence of macroscopic flow [1]. In 1828, Robert Brown observed with a microscope the random motion of pollen grains suspended in water [2]. At the beginning of the twentieth century, what is now called "Brownian motion", was studied by physicists like Einstein [3], Smoluchowski [4], Langevin [5] and Perrin [6]. They have shown (among other things) that the

motion of a free Brownian particle can be characterised by a diffusion coefficient D:

$$\langle x(t)^2 \rangle = 2Dt \tag{1}$$

where x is one position coordinate of the particle, t is the time (at $t = 0$ the position is chosen to be $x = 0$), and $\langle . \rangle$ is an ensemble average (*i.e.* an average over several realisations of the same diffusion process).
Moreover, this diffusion coefficient is directly linked to the thermal fluctuations of the fluid:

$$D = \frac{k_{\mathrm{B}}T}{6\pi R\eta} \tag{2}$$

where k_{B} is the Boltzmann constant, T the temperature (in kelvins), R the particle's radius, and η the viscosity of the fluid. Even today, more than a century after these works, Brownian motion is still an active field of theoretical and experimental research. In particular, new experimental tools as optical tweezers or atomic-force microscopes now allow for controlling devices at the micro or nano-scale, and have meet an increasing interest in the past twenty years. Simultaneously, important theoretical results have been achieved in the field of out-of-equilibrium statistical physics and have opened the way to a thermodynamic approach in micro-systems where thermal fluctuations cannot be neglected.

In this thesis, we have studied the fluctuations and interactions of 1 µm silica particles manipulated with optical traps. We were motivated by the experimental possibility to use "multiple traps". It allows us to trap several particles in various configurations, that can be linked to various theoretical questions. The manuscript is organised as follow:

1. In the first chapter we introduce some useful experimental and theoretical background. We describe the physics of optical trapping, and our experimental set-up. We recall the Langevin equation used to describe the Brownian motion of a trapped particle, definitions of work and heat from the stochastic energetics framework, the Fluctuation-Dissipation Theorem and some formulations of Fluctuation Theorems.

2. In the second chapter we test the Landauer's principle that predicts the minimal energetic cost of erasing one bit of information. We use a single particle in a double trap to mimic a 1-bit memory system. By applying an external force, we realise a memory-erasure procedure, and we measure the heat dissipation associated with this logically irreversible process. We also use a Fluctuation Theorem to directly extract the free-energy change associated with the procedure.

3. In the third chapter, we explain why gelatin is not a good candidate to trap two nearby particles with different effective temperatures. We trap a single particle in gelatin that is undergoing sol-gel transition. We show that the previously observed anomalous high fluctuations, that could be interpreted as an effective temperature, are not reproducible. In particular, we verify that the Fluctuation-Dissipation Theorem is not violated in such a system.

4. In the fourth chapter we study the hydrodynamic interactions of two particles trapped nearby, when one of them is randomly forced so that it shows an effective temperature. We measure the particles positions correlation functions and find a good agreement with predictions from an analytic model. We also measure the distributions of heat and work exchanged between the particles and try to interpret them with an exchange Fluctuation Theorem.

5. Finally, in the fifth chapter, we try to use a shear-flow to create an effective temperature on one trapped particle. We describe the microfluidic set-up used to create a shear-flow at the micro-scale as well as a way to mimic an "effective" shear-flow with controlled optical traps. We present some preliminary results that show a clear violation of the Fluctuation-Dissipation Theorem for this system.

Chapter 1

Experimental and Theoretical Background

La notion de passoire est indépendante de la notion de trou.

Pr. Shadoko

In this chapter we give a brief overview of the physics of optical tweezers, we describe our experimental set-up, we present the framework of stochastic thermodynamics and we recall several results from (out-of) equilibrium statistical physics that will be useful throughout the Thesis.

1.1 Optical tweezers

1.1.1 Theory

Optical traps (also called optical tweezers) allow for trapping and manipulating dielectric particles, with sizes from $\sim 10\,\mu m$ to $\sim 10\,nm$, thanks to the radiation pressure exerted by light on matter. The first experimental realisation was done by Ashkin in 1969 [7], using two counter-propagating laser beams to trap micron-sized particles. Then the technology evolved rapidly and successfully, and optical tweezers are nowadays widely used scientific tools, especially in fields like biology, colloids physics and microfluidic [8, 9].

When a laser beam with wavelength λ goes through a transparent particle, with a refractive index n_b greater than that of the surrounding medium n_a, the particle senses two forces:

- The scattering force, which is proportional to the beam intensity, pushes the particle in the direction of light propagation.
- The gradient force, which is proportional to the gradient of intensity, pushes the particles toward the regions of high intensity.

In the limit case where the particle is big compared to the wavelength (Mie regime), this effect can simply be understood using geometrical optics. The refraction and reflection of the rays directly indicate the momentum transferred to the particle. A schematic representation is shown in figure 1.1. The light propagates along the z direction. The orange profile is the distribution of light intensity in the x direction. The black lines (α, β and γ) are directions

of propagation of light rays refracted at the interfaces between the sphere and the surrounding medium. For the α ray the black dashed-lines indicate directions of the light rays reflected at the interfaces, the red arrows (F_{D1} and F_{D2}[1]) are forces due to the refracted rays, and the green arrows (F_{R1} and F_{R2}) are forces due to the reflected rays. For the γ ray, the forces (not represented) are simply obtained by symmetry, but have a smaller amplitude than for the α ray, because the intensity is smaller in the lower half than in the upper half of the bead. In the end, the bead senses a force in the direction of light propagation z and a force in the x direction toward the region of maximal intensity.

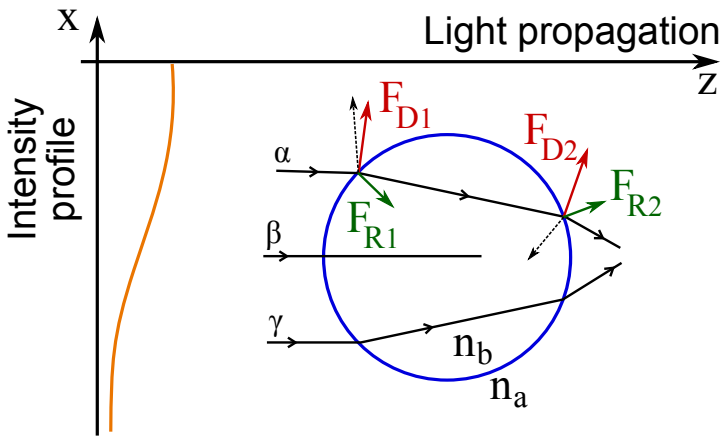

Figure 1.1: Schematic representation of the forces acting on a Mie dielectric sphere lit by a laser beam (image reproduced from [7]). The refractive index of the bead n_b is greater than the one of the surrounding medium n_a.

In the limit where the particle is small compared to the wavelength (Rayleigh regime), the forces can be computed by treating the particle as a point dipole [10]:

$$F_{\text{scattering}} = \frac{I_0}{C}\frac{128\pi^5 R^6}{3\lambda^4}\left(\frac{m^2-1}{m^2+2}\right)^2 n_a \tag{1.1}$$

where I_0 is the intensity of the laser beam, R is the particle radius, $m = n_b/n_a$ is the "effective index", and C the speed of light,

$$F_{\text{gradient}} = \frac{2\pi\alpha}{C{n_a}^2}\nabla I_0 = \frac{2\pi R^3}{C}\left(\frac{m^2-1}{m^2+2}\right)\nabla I_0 \tag{1.2}$$

where α is the particle's polarizability.

The early set-ups used mostly the scattering force to trap one particle, by pushing it against another laser [7], against a wall, or against gravity [11]. In 1986 Ashkin and co-workers used a highly focused beam (with a high numerical aperture microscope objective), so that the gradient force exceeds the scattering force and the particle could be trapped with a single laser beam [12]. In this configuration, near the focal point, the intensity gradient counterbalances the radiation pressure pushing the particle in the direction of light propagation, and the particle is trapped. A schematic representation with geometrical optics is shown in figure 1.2. We use the same principle in our optical trap set-up.

[1] "D" stands for "deflection".

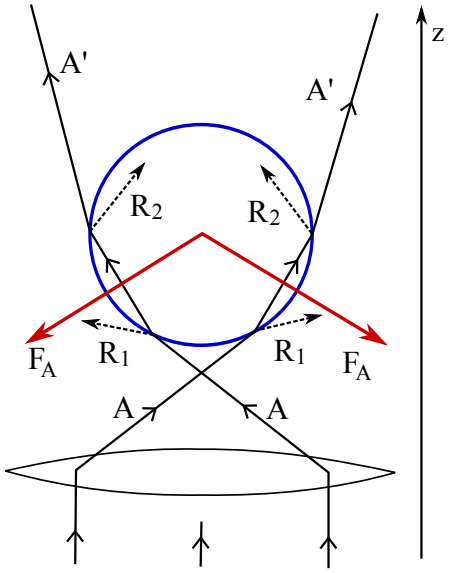

Figure 1.2: Schematic representation of Mie dielectric sphere trapped with a highly focused laser beam (image reproduced from [12]). The refractive index of the bead n_b is greater than the one of the surrounding medium n_a. The bead is attracted toward the focal point, even though the radiation pressure tends to push it in the direction of light propagation z.

For small displacements, the trap imposes a harmonic restoring force to the particle:

$$\vec{F}(x,y,z) = -k_x\, x\vec{e}_x - k_y\, y\vec{e}_y - k_z\, z\vec{e}_z \tag{1.3}$$

where $\vec{r} = (x,y,z)$ is the displacement of the particle with respect to the position of the trap (which is the equilibrium position of the particle), and the k_i ($i \in \{x,y,z\}$) are the trap's stiffnesses in different directions. The force is typically in the piconewton range and is proportional to the beam's intensity I_0. Its exact value depends on the beam and particle shapes. Usually, the stiffnesses in the transverse directions x and y are equal, but the stiffness in the direction of light propagation z is smaller. Due to the scattering force or external forces like gravity, the position of the trap may not be exactly the focal point.

In the Mie regime the force does not depend on the R radius of the bead, but in the Rayleigh regime the force is proportional to R^3 [13]. Some experimental forces measurements are presented in [14]. Calculations of the gradient force for any size of particle are presented in [15]. For example, for a symmetric Gaussian beam $I(r) = I_0\exp(-r^2/2w_0^2)$, the gradient force is given by:

$$F(r) = 4\pi\alpha I_0 w_0^2 \exp\left(-\frac{R^2+r^2}{2w_0^2}\right)\left[\frac{Rr}{w_0^2}\cosh\left(\frac{Rr}{w_0^2}\right) - \sinh\left(\frac{Rr}{w_0^2}\right)\right] \tag{1.4}$$

where w_0 is the beam waist, and $r = \sqrt{x^2+y^2+z^2}$. When the displacement is small enough, it can be rewritten $F(r) = -kr$ with the stiffness:

$$k = \frac{4\pi\alpha I_0}{3w_0^2} R^3 \exp\left(-\frac{R^2}{2w_0^2}\right). \tag{1.5}$$

In practice, it is often easier to calibrate the optical trap by measuring directly the force or trapping potential than measuring the values necessary to compute the theoretical expression. In the following sections we describe our experimental set-up, including the calibration techniques.

1.1.2 Sample preparation

The particles we use are *Polyscience Inc.* silica micro-spheres of radius $R = 1.00 \pm 0.05\,\mu m$. The commercial aqueous solution has a concentration of $10^{10}\,\text{particle} \cdot \text{mL}^{-1}$. We usually dilute it in bidistilled water to reduce the concentration down to $\sim 10^{6}\,\text{particle} \cdot \text{mL}^{-1}$ before using it.

The particle solution is contained inside a disk shaped glass cell which is designed to be used in our custom-built optical tweezers set-up (described in the next subsection). The cell, schematically represented in figure 1.3, is made from a microscope slide and a glass coverslip of thickness No. 1 (0.13 to 0.16 mm). Two holes, used to fill the cell, are drilled in the microscope slide.

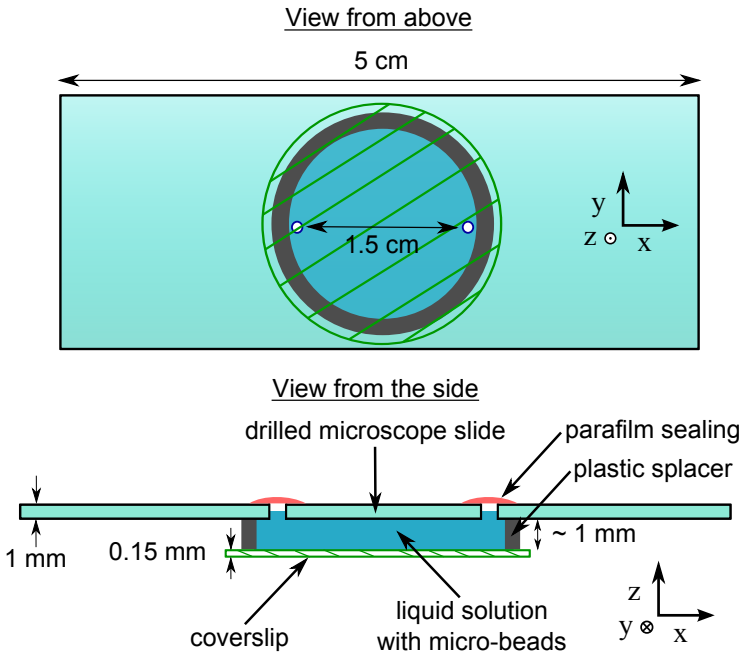

Figure 1.3: Schematic representation of disk-shape cells used to contain the micro-particles solution.

The cell is built using the following protocol:

- Two holes separated by $\sim 1.5\,\text{cm}$ are drilled in a microscope slide.
- A circular plastic spacer is glued on the surface of the slide using UV-curing *Norland Optical Adhesive 81* (NOA-81).
- The open cell is cleaned in an ultrasonic cleaner, using bidistilled water with Micro-90® cleaning solution as a solvent. The cell is carefully rinsed with bidistilled water and dried with a compressed air flow.

- A coverslip is cleaned using isopropyl alcohol (IPA) and glued to the plastic spacer using NOA-81.
- The cell is filled with micro-spheres solutions introduced by a micropipette in one of the holes. To avoid sedimentation of the particles, the solution is agitated before being introduced in the cell.
- The holes are sealed using Parafilm M®. A small piece of parafilm is put over each hole, and attached to the glass surface with the use of a soldering iron.

Usually the cells are put under a UV-lamp for a few hours after being sealed, to avoid the presence of bacteria inside. Once the cell is sealed, it can be kept for a few weeks before the fluid starts to evaporate significantly. The cells are reusable: it is easy to remove the parafilm sealing and the coverslip to recover an empty open cell.

The particles have a greater density than water and rapidly fall to the bottom of the cell. They usually do not sediment completely because their surface is slightly charged negatively and is repulsed by the negative charge of the cell's glass surfaces. The particles are small enough to acts like Brownian particles [2] and show a random motion resulting from their collision with the molecules of water. Hence, in the absence of trapping, the particles freely diffuse in the bottom plane of the cell.

If we want a region with a small depth where the fraction of particles will be very low, we can add a glass step in the central region of the cell, as described in chapter 2. If we want to work with a thermoreversible gel, we can use a microscope slide coated with Indium Tin Oxide (ITO). The ITO coating is electrically conductive and allows us to heat the cell thanks to Ohm's law, as described in chapter 3.

1.1.3 Experimental set-up

During the Thesis, we used different variations of the same experimental set-up. We describe here their common base that is used to create several optical traps with a chosen configuration, and the details of each variation are given in the following chapters.

Trap controlled by an acousto-optic deflector

To create an optical trap, we use a Gaussian laser beam that is enlarged with the use of a telescope and sent in a microscope objective with a high numerical aperture. The microscope objective is an oil-immersion *Leica* HCX PL. APO ×63 with numerical aperture 1.4. The cell is placed on a translational stage (in three directions xyz) and is approached to the microscope objective with a droplet of immersion oil (*Leica* "type F"). The particles are trapped near the focal point, where the intensity of the laser is maximal. Note that the particles have a size comparable to typical laser wavelengths, and cannot be considered to be in the Mie or Rayleigh approximation when they are trapped.

To control the position of the trap, the laser beam goes through an acousto-optic deflector (AOD) from *AA Opto-Electronic*. The physical principle is the following: a radio frequency signal is applied to a piezo-electric transducer, bonded to a suitable crystal. It generates an acoustic wave that travels through the crystal at the acoustic velocity of the material and with an acoustic wavelength dependent on the frequency of the signal. This acoustic wave acts as a "phase grating" and the incident laser beam is diffracted by this grating. Thus, by controlling

the frequency of the signal sent to the AOD, we control the deflection angle of the first order diffracted beam. For a parallel beam, an angle of incidence corresponds to a position in the focal plane of the microscope objective. Hence, controlling the frequency of the driving signal sent to the AOD allows us to shift the position of the trap in the focal plane. Note that to shift the trap in both transverse directions x and y, one needs to use two orthogonal AODs.

We have three AOD devices, two to be used with a $\lambda = 1064\,\text{nm}$ laser, and one to be used with a $\lambda = 532\,\text{nm}$ laser. Both AODs work with driving signals of frequencies around 80 MHz. Their efficiency[2] is about 80 % for the central frequency and do not evolve rapidly with the drive frequency. They enable us to rapidly change the position of the trap in the focal plane (up to 1 MHz). The driving signal is created by a 100 MHz arbitrary function generator from Tektronix®, and its frequency is controlled by a computer generated signal.

To create multiple independent optical traps, we switch rapidly the laser between several focal positions, thanks to the AOD. If the switching is fast enough, each trapped particle does not have enough time to diffuse away from its trap's position during the time when the laser is in others trap's positions. This technique allows us to trap up to ~ 8 particles with the possibility to change the traps configuration at a high speed. The other usual method to create multiple traps is the use of holographic tweezers [16–18], which allow for more complex geometries but are limited by a refreshing rate of a few tens of Hz.

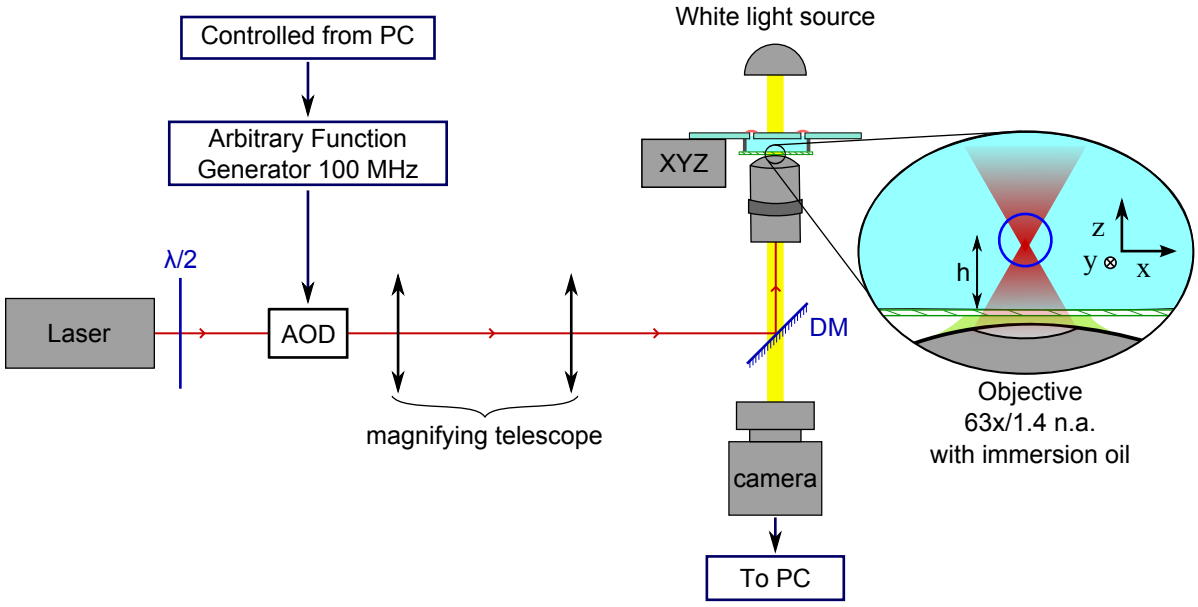

Figure 1.4: Schematic representation of the optical traps set-up used to trap one or several silica micro-beads. The acousto-optic deflector (AOD) allows to change very rapidly the position of the laser focal point where the particle is trapped. The half-wave plate ($\lambda/2$) is used to tune the beam's direction of polarisation. "DM" is a dichroïc mirror.

A schematic representation of the set-up is shown in figure 1.4. The particles are usually trapped at a distance $h \sim 20\,\mu\text{m}$ from the bottom of the cell. Since the particles are trapped

[2]The efficiency is the ratio of intensity in first diffracted order and intensity in the zero$^{\text{th}}$ order without applied frequency.

near the focal point of the microscope objective, we can use the same microscope objective to visualise their motion.

Particle tracking

The particle's motion can be tracked directly using the image of the focal plane seen through the microscope objective. For this purpose, we use a fast *DALSA* camera able to record small images at rate of 1600 Hz. To avoid storing huge film files, we made a Labview® program with an implementation in C++ of the tracking algorithm from Daniel Blair and Eric Dufresne [19]. The algorithm is an adaptation of the IDL Particle Tracking software developed by David Grier, John Crocker and Eric Weeks [20] which is described in article [21]. With this program we can do "real-time" tracking and save only the coordinates x and y of several particles over the time.

Another way to track one particle's motion, is to use a Position Sensing Diode (PS diode) *DL100-7-PCBA3*. The principle is the following: for a laser beam, the trapped micro-bead of radius R acts as a lens of focal $f_1 = mR/2(m-1)^2$, with m the effective index ($m = n_{\text{bead}}/n_{\text{medium}}$). Hence, if the particle moves, it will change the direction in which the beam is deflected after the bead. Experimentally, we add a second laser beam, which is aligned with the trapping laser and focused close to its focal point, and we detect the position of this laser on the PS diode after an array of lenses. A schematic representation is shown in figure 1.5. The PS diode measures the relative displacement of the laser spot's centroid with respect to its own centroid. The optical system is aligned so that in the absence of bead, the laser spot is centred on the PS diode. When a bead is trapped, its fluctuations in the xy plane are recorded by the deflections of the beam on the PS diode at a rate up to 20 kHz.

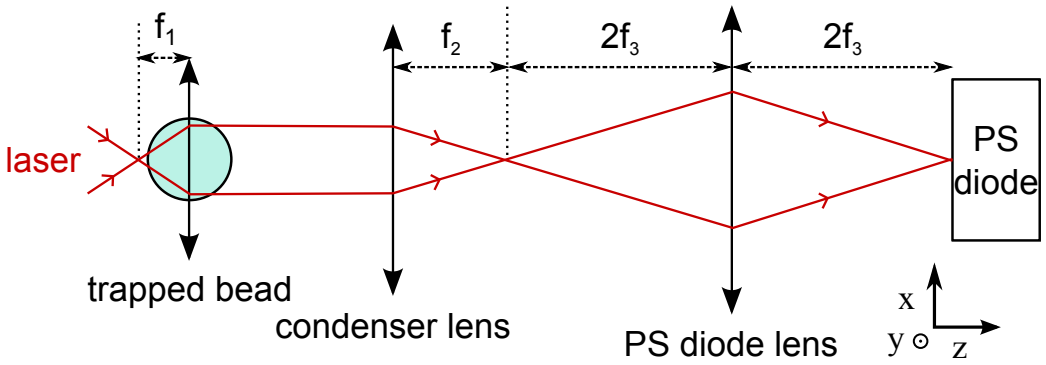

Figure 1.5: Schematic representation of the optical path of the laser beam going through the bead and detected by the position sensing diode (PS diode). For the experimental set-up, $f_2 = 23$ mm and $f_3 = 35$ mm. Only the detection laser in represented, the bead is trapped by another laser, which is filtered by a dichroïc mirror before reaching the PS diode.

Even if the PS diode allows for higher acquisition frequencies, we mostly used the camera tracking. The advantages of using a camera are the following:

- It is easy to convert pixels to micrometers by using a calibration target and the beads displacements can directly be measured in µm. Conversely, the PS diode only gives a signal in volts which requires a more complex calibration that needs to be done for each particle trapped.

- It is easy to track several particles with the camera, whereas it requires complex optical set-ups with the PS diode.

1.1.4 Calibration techniques

In this section we describe the calibration used to measure the trap's stiffness k. For simplicity reasons, we consider only the displacement in the direction x, but the analysis can easily be extended to a motion in the plane xy.

Potential measurement

If the coordinates of the particles are measured directly in physical units (µm), one simple way to visualise the trapping potential $U(x)$, is to compute the equilibrium distribution of positions $P(x)$. Indeed, at equilibrium $P(x)$ verifies the Boltzmann distribution:

$$P(x) \propto \exp\left(-\frac{U(x)}{k_B T}\right) \tag{1.6}$$

where k_B is the Boltzmann constant, and T the equilibrium temperature of the fluid in kelvins. Then a polynomial fitting of the distribution logarithm, directly gives the potential in $k_B T$ units.

An example of potential, compared with a quadratic fit ($U(x) = kx^2/2$) is shown in figure 1.6a. When the set-up is correctly adjusted[3], the agreement is excellent.

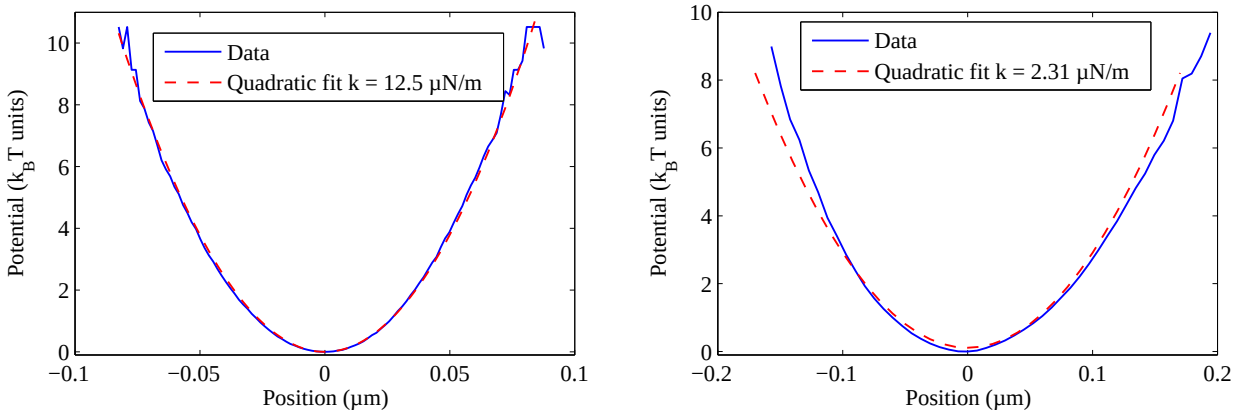

(a) A single trap

(b) One of two traps created by an AOD

Figure 1.6: Potentials measured by equilibrium position distribution estimation, for particles trapped in water at room temperature ($\sim 23\,°C$). a) For a single trap. The quadratic fit has a very good agreement with the data (here $k = 12.5\,\mathrm{pN/\mu m}$). b) For one of the two traps created by a single laser beam switched between two positions thanks to an acousto-optic deflector (AOD). The potential is a bit asymmetric and the agreement with the quadratic fit is not very good (here $k = 2.31\,\mathrm{pN/\mu m}$).

Note that when the position of the trap is switched between several positions by the acousto-optic deflector (AOD), the shape of the potentials is always a bit asymmetric, as shown in

[3]The laser beam must be parallel and well centred with regard to the microscope objective.

figure 1.6b. It can be understood as an effect of the finite time needed to displace the beam between the two positions: there is a residual laser intensity between the two traps, which modifies the trapping potentials.

There are more complicated methods to directly measure the trapping potential (for example the one described in [22]), but this one is sufficient for simple potential shapes and only requires a long (*i.e.* a few ~ 100000 points) equilibrium measurement.

Spectral analysis

An usual method of calibration consists in measuring the Power Spectral Density (PSD) of the bead's x-displacement [23]. The particle's motion is described by an over-damped Langevin equation[4], and at equilibrium its PSD is Lorentzian:

$$S_x(f) = \frac{4\gamma k_\mathrm{B}T/k^2}{1 + f^2/f_c^2} \tag{1.7}$$

with the cut-off frequency f_c (also called "corner frequency") that verifies $f_c = k/(2\pi\gamma)$ where $\gamma = 6\pi R\eta$ is the Stokes friction coefficient, R is the radius of the particle, and η is the dynamic viscosity of the fluid (which is supposed Newtonian here). The integral of the PSD (which is equal to the variance of the signal) verifies:

$$\int_0^\infty S_x(f)\,\mathrm{d}f = \sigma_x^2 = \frac{k_\mathrm{B}T}{k}. \tag{1.8}$$

If the coordinates x are measured in physical units that can be converted to meters (for example µm from the camera), the integral of the PSD allows for computing the stiffness k directly. Then the Stokes term γ can be derived from the value of the cut-off frequency f_c. Thus it is possible to work with fluids of unknown viscosity[5].

If the coordinates X are measured in arbitrary units (for example volts from the position sensing diode), the measured PSD is given by :

$$S_X(f) = \mathscr{C}^2\frac{4\gamma k_\mathrm{B}T/k^2}{1 + f^2/f_c^2} \tag{1.9}$$

with $\mathscr{C}$ the conversion factor from arbitrary units to meters (usually for us $\mathscr{C}$ is in $\mathrm{V}\cdot\mathrm{m}^{-1}$). Then we need to know the Stokes term γ to be able to compute the stiffness k and the conversion factor $\mathscr{C}$ from the PSD measurement. Thus, it is not possible to work with fluids of unknown viscosity without another calibration technique, which usually requires an active driving [24].

Experimentally, we numerically high-pass filter the data to eliminate low-frequency noise (we usually use first order Butterworth filter with cut-off frequency 0.1 Hz or below). Then we compute the Power Spectral Density (PSD) using Welch's overlapped segment averaging estimator ("pwelch" function from Matlab®). When the system is well adjusted, the PSD is very well fitted by a Lorentzian over a wide frequency range, as shown in figure 1.7.

We usually use this method to calibrate the stiffness k. The measurement of the Power Spectral Density is also a good way to check that the system is not perturbed with external noises (mechanical or electronic noises will typically be responsible for some peaks in the PSD). Typical stiffnesses are in the range $0.5\,\mathrm{pN/µm} \leq k \leq 50\,\mathrm{pN/µm}$.

[4]The Langevin equation is described in the following section.

[5]If the viscosity is known, the cut-off frequency gives a second independent measurement of k that can be compared with the one from the PSD's integral.

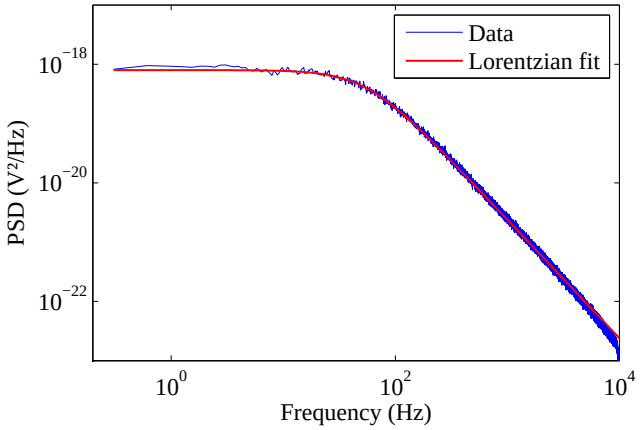

Figure 1.7: Measured Power Spectral Density (PSD) of one bead's x-displacement in water at room temperature ($\sim$ 23 °C), acquired at 20 kHz with the position sensing diode. The Lorentzian fit is in good agreement with data for frequencies $\leq$ 5000 Hz (here $f_c = 56.0$ Hz).

Corrections due to final distance between the bead and the bottom surface

One must be careful with the distance h between the bead and the bottom surface of the cell.

Indeed, the Stokes friction coefficient γ acting on a sphere is modified by the presence of a neighbouring wall, following the Faxén corrections [25]. For the motion parallel to the wall (which is the xy plane for us), the first order correction is given by [26]:

$$\gamma_{\parallel} = \frac{6\pi R\eta}{1 - (9/16)(R/h)}. \tag{1.10}$$

It means that when the particle is close to the bottom surface of the cell, the friction term acting on it is bigger than the bulk one. For example, if $h = 10\,\mu$m and $R = 1\,\mu$m, $\gamma_{\parallel}$ is 6 % bigger than the bulk friction coefficient $\gamma = 6\pi R\eta$. In particular, in the case where we need the value of γ to calibrate k, this correction might become important. More information about rotational and translational Faxén corrections can be found in [27].

The oil-immersion microscope objective is also responsible for spherical aberrations depending on h. It follows that the stiffness k is lowered when the distance between the bottom surface and the bead is increased [28]. This effect means that h must remain constant during experiments (or k must be calibrated for each value of h).

Note that the exact value of k also depends on the bead trapped (because the size and shape can be a little bit different between two beads) and the position of trapping (because of defects of the glass or small impurities in the cell). These corrections are often small ($\leq$ 5 % on the value of k), but can become important if the potential needs to be very well calibrated. Conversely, the conversion factor $\mathscr{C}$ for measurements with the position sensing diode is very dependent of the trapped bead and the position of trapping, and needs to be calibrated before each measurement.

1.2 Stochastic thermodynamics

In this section, we give a brief presentation of stochastic dynamics used to describe Brownian motion, and its links with thermodynamics. A more complete description can be found in Sekimoto's book "Stochastic energetics" [29]. We also summarise some results from (out-of) equilibrium statistical physics theorems, that will be useful for us.

1.2.1 Langevin equation

The one-dimensional motion of a free Brownian particle in a fluid at equilibrium can be described by the Langevin equation [5]:

$$m\ddot{x} = -\gamma\dot{x} + \xi(t) \tag{1.11}$$

with x the position of the particle, $\dot{x} = \frac{\mathrm{d}x}{\mathrm{d}t}$ its velocity, m its mass, $\gamma = 6\pi R\eta$ the Stokes friction coefficient (R is the particle's radius and η is the viscosity of the fluid), and $\xi(t)$ the thermal random force due to the collisions with microscopic molecules of fluid. The motion of the Brownian particle is described on a time much larger than the characteristic time of the fluid molecules movements. The thermal random force is modelled by a Gaussian white noise which verifies:

$$\begin{aligned} \langle \xi(t) \rangle &= 0 \\ \langle \xi(t)\xi(t') \rangle &= 2\gamma k_{\mathrm{B}} T \delta(t - t') \end{aligned} \tag{1.12}$$

where k_{B} is the Boltzmann constant, T is the temperature of the fluid, $\langle . \rangle$ stands for the ensemble average, and δ is the Dirac delta function.

The Langevin equation can also be used to describe the Brownian motion of particles submitted to external forces in addition to the thermal random force. In this case, we assume that even if the Brownian particle behaves in a non-equilibrium manner under an external forcing, the environment remains in equilibrium. For example, a Brownian particle trapped by optical tweezers will be described by the equation:

$$m\ddot{x} = -\gamma\dot{x} - kx + \xi(t) \tag{1.13}$$

where k is the trap stiffness.

Finally, in the case where the characteristic time $\tau_{\mathrm{inertia}} = m/\gamma$ is small compared to the time resolution, we can neglect the inertia term and use an over-damped Langevin equation:

$$\gamma\dot{x} = -kx + \xi(t) \tag{1.14}$$

Experimentally, with silica beads of radius $R = 1\,\mu\mathrm{m}$ in water at room temperature, we have $m \approx 1 \times 10^{-14}\,$kilogram and $\gamma \approx 2 \times 10^{-8}\,\mathrm{kg \cdot s^{-1}}$. It follows that the characteristic inertia time is $\tau_{\mathrm{inertia}} \approx 5 \times 10^{-7}\,\mathrm{s}$ which is very short compared to our acquisition times.
Moreover, for our usual stiffnesses ($0.5 \leq k \leq 50\,\mathrm{pN/\mu m}$) the resonance period of the harmonic oscillator $10^{-3} \geq 2\pi\sqrt{m/k} \geq 10^{-4}\,\mathrm{s}$ is always smaller than the characteristic trapping time $\tau_{\mathrm{trap}} = 2\pi\gamma/k$, which is in the range $10^{-1} \geq \tau_{\mathrm{trap}} \geq 10^{-3}\,\mathrm{s}$.

Throughout the Thesis, we always describe our trapped Brownian particles motions with over-damped Langevin equations, and add external forces when necessary.

1.2.2 Stochastic work and heat

We consider a Brownian particle in a potential $U(x)$, described by the over-damped Langevin equation:

$$\gamma\dot{x} = -\frac{\mathrm{d}U}{\mathrm{d}x} + \xi(t) \tag{1.15}$$

Following Sekimoto [30], this equation can be seen as the first law of thermodynamics for stochastic dynamics. For a small change of position $\mathrm{d}x$ we can write:

$$0 = -\left(-\gamma\dot{x} + \xi(t)\right)\mathrm{d}x + \frac{\mathrm{d}U}{\mathrm{d}x}\mathrm{d}x \tag{1.16}$$

The term $(-\gamma\dot{x} + \xi(t))$ is the force exerted by the heat bath on the system, and the term $\frac{\mathrm{d}U}{\mathrm{d}x}\mathrm{d}x$ is a change of internal energy of the system $\mathrm{d}U$. Then the equation can be rewritten:

$$0 = \delta Q + \mathrm{d}U \tag{1.17}$$

where:

$$\delta Q \equiv -\left(-\gamma\dot{x} + \xi(t)\right)\mathrm{d}x \tag{1.18}$$

is identified as the stochastic heat dissipated by the system into the heat bath.[6]

If we now suppose that the potential also depends on an external parameter λ (controlled by an external agent). The equation will be slightly modified:

$$0 = -\left(-\gamma\dot{x} + \xi(t)\right)\mathrm{d}x + \frac{\partial U}{\partial x}(x,\lambda)\mathrm{d}x \tag{1.19}$$

and, since $\mathrm{d}U = (\partial U/\partial x)\mathrm{d}x + (\partial U/\partial\lambda)\mathrm{d}\lambda$, we get:

$$\frac{\partial U}{\partial\lambda}\mathrm{d}\lambda = \delta Q + \mathrm{d}U. \tag{1.20}$$

The left-hand side term is then identified with the work done by the external agent to the system through the change of the variable λ:

$$\delta W \equiv \frac{\partial U}{\partial\lambda}\mathrm{d}\lambda. \tag{1.21}$$

Finally, in the formalism of the stochastic energetics, if we consider a system described by an over-damped Langevin equation:

$$\gamma\dot{x} = -\frac{\partial U}{\partial x}(x,\lambda) + \xi(t) \tag{1.22}$$

The stochastic heat dissipated by the system into the heat bath along the trajectory $x(t)$ between time $t = 0$ and t is:

$$Q_{0,t} = \int_0^t -\left(\xi - \gamma\dot{x}\right)\dot{x}\,\mathrm{d}t'. \tag{1.23}$$

The stochastic work received by the system along the trajectory $x(t)$ between time $t = 0$ and t is:

$$W_{0,t} = \int_0^t \frac{\partial U}{\partial\lambda}\dot{\lambda}\,\mathrm{d}t'. \tag{1.24}$$

Note that is it also possible to define a stochastic (trajectory dependent) entropy, but this will not be discussed in this Thesis (see [31] for more information).

[6] From the equation of motion, δQ is the work done by the reaction force from the system to the heat bath. It is identified as a heat term because in classical thermodynamics a heat bath can only exchange heat with a system.

1.2.3 Fluctuation-Dissipation Theorem

The Fluctuation-Dissipation Theorem (FDT) was developed in the framework of the linear response theory. It links the linear response of a given system to a small external perturbation with the fluctuation properties of the system in thermal equilibrium. A more complete description can be found in Kubo's review [32].

The first example was the Einstein's relation [3], which links the diffusion coefficient of a free Brownian particle D to its Stokes friction term $\gamma = 6\pi R\eta$:

$$D = \frac{k_\mathrm{B}T}{\gamma}. \tag{1.25}$$

The diffusion coefficient is characteristic of the fluctuations of the system at equilibrium, and the friction term is the inverse of the particle's mobility which gives the change of velocity in response to an applied force (*i.e.* a perturbation). Note that the value of the auto-correlation of the thermal random force in the Langevin equation (second line of equation 1.12) is chosen to verify the Einstein's relation.

In the general case, one considers a physical quantity $B(t)$ of a dynamical system, described by an Hamiltonian H_0, and one looks for the response of B to an external perturbation $f(t)$. Then, the average perturbed quantity $\langle B(t)\rangle_\mathrm{pert}$ can be written at the first order in the perturbation expansion as:

$$\langle B(t)\rangle_\mathrm{pert} = \langle B(t)\rangle_\mathrm{unpert} + \int_{-\infty}^{t} R(t-s)f(s)\,\mathrm{d}s \tag{1.26}$$

where $\langle . \rangle_\mathrm{unpert}$ is the average in the equilibrium system (when no perturbation is applied), and $R(t-s)$ is called the linear response function. Note that if the perturbation is a pulse (*i.e.* $f(t)$ is a Dirac δ function), $\langle B(t)\rangle_\mathrm{pert} - \langle B(t)\rangle_\mathrm{unpert}$ is directly equal to $R(t)$.
Formally the perturbation can be written in the form of a change in the system's Hamiltonian:

$$\Delta H = -f(t)A \tag{1.27}$$

where A is another physical quantity of the system (which might be equal to B).
Then, the Fluctuation-Dissipation Theorem (FDT) links the response function R to the correlation function between A and B:

$$R(t) = -\frac{1}{k_\mathrm{B}T}\frac{\mathrm{d}C_{BA}(t)}{\mathrm{d}t} \tag{1.28}$$

where the correlation function C_{BA} is defined by:

$$C_{BA} = \langle B(t)A(0)\rangle_\mathrm{unpert}. \tag{1.29}$$

In this thesis, the FDT will be used in situations where $B = A = x$, with x the position of the particle, and we will thus look for the response of x to an applied force $f(t)$. In this case, the FDT states:

$$R(t) = -\frac{1}{k_\mathrm{B}T}\frac{\mathrm{d}C_{xx}(t)}{\mathrm{d}t} \tag{1.30}$$

Since it is often easier to measure the response to a step perturbation (*i.e.* $f(t)$ is an Heaviside function) than to an impulse perturbation, we can define an integrated response function:

$$\chi(t) = \int_0^t R(s)\,\mathrm{d}s \tag{1.31}$$

which is directly given by the measured $\langle x(t)\rangle_{\text{pert}} - \langle x(t)\rangle_{\text{unpert}}$ when $f(t)$ is an Heaviside step function.
And finally, the FDT gives:

$$\chi(t) = \frac{1}{k_{\text{B}}T}\left(C_{xx}(0) - C_{xx}(t)\right) \tag{1.32}$$

which is the expression that will be tested in chapters 3 and 5.

1.2.4 Fluctuation Theorems

Fluctuation Theorems (FT) are important non-equilibrium theorems that predict some properties of the Probability Distribution Functions (PDF) of stochastic quantities like work, heat or entropy change, evaluated along fluctuating trajectories. There exist several formulations of them and we only give two examples here. A more general description of Fluctuations Theorems can be found in Seifert's review [31].

The Jarzynski Equality for the work

The Jarzynski Equality is an integral Fluctuation Theorem which was first introduced by Jarzynski in the framework of Hamiltonian dynamics [33]. It was later shown to hold also for stochastic dynamics [34–36]. It links the stochastic work received when a system is driven from an equilibrium state to another state with the equilibrium free energy difference between the two states.

If we consider a system driven by a control parameter from an equilibrium state A to a state B (which is not necessarily at equilibrium), the stochastic work received by the system W_{st} during the procedure (which is a fluctuating quantity) verifies:

$$\left\langle \exp\left(-\frac{W_{\text{st}}}{k_{\text{B}}T}\right)\right\rangle = \exp\left(-\frac{\Delta F}{k_{\text{B}}T}\right) \tag{1.33}$$

where $\langle . \rangle$ denotes the ensemble average over all possible trajectories, and the free energy difference $\Delta F = F_B - F_A$ is the difference between the free energy of the system in the equilibrium state A and the free energy that the system would have if it was at equilibrium in the state B.

This equality is interesting because it allows for measuring an equilibrium quantity ΔF by applying a non-equilibrium driving procedure to the system. It will be used (as well as a detailed version) in chapter 2.

A detailed Stationary State Fluctuation Theorem for the heat

A detailed version of the Stationary State Fluctuation Theorem for the heat can be found in [37]. It states that the probability to observe a given amount of heat Q_τ being dissipated during the time τ in a non-equilibrium steady state satisfies:

$$\frac{P(Q_\tau)}{P(-Q_\tau)} = \exp\left(\frac{Q_\tau}{k_{\text{B}}T}\right) \tag{1.34}$$

in the limit where τ is large.

A modified version of this detailed Fluctuation Theorem will be used in chapter 4.

Chapter 2

Landauer's Principle

Et puis les Shadoks les plus doués pour les mathématiques enfourchent leur ordinateur à pédales [...] car [ils] avaient entendu dire que plus un ordinateur va vite, plus il donne de bons résultats...

Jacques Rouxel

2.1 A link between information theory and thermodynamics

The Landauer's principle was first introduced by Rolf Landauer in 1961 [38]. It states that any logically irreversible transformation of classical information is necessarily accompanied by the dissipation of at least $k_{\mathrm{B}}T\ln 2$ of heat per lost bit, where k_{B} is the Boltzmann constant and T is the temperature. This quantity represents only $\sim 3\times 10^{-21}\,\mathrm{J}$ at room temperature (300 K) but is a general lower bound, independent of the specific kind of memory system used.

An operation is said to be logically irreversible if its input cannot be uniquely determined from its output. Any Boolean function that maps several input states onto the same output state, such as AND, NAND, OR and XOR, is therefore logically irreversible. In particular, the erasure of information, the RESET TO ZERO operation, is logically irreversible and leads to an entropy increase of at least $k_{\mathrm{B}}\ln 2$ per erased bit.

A simple example can be done with a 1-bit memory system (*i.e.* a systems with two states, called 0 and 1) modelled by a physical double well potential in contact with a single heat bath. In the initial state, the bistable potential is considered to be at equilibrium with the heat bath, and each state (0 and 1) have same probability to occur. Thus, the entropy of the system is $S = k_{\mathrm{B}}\ln 2$, because there are two states with probability 1/2. If a RESET TO ZERO operation is applied, the system is forced into state 0. Hence, there is only one accessible state with probability 1, and the entropy vanishes $S = 0$. Since the Second Law of Thermodynamics states that the entropy of a closed system cannot decrease on average, the entropy of the heat bath must increase of at least $k_{\mathrm{B}}\ln 2$ to compensate the memory system's loss of entropy. This

increase of entropy can only be done by an heating effect: the system must release in the heat bath at least $k_B T \ln 2$ of heat per bit erased[1].

For a reset operation with efficiency smaller than 1 (*i.e.* if the operation only erase the information with a probability $p < 1$), the Landauer's bound is generalised:

$$\langle Q \rangle \geq k_B T \left[\ln 2 + p \ln(p) + (1-p) \ln(1-p) \right] \tag{2.1}$$

The Landauer's principle was widely discussed as it could solve the paradox of Maxwell's "demon" [39–41]. The demon is an intelligent creature able to monitor individual molecules of a gas contained in two neighbouring chambers initially at the same temperature. Some of the molecules will be going faster than average and some will be going slower. By opening and closing a molecular-sized trap door in the partitioning wall, the demon collects the faster (hot) molecules in one of the chambers and the slower (cold) ones in the other. The temperature difference thus created can be used to run a heat engine, and produce useful work. By converting information (about the position and velocity of each particle) into energy, the demon is therefore able to decrease the entropy of the system without performing any work himself, in apparent violation of the Second Law of Thermodynamics. A simpler version with a single particle, called Szilard Engine [42] has recently been realised experimentally [22], showing that information can indeed be used to extract work from a single heat bath. The paradox can be resolved by noting that during a full thermodynamic cycle, the memory of the demon, which is used to record the coordinates of each molecule, has to be reset to its initial state. Thus, the energy cost to manipulate the demon's memory compensate the energy gain done by sorting the gas molecules, and the Second Law of Thermodynamics is not violated any more.

More information can be found in the two books [43, 44], and in the very recent review [45] about thermodynamics of information based on stochastic thermodynamics and fluctuation theorems.

In this chapter, we describe an experimental realisation of the Landauer's information erasure procedure, using a Brownian particle trapped with optical tweezers in a time-dependent double well potential. This kind of system was theoretically [46] and numerically [47] proved to show the Landauer's bound $k_B T \ln 2$ for the mean dissipated heat when an information erasure operation is applied. The results described in this chapter were partially presented in two articles [48, 49], and were later confirmed by two independent experimental works [50, 51].

[1] It it sometimes stated that the cost is $k_B T \ln 2$ per bit written. It is actually the same operation as the RESET TO ZERO can also be seen to store one given state (here state 0), starting with an unknown state.

2.2 Experimental set-up

2.2.1 The one-bit memory system

The one-bit memory system is made of a double well potential where one particle is trapped by optical tweezers. If the particle is in the left-well the system is in the state "0", if the particle is in the right-well the system in the state "1" (see figure 2.1).

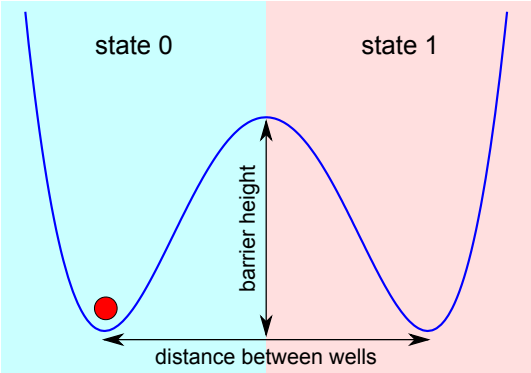

Figure 2.1: Schematic representation of the one-bit memory system, made of one particle trapped in a double well potential.

The particles are silica beads (radius $R = 1.00 \pm 0.05\,\mu m$), diluted at a low concentration in bidistilled water. The solution is contained in a disk-shape cell, already described in section 1.1.2. The center of the cell has a smaller depth ($\sim 80\,\mu m$) compared to the rest of the cell ($\sim 1\,mm$), see figure 2.2. This central area contains less particles than the rest of the cell and provides us a clean region where one particle can be trapped for a long time without interacting with other particles.

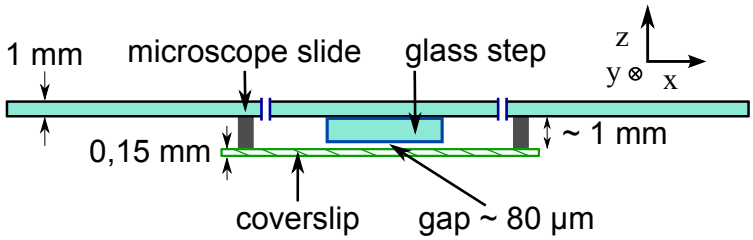

Figure 2.2: Schematic representation of the cell used to trap particles dispersed in water (view from the side). The central part has a smaller gap than the rest of the cell.

The double well potential is created using an Acousto-Optic Deflector which allows us to switch very rapidly (at a rate of 10 kHz) a laser beam (wavelength $\lambda = 1064\,nm$) between two positions (separated by a fixed distance $d \sim 1\,\mu m$), as explained in section 1.1.3. These two positions become for the particle the two wells of the double well potential. The intensity of the laser I can be controlled from 10 mW to more than 100 mW, which enables us to change

the height of the double well potential's central barrier[2]. A NanoMax closed-loop piezoelectric stage from Thorlabs® with high resolution (5 nm) can move the cell with regard to the position of the laser. Thus it allows us to create a fluid flow around the trapped particle. The position of the bead is tracked using a fast camera with a resolution of 108 nm per pixel, which after treatment gives the position with a precision greater than 5 nm. The trajectories of the bead are sampled at 502 Hz. See figure 2.3.

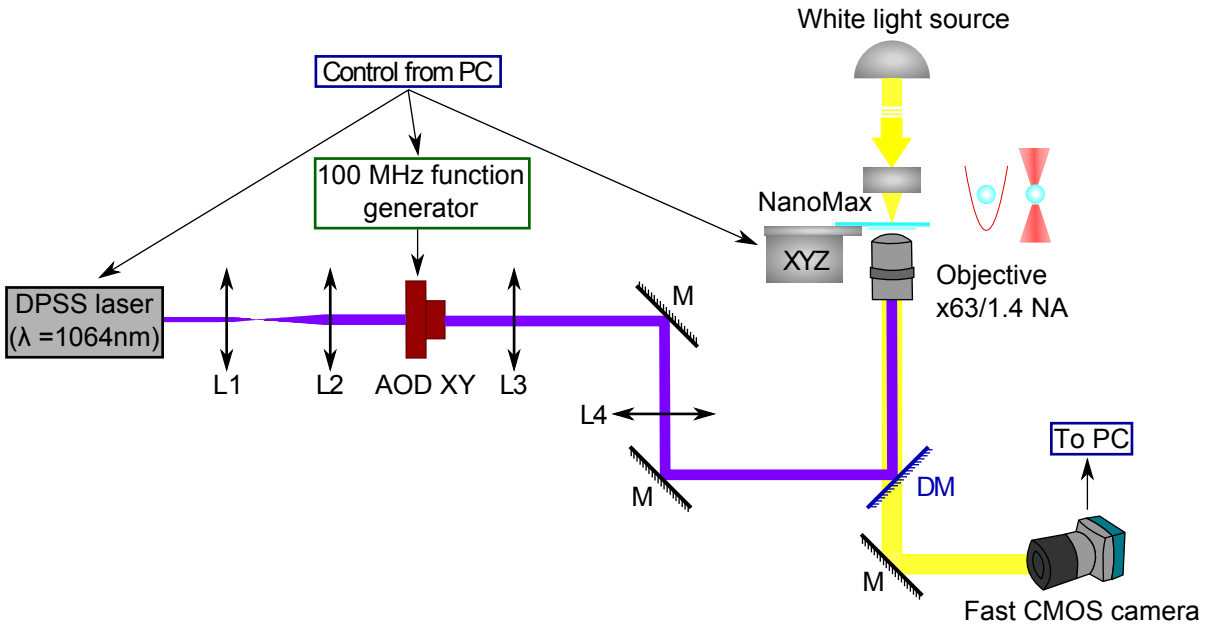

Figure 2.3: Schematic representation of optical tweezers set-up used to trap one particle in a double well potential. The Acousto-Optic Deflector (AOD) is used to switch rapidly the trap between two positions. The NanoMax piezo stage can move the cell with regard to the laser, which creates a flow around the trapped particle. "M" are mirrors and "DM" is a dichroic mirror.

The beads are trapped at a distance $h = 25\,\mu m$ from the bottom of the cell. The double well potential must be tuned for each particle, in order to be as symmetrical as possible and to have the desired central barrier. The tuning is done by adjusting the distance between the two traps and the time that the laser spend on each trap. The asymmetry can be reduced to $\sim 0.1\,k_BT$. The double well potential $U_0(x, I)$ (with x the position and I the intensity of the laser) can simply be measured by computing the equilibrium distribution of the position for one particle in the potential:

$$P(x, I) \propto \exp\left(-\frac{U(x, I)}{k_B T}\right). \tag{2.2}$$

One typical double well potential is shown in figure 2.4.

[2]The values are the power measured on the beam before the microscope objective, so the "real" power at the focal point should be smaller, due to the loss in the objective.

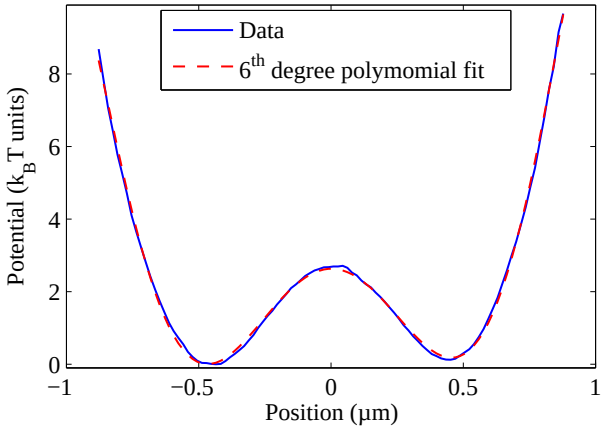

Figure 2.4: Double well potential measured by computing the equilibrium distribution of one particle's positions, with $I_{\text{laser}} = 15\,\text{mW}$. Here the distribution is computed on 1.5×10^6 points sampled at 502 Hz (*i.e.* a 50 min long measurement). The double well potential is well fitted by a 6^{th} degeree polynom.

2.2.2 The information erasure procedure

We perform the erasure procedure as a logically irreversible operation. This procedure brings the system initially in one unknown state (0 or 1 with same probability) to one chosen state (we choose 0 here). It is done experimentally in the following way (and summarised in figure 2.5a):

- At the beginning the bead must be trapped in one well-defined state (0 or 1). For this reason, we start with a high laser intensity ($I_{\text{high}} = 48\,\text{mW}$) so that the central barrier is more than $8\,k_BT$. In this situation, the characteristic jumping time (Kramers Time [52]) is about 3000 s, which is long compared to the time of the experiment, and the equivalent stiffness of each well is about 1.5 pN/µm. The system is left 4 s with high laser intensity so that the bead is at equilibrium in the well where it is trapped[3]. The potential $U_0(x, I_{\text{high}})$ is represented in figure 2.5b **1**.

- The laser intensity is first lowered (in a time $T_{\text{low}} = 1\,\text{s}$) to a low value ($I_{\text{low}} = 15\,\text{mW}$) so that the barrier is about $2.2\,k_BT$. In this situation the jumping time falls to $\sim 10\,\text{s}$, and the equivalent stiffness of each well is about 0.3 pN/µm. The potential $U_0(x, I_{\text{low}})$ is represented figure 2.5b **2**.

- A viscous drag force linear in time is induced by displacing the cell with respect to the laser using the piezoelectric stage. The force is given by $f = \gamma v$ where $\gamma = 6\pi R\eta$ (η is the viscosity of water) and v the speed of displacement. The bead is pushed by f and ends always in the same well (state 0 here) independently of the initial state. Since the force does not depend on the particle's position, we can introduce an additional potential term $-fx$ that tilts the double well. The tilted potential $V(x,t) = U_0(x, I_{\text{low}}) - f(t)x$ is represented in figures 2.5b **3** to **5**.

[3]The characteristic time for the particle trapped in one well when the barrier is high is 0.08 s.

- At the end, the force is stopped and the central barrier is raised again to its maximal value (in a time $T_{\text{high}} = 1\,\text{s}$). See figure 2.5b **6**.

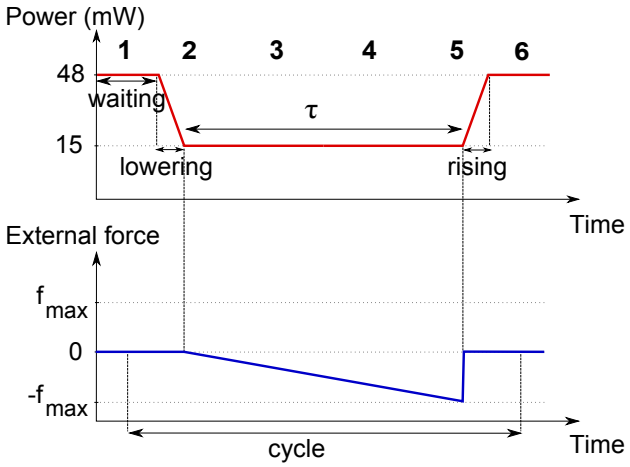

(a) Laser intensity and external drag force.

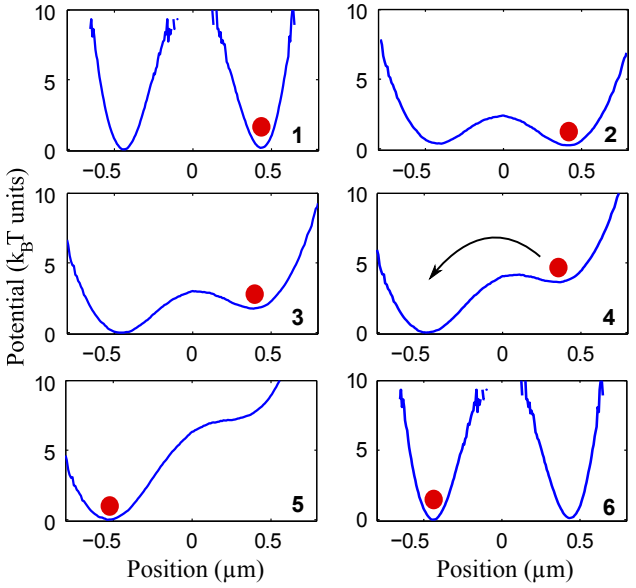

(b) Potential felt by the particle.

Figure 2.5: Schematical representation of the erasure procedure. The potential felt by the trapped particle is represented at different stages of the procedure (**1** to **6**). For **1** and **2** the potential $U_0(x, I)$ is measured. For **3** to **5** the potential is constructed from $U_0(x, I_{\text{low}})$ knowing the value of the applied drag force.

The total duration of the erasure procedure is $T_{\text{low}} + \tau + T_{\text{high}}$. Since we kept $T_{\text{low}} = T_{\text{high}} = 1\,\text{s}$, a procedure is fully characterised by the duration τ and the maximum value of the force applied f_{max}. Its efficiency is characterized by the "proportion of success" P_S, which is the proportion of trajectories where the bead ends in the chosen well (state 0), independently of where it started.

Note that for the theoretical procedure, the system must be prepared in an equilibrium state with same probability to be in state 1 than in state 0. However, it is more convenient experimentally to have a procedure always starting in the same position. Therefore we separate the procedure in two sub-procedures: one where the bead starts in state 1 and is erased in state 0, and one where the bead starts in state 0 and is erased in state 0. The fact that the position of the bead at the beginning of each procedure is actually known is not a problem because this knowledge is not used by the erasure procedure. The important points are that there are as many procedures starting in state 0 than in state 1, and that the procedure is always the same regardless of the initial position of the bead. Examples of trajectories for the two sub-procedures $1 \to 0$ and $0 \to 0$ are shown in figure 2.6.

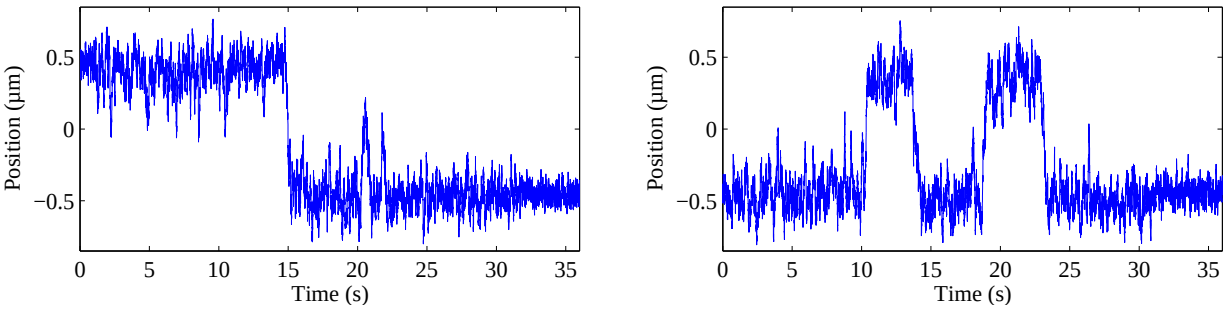

(a) $1 \to 0$ (b) $0 \to 0$

Figure 2.6: Examples of trajectories for the erasure procedure. $t = 0$ corresponds to the time where the barrier starts to be lowered. The two possibilities of initial state are shown.

2.3 Landauer's bound for dissipated heat

2.3.1 Computing the dissipated heat

The system can be described by an over-damped Langevin equation:

$$\gamma \dot{x} = -\frac{\partial U_0}{\partial x}(x, I) + f(t) + \xi(t) \tag{2.3}$$

with x the position of the particle[4], $\dot{x} = \frac{\mathrm{d}x}{\mathrm{d}t}$ its velocity, $\gamma = 6\pi R\eta$ the friction coefficient (η is the viscosity of water), $U_0(x, I)$ the double well potential created by the optical tweezers, $f(t)$ the external drag force exerted by displacing the cell, and $\xi(t)$ the thermal noise which verifies $\langle \xi(t) \rangle = 0$ and $\langle \xi(t)\xi(t') \rangle = 2\gamma k_\mathrm{B} T \delta(t - t')$, where $\langle . \rangle$ stands for the ensemble average.

Following the formalism of the stochastic energetics [30], the heat dissipated by the system into the heat bath along the trajectory $x(t)$ between time $t = 0$ and t is:

$$Q_{0,t} = \int_0^t -\left(\xi(t') - \gamma \dot{x}(t')\right) \dot{x}(t') \, \mathrm{d}t'. \tag{2.4}$$

Using equation 2.3, we get:

$$Q_{0,t} = \int_0^t \left(-\frac{\partial U_0}{\partial x}(x, I) + f(t')\right) \dot{x}(t') \, \mathrm{d}t'. \tag{2.5}$$

For the erasure procedure described in 2.2.2 the dissipated heat can be decomposed in three terms:

$$Q_\mathrm{erasure} = Q_\mathrm{barrier} + Q_\mathrm{optical} + Q_\mathrm{drag} \tag{2.6}$$

Where:

- Q_barrier is the heat dissipated when the central barrier is lowered and risen ($f = 0$ during these stages of the procedure):

$$Q_\mathrm{barrier} = \int_0^{T_\mathrm{low}} \left(-\frac{\partial U_0}{\partial x}(x, I)\right) \dot{x} \, \mathrm{d}t' + \int_{T_\mathrm{low}+\tau}^{T_\mathrm{low}+\tau+T_\mathrm{high}} \left(-\frac{\partial U_0}{\partial x}(x, I)\right) \dot{x} \, \mathrm{d}t' \tag{2.7}$$

- Q_optical is the heat dissipated due to the force of the potential U_0 created by the optical traps, during the time τ where the external drag force is applied (the laser intensity is constant during this stage of the procedure):

$$Q_\mathrm{optical} = \int_{T_\mathrm{low}}^{T_\mathrm{low}+\tau} \left(-\frac{\partial U_0}{\partial x}(x, I)\right) \dot{x} \, \mathrm{d}t' \tag{2.8}$$

- Q_drag is the heat dissipated due to the external drag force applied during the time τ (the laser intensity is constant during this stage of the procedure):

$$Q_\mathrm{drag} = \int_{T_\mathrm{low}}^{T_\mathrm{low}+\tau} f \dot{x} \, \mathrm{d}t' \tag{2.9}$$

[4] We take the reference $x = 0$ as the middle position between the two traps.

The duration of the barrier's height change is much longer than the relaxation time of the particle in the trap ($\sim 0.1\,\mathrm{s}$). So, the lowering and rising of the barrier can be considered as a quasi-static cyclic process, and do not contribute to the dissipated heat in average. The complete calculation can also be done if we assume that the particle do not jump out of the well where it is during the change of barrier height. In this case, we can do a quadratic approximation: $U_0(x, I) = \frac{1}{2}k(I)x^2$ where k is the stiffness of the trap, which evolves in time because it depends linearly on the intensity of the laser. Then:

$$\langle Q_{\text{lowering}} \rangle = \left\langle \int_0^{T_{\text{low}}} -kx\dot{x}\,\mathrm{d}t' \right\rangle = \int_0^{T_{\text{low}}} -\frac{k}{2}\,\mathrm{d}\left(\langle x^2 \rangle\right). \tag{2.10}$$

Using the equipartition theorem (which is possible because the change of stiffness is assumed to be quasi-static), we get:

$$\langle Q_{\text{lowering}} \rangle = \int_0^{T_{\text{low}}} -k\frac{k_{\text{B}}T}{2}\,\mathrm{d}\left(\frac{1}{k}\right) = \frac{k_B T}{2}\ln\left(\frac{k_{\text{low}}}{k_{\text{high}}}\right). \tag{2.11}$$

The same calculation gives $\langle Q_{\text{rising}} \rangle = \frac{k_B T}{2}\ln\left(\frac{k_{\text{high}}}{k_{\text{low}}}\right)$, and it follows directly that $\langle Q_{\text{barrier}} \rangle = \langle Q_{\text{lowering}} \rangle + \langle Q_{\text{rising}} \rangle = 0$.

The heat dissipated due to the potential when the force is applied is also zero in average. Indeed, the intensity is constant and U_0 becomes a function depending only on x. It follows that:

$$\langle Q_{\text{optical}} \rangle = \int_{T_{\text{low}}}^{T_{\text{low}}+\tau} -\frac{\mathrm{d}U_0}{\mathrm{d}x}\,\mathrm{d}x = \Big[U_0(x)\Big]_{x(T_{\text{low}}+\tau)}^{x(T_{\text{low}})}. \tag{2.12}$$

Since the potential is symmetrical, there is no change in U_0 when the bead goes from one state to another, and $\langle U_0(x(T_{\text{low}})) - U_0(x(T_{\text{low}} + \tau)) \rangle = 0$.

Finally, since we are interested in the mean dissipated heat, the only relevant term to calculate is the heat dissipated by the external drag force:

$$Q_{\text{drag}} = \int_{T_{\text{low}}}^{T_{\text{low}}+\tau} \gamma v(t')\dot{x}\,\mathrm{d}t'. \tag{2.13}$$

Where γ is the known friction coefficient, $v(t)$ is the imposed displacement of the cell (which is not a fluctuating quantity) and $\dot{x}$ can be estimated simply:

$$\dot{x}(t + \delta t/2) = \frac{x(t + \delta t) - x(t)}{\delta t}. \tag{2.14}$$

We measured Q_{drag} for several erasure procedures with different parameters τ and $f_{\max}$. For each set of parameters, we repeated the procedure a few hundred times in order to compute the average dissipated heat.

We didn't measure Q_{lowering} and Q_{rising} because it requires to know the exact shape of the potential at any time during lowering and rising of the central barrier. The potentials could have been measured by computing the equilibrium distribution of one particle's positions for different values of I. But these measurements would have been very long since they require to be done on times much longer than the Kramers time to give a good estimation of the double well potential. Nevertheless, we estimated on numerical simulations with parameters close to our experimental ones that $\langle Q_{\text{lowering}} + Q_{\text{optical}} + Q_{\text{rising}} \rangle \approx 0.07\,\mathrm{k_B T}$ which is only 10 % of the Landauer's bound.

2.3.2 Results

We first measured P_S the proportion of success for different set of τ and $f_{\max}$. Qualitatively, the bead is more likely to jump from one state to another thanks to thermal fluctuations if the waiting time is longer. Of course it also has fewer chances to escape from state 0 if the force pushing it toward this state is stronger. We did some measurements keeping the product $\tau \times f_{\max}$ constant. The results are shown in figure 2.7 (blue points).

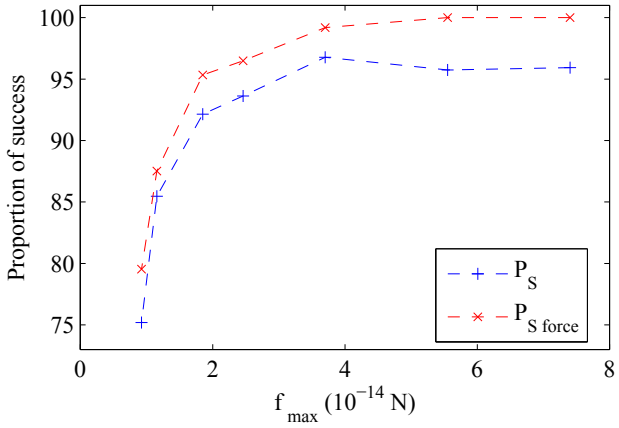

Figure 2.7: Proportion of success for different values of τ and $f_{\max}$, keeping constant the product $\tau \times f_{\max} \approx 0.4\,\mathrm{pN \cdot s}$ (which corresponds to $\tau \times v_{max} = 20\,\mu\mathrm{m}$). P_S quantifies the ratio of procedures which ends in state 0 after the barrier is risen. $P_{S\,\mathrm{force}}$ quantifies the ratio of procedures which ends in state 0 before the barrier is risen.

The proportion of success is clearly not constant when the product $\tau \times f_{\max}$ is kept constant, but, as expected, the higher the force, the higher P_S. One must also note that the experimental procedure never reaches a P_S higher than $\sim 95\,\%$. This effect is due to the last part of the procedure: since the force is stopped when the barrier is low, the bead can always escape from state 0 during the time needed to rise the barrier. This problem can be overcome with a higher barrier or a faster rising time T_{high}. It was tested numerically by Raoul Dillenscheider and Éric Lutz, using a protocol adapted from [47] to be close to our experimental procedure. They showed that for a high barrier of $8\,k_BT$ the proportion of success approaches only $\sim 94\,\%$, whereas for a barrier of $15\,k_BT$ it reaches $\sim 99\,\%$. Experimentally we define a proportion of success $P_{S\,\mathrm{force}}$ by counting the number of procedures where the particle ends in state 0 when the force is stopped (*before* the rising of the barrier). It quantifies the efficiency of the pushing force, which is the relevant one since we have shown that the pushing force is the only contribution to the mean dissipated heat. Measured $P_{S\,\mathrm{force}}$ are shown in figure 2.7 (red points). $P_{S\,\mathrm{force}}$ is roughly always $5\,\%$ bigger than P_S and it reaches $100\,\%$ of success for high forces.

To reach the Landauer's bound, the force necessary to erase information must be as low as possible, because it is clear that a higher force will always produce more heat for the same proportion of success. Moreover, the bound is only reachable for a quasi-static (*i.e.* $\tau \to \infty$) erasure procedure, and the irreversible heat dissipation associated with a finite time procedure should decrease as $1/\tau$ [53]. Thus we decided to work with a chosen τ and to manually[5] optimise the applied force. The idea was to choose the lowest value of $f_{\max}$ which gives a $P_{S\,\mathrm{force}} \geq 95\,\%$.

[5]The term "manually" refers to the fact that the optimisation was only empirical and that we did not

The Landauer's bound $k_B T \ln 2$ is only valid for totally efficient procedures. Thus one should theoretically look for a Landauer's bound corresponding to each experimental proportion of success (see equation 2.1). Unfortunately the function $\ln 2 + p \ln(p) + (1-p)\ln(1-p)$ quickly decreases when p is lower than 1. To avoid this problem, we made an approximation by computing $\langle Q \rangle_{\to 0}$ the mean dissipated heat for the trajectories where the memory is erased (*i.e* the ones ending in state 0). We consider that $\langle Q \rangle_{\to 0}$ mimics the mean dissipated heat for a procedure with 100 % of success. This approximation is reasonable as long as $P_{S\,\text{force}}$ is close enough to 100 %, because the negative contributions which reduce the average dissipated heat are mostly due to the rare trajectories going against the force (*i.e* ending in state 1). Of course, at the limit where the force is equal to zero, one should find $P_{S\,\text{force}} = 50\,\%$ and $\langle Q \rangle_{\to 0} = 0$ which is different from $k_B T \ln 2$. The mean dissipated heat for several procedures are shown in figure 2.8.

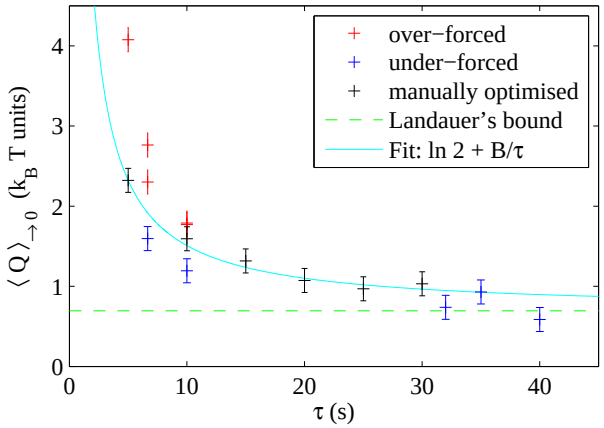

Figure 2.8: Mean dissipated heat for several procedures, with fixed τ and different values of $f_{\max}$. The red points have a force too high, and a $P_{S\,\text{force}} \geq 99\,\%$. The blue points have a force too low and $91\,\% \leq P_{S\,\text{force}} < 95\,\%$ (except the last point which has $P_{S\,\text{force}} \approx 80\,\%$). The black points are considered to be optimised and have $95\,\% \leq P_{S\,\text{force}} < 99\,\%$. The error bars are $\pm 0.15\,\text{k}_\text{B}\text{T}$ estimated from the reproductibility of measurement with same parameters. The fit $\langle Q \rangle_{\to 0} = \ln 2 + B/\tau$ is done only by considering the optimised procedures.

The mean dissipated heat decreases with the duration of the erasure procedure τ and approaches the Landauer's bound $k_B T \ln 2$ for long times. Of course, if we compute the average on all trajectories (and not only on the ones ending in state 0) the values of the mean dissipated heat are smaller, but remain greater than the generalised Landauer's bound for the corresponding proportion of success p:

$$\langle Q \rangle_{\to 0} \geq \langle Q \rangle \geq k_B T \left[\ln 2 + p \ln(p) + (1-p)\ln(1-p)\right] \tag{2.15}$$

For example, the last point ($\tau = 40\,\text{s}$) has a proportion of success $P_{S\,\text{force}} \approx 80\,\%$, which corresponds to a Landauer's bound of only $\approx 0.19\,\text{k}_\text{B}\text{T}$, and we measure $\langle Q \rangle_{\to 0} = 0.59\,\text{k}_\text{B}\text{T}$ greater than $\langle Q \rangle = 0.26\,\text{k}_\text{B}\text{T}$. The manually optimised procedures also seem to verify a decreasing of $\langle Q \rangle_{\to 0}$ proportional to $1/\tau$. A numerical least square fit $\langle Q \rangle_{\to 0} = \ln 2 + B/\tau$ is plotted

computed the theoretical best $f_{\max}$ for a given value of τ.

in figure 2.8 and gives a value of $B = 8.15\,\mathrm{k_B T}\cdot\mathrm{s}$. If we do a fit with two free parameters $\langle Q\rangle_{\to 0} = A + B/\tau$, we find $A = 0.72\,\mathrm{k_B T}$ which is close to $k_B T \ln 2 \approx 0.693\,\mathrm{k_B T}$.

One can also look at the distribution of $Q_{\mathrm{drag}\to 0}$. Histograms for procedures going from 1 to 0 and from 0 to 0 are shown in figure 2.9. The statistics are not sufficient to conclude on the exact shape of the distribution, but as expected, there is more heat dissipated when the particle has to jump from state 1 to state 0 than when it stays in state 0. It is also noticeable that a fraction of the trajectories always dissipate less heat than the Landauer's bound, and that some of them even have a negative dissipated heat. We are able to approach the Landauer's bound in average thanks to those trajectories where the thermal fluctuations help us to erase the information without dissipating heat.

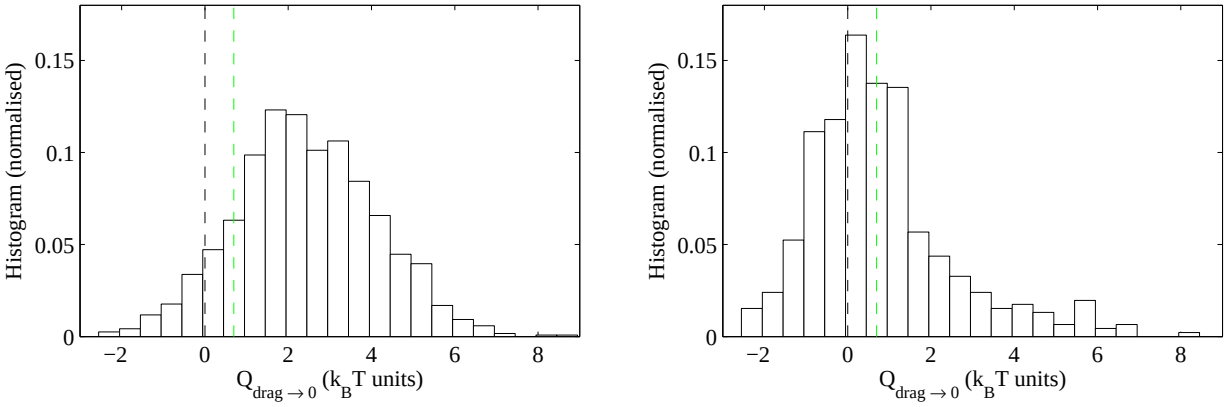

(a) $1 \to 0$ (b) $0 \to 0$

Figure 2.9: Histograms of the dissipated heat $Q_{\mathrm{drag}\to 0}$. (a) For one procedure going from 1 to 0 ($\tau = 10\,\mathrm{s}$ and $f_{\max} = 3.8 \times 10^{-14}\,\mathrm{N}$). (b) For one procedure going from 0 to 0 ($\tau = 5\,\mathrm{s}$ and $f_{\max} = 3.8 \times 10^{-14}\,\mathrm{N}$). The black vertical lines indicate $Q = 0$ and the green ones indicate the Landauer's bound $k_B T \ln 2$.

2.4 Integrated Fluctuation Theorem applied on information erasure procedure

We have shown that the mean dissipated heat for an information erasure procedure applied on a 1 bit memory system approaches the Landauer's bound for quasi-static transformations. One may wonder if we can have direct access to the variation of free-energy between the initial and the final state of the system, which is directly linked to the variation of the system's entropy.

2.4.1 Computing the stochastic work

To answer this question it seems natural to use the Integrated Fluctuation Theorem called the Jarzinsky equality [33] which allows one to compute the free energy difference between two states of a system, in contact with a heat bath at temperature T. When such a system is driven from an equilibrium state A to a state B through any continuous procedure, the Jarzynski equality links the stochastic work W_{st} received by the system during the procedure to the free energy difference $\Delta F = F_B - F_A$ between the two states:

$$\left\langle \mathrm{e}^{-\beta W_{\mathrm{st}}} \right\rangle = \mathrm{e}^{-\beta \Delta F} \tag{2.16}$$

Where $\langle . \rangle$ denotes the ensemble average over all possible trajectories, and $\beta = \frac{1}{k_{\mathrm{B}} T}$.

For a colloidal particle confined in one spatial dimension and submitted to a conservative potential $V(x, \lambda)$, where $\lambda = \lambda(t)$ is a time-dependent external parameter, the stochastic work received by the system is defined by [31]:

$$W_{\mathrm{st}}[x(t)] = \int_0^t \frac{\partial V}{\partial \lambda} \dot{\lambda} \, \mathrm{d}t' \tag{2.17}$$

Here the potential is made by the double-well and the tilting drag force[6]

$$V(x, \lambda) = U_0(x, I(t)) - f(t)x \tag{2.18}$$

and we have two control parameters: $I(t)$ the intensity of the laser and $f(t)$ the amplitude of the drag force.

Once again, we can separate two contributions: one coming from the lowering and rising of the barrier, and one coming from the applied external drag force. We again consider that the lowering and rising of the barrier should not modify the free-energy of the system, and that the main contribution is due to the drag force. Thus:

$$W_{\mathrm{st}} = \int_{T_{\mathrm{low}}}^{T_{\mathrm{low}}+\tau} -\dot{f} x \, \mathrm{d}t' \tag{2.19}$$

Noting that $f(t = T_{\mathrm{low}}) = 0 = f(t = T_{\mathrm{low}} + \tau)$, it follows from an integration by parts that the stochastic work is equal to the heat dissipated by the drag force:

$$W_{\mathrm{st}} = \int_{T_{\mathrm{low}}}^{T_{\mathrm{low}}+\tau} -\dot{f} x \, \mathrm{d}t' = \int_{T_{\mathrm{low}}}^{T_{\mathrm{low}}+\tau} f \dot{x} \, \mathrm{d}t' = Q_{\mathrm{drag}} \tag{2.20}$$

The two integrals have been calculated experimentally for all the trajectories of all the procedures tested and it was verified that the difference between the two quantity is completely negligible. In the following parts, we write W_{st} for theoretic calculations, and Q_{drag} when we apply the calculations to our experimental data.

[6] As already mentioned, f is independent of x and can be seen as an extra potential term $-fx$. More generally, for a system in one dimension, any external force can be written as the gradient of a global potential.

2.4.2 Interpreting the free-energy difference

Since the memory erasure procedure is made in a cyclic way (which implies $\Delta U = 0$) and $\Delta S = -k_{\mathrm{B}} \ln 2$ it is natural to await $\Delta F = k_{\mathrm{B}} T \ln 2$. But the ΔF that appears in the Jarsynski equality is the difference between the free energy of the system in the initial state (which is at equilibrium) and the equilibrium state corresponding to the final value of the control parameter:

$$\Delta F_{\mathrm{Jarzynski}} = F(\lambda(t_{\mathrm{final}})) - F(\lambda(t_{\mathrm{initial}})) \tag{2.21}$$

Because the height of the barrier is always finite there is no change in the equilibrium free energy of the system between the beginning and the end of our procedure. Then $\Delta F_{\mathrm{Jarzynski}} = 0$, and we await $\left\langle \mathrm{e}^{-\beta W_{\mathrm{st}}} \right\rangle = 1$, which is not very interesting.

Nevertheless it has been shown [54] that, when there is a difference between the actual state of the system (described by the phase-space density ρ_t) and the equilibrium state (described by ρ_t^{eq}), the Jarzynski equality can be modified:

$$\left\langle \mathrm{e}^{-\beta W_{\mathrm{st}}(t)} \right\rangle_{(x,t)} = \frac{\rho^{\mathrm{eq}}(x, \lambda(t))}{\rho(x,t)} \mathrm{e}^{-\beta \Delta F_{\mathrm{Jarzynski}}(t)} \tag{2.22}$$

Where $\langle . \rangle_{(x,t)}$ is the mean on all the trajectories that pass through x at t.

In our procedure, selecting the trajectories where the information is actually erased is equivalent to fix the position x to the chosen final well (state 0 corresponds to $x < 0$) at the time $t = T_{\mathrm{low}} + \tau$. It follows that $\rho(x < 0, T_{\mathrm{low}} + \tau)$ is directly $P_{S\,\mathrm{force}}$, the proportion of success of the procedure, and $\rho^{\mathrm{eq}}(x < 0, \lambda(T_{\mathrm{low}} + \tau)) = 1/2$ since both wells have same probability at equilibrium[7]. Then:

$$\left\langle \mathrm{e}^{-\beta W_{\mathrm{st}}(T_{\mathrm{low}}+\tau)} \right\rangle_{\to 0} = \frac{1/2}{P_{S\,\mathrm{force}}} \tag{2.23}$$

Similarly for the trajectories that end the procedure in the wrong well (state 1) we have:

$$\left\langle \mathrm{e}^{-\beta W_{\mathrm{st}}(T_{\mathrm{low}}+\tau)} \right\rangle_{\to 1} = \frac{1/2}{1 - P_{S\,\mathrm{force}}} \tag{2.24}$$

Taking into account the Jensen's inequality, i.e. $\langle \mathrm{e}^{-x} \rangle \geq \mathrm{e}^{-\langle x \rangle}$, we find that equations 2.23 and 2.24 imply:

$$\begin{aligned} \langle W_{\mathrm{st}} \rangle_{\to 0} &\geq k_{\mathrm{B}} T \left[\ln(2) + \ln(P_{S\,\mathrm{force}}) \right] \\ \langle W_{\mathrm{st}} \rangle_{\to 1} &\geq k_{\mathrm{B}} T \left[\ln(2) + \ln(1 - P_{S\,\mathrm{force}}) \right] \end{aligned} \tag{2.25}$$

Given that the mean stochastic work dissipated to realise the procedure is simply:

$$\langle W_{\mathrm{st}} \rangle = P_{S\,\mathrm{force}} \langle W_{\mathrm{st}} \rangle_{\to 0} + (1 - P_{S\,\mathrm{force}}) \langle W_{\mathrm{st}} \rangle_{\to 1} \tag{2.26}$$

it follows:

$$\langle W_{\mathrm{st}} \rangle \geq k_{\mathrm{B}} T \left[\ln(2) + P_{S\,\mathrm{force}} \ln(P_{S\,\mathrm{force}}) + (1 - P_{S\,\mathrm{force}}) \ln(1 - P_{S\,\mathrm{force}}) \right] \tag{2.27}$$

which is the generalization of the Landauer's bound for $P_{S\,\mathrm{force}} < 100\,\%$. Hence, the Jarzynski equality applied to the information erasure procedure allows one to find the complete Landauer's bound for the stochastic work received by the system.

[7] A more detailed demonstration is given in Appendix 2.6.

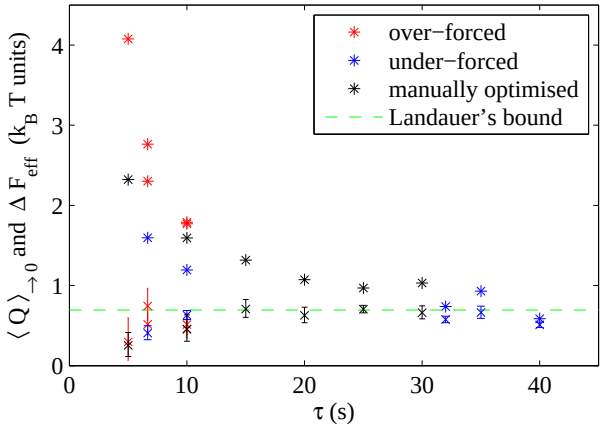

Figure 2.10: Mean dissipated heat ($*$) and effective free energy difference ($\times$) for several procedures, with fixed τ and different values of $f_{\max}$. The red points have a force too high, and a $P_{S\,\text{force}} \geq 99\,\%$. The blue points have a force too low and $91\,\% \leq P_{S\,\text{force}} < 95\,\%$ (except the last point which has $P_{S\,\text{force}} \approx 80\,\%$). The black points are considered to be optimised and have $95\,\% \leq P_{S\,\text{force}} < 99\,\%$.

Finally we experimentally compute ΔF_{eff} which is the logarithm of the exponential average of the dissipated heat for trajectories ending in state 0:

$$\Delta F_{\text{eff}} = -\ln\left(\left\langle \mathrm{e}^{-\beta Q_{\text{drag}}}\right\rangle_{\to 0}\right). \tag{2.28}$$

Data are shown in figure 2.10. The error bars are estimated by computing the average on the data set with 10% of the points randomly excluded, and taking the maximal difference in the values observed by repeating this operation 1000 times. Except for the first points[8] ($\tau = 5\,\text{s}$), the values are very close to $k_{\text{B}}T\ln 2$, which is in agreement with equation 2.23, since $P_{S\,\text{force}}$ is close to $100\,\%$. Hence, we retrieve the Landauer's bound for the free-energy difference, for any duration of the information erasure procedure.

Note that this result is not in contradiction with the classical Jarzynski equality, because if we average over all the trajectories (and not only the ones where the information is erased), we should find:

$$\left\langle \mathrm{e}^{-\beta W_{\text{st}}}\right\rangle = P_{S\,\text{force}}\left\langle \mathrm{e}^{-\beta W_{\text{st}}}\right\rangle_{\to 0} + (1 - P_{S\,\text{force}})\left\langle \mathrm{e}^{-\beta W_{\text{st}}}\right\rangle_{\to 1} = 1. \tag{2.29}$$

However, the verification of this equality is hard to do experimentally since we have very few trajectories ending in state 1, which gives us not enough statistics to estimate $\left\langle \mathrm{e}^{-\beta W_{\text{st}}}\right\rangle_{\to 1}$ properly.

2.4.3 Separating sub-procedures

To go further, we can also look at the two sub-procedures $1 \to 0$ and $0 \to 0$ separately. To simplify calculations, we make here the approximation that $P_{S\,\text{force}} = 100\,\%$.

[8] We believe that the discrepancy can be explained by the fact that the values of $Q_{\text{drag}\to 0}$ are bigger and that it is more difficult to estimate correctly the exponential average in this case.

We can compute the exponential average of each sub-procedure:

$$M_{1\to0} = \left\langle \mathrm{e}^{-\beta W_{\mathrm{st}}} \right\rangle_{1\to0} \quad \text{and} \quad M_{0\to0} = \left\langle \mathrm{e}^{-\beta W_{\mathrm{st}}} \right\rangle_{0\to0} \tag{2.30}$$

For each sub-procedure taken independently the classical Jarzynski equality does not hold because the initial conditions are not correctly tested. Indeed selecting trajectories by their initial condition induces a bias in the initial equilibrium distribution. But it has been shown [55] that for a partition of the phase-space into non-overlapping subsets χ_j $(j = 1, ..., K)$ there is a detailed Jarzynski Equality :

$$\left\langle \mathrm{e}^{-\beta W_{\mathrm{st}}} \right\rangle_j = \frac{\tilde{\rho}_j}{\rho_j} \left\langle \mathrm{e}^{-\beta W_{\mathrm{st}}} \right\rangle \tag{2.31}$$

with:

$$\rho_j = \int_{\chi_j} \rho(t_a)\, \mathrm{d}x\mathrm{d}p \quad \text{and} \quad \tilde{\rho}_j = \int_{\tilde{\chi}_j} \tilde{\rho}(t_a)\, \mathrm{d}x\mathrm{d}p \tag{2.32}$$

where $\rho(t_a)$ and $\tilde{\rho}(t_a)$ are the phase-space densities of the system measured at the same intermediate but otherwise arbitrary point in time, in the forward and backward protocol, respectively. The backward protocol is simply the time-reverse of the forward protocol.

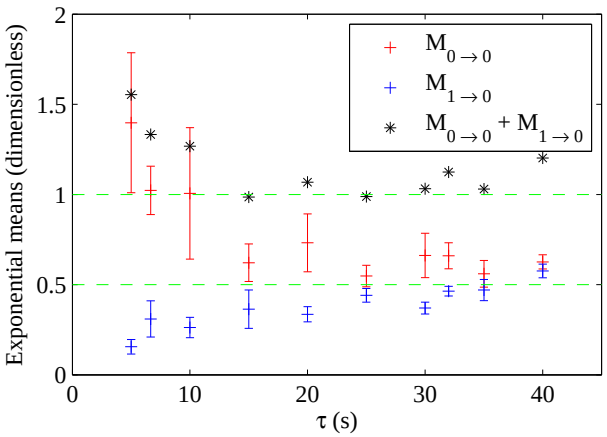

Figure 2.11: Exponential means computed on the sub-procedures, for several parameters, with fixed τ and manually optimised values of $f_{\max}$. The error bars are estimated by computing the exponential mean on the data set with 10% of randomly excluded points, and taking the maximal difference in the values observed by repeating this operation 1000 times.

Here, we take only two subsets $j = \{0 \to 0, 1 \to 0\}$, defined by the position where the bead starts, and we choose $t_a = T_{\mathrm{low}}$ the starting point of the applied force. Then we have:

$$M_{i\to0} = \frac{\tilde{\rho}_{i\to0}}{\rho_{i\to0}} \mathrm{e}^{-\beta \Delta F_{\mathrm{eff}}} = \frac{\tilde{P}_{0\to i}}{1/2}\, \frac{1}{2} \tag{2.33}$$

where $i = \{0, 1\}$ and $\tilde{P}_{0\to i}$ is the probability that the system returns to its initial state i under the time-reversed procedure (which always starts in state 0). Finally:

$$M_{1\to0} = \tilde{P}_{0\to1} \quad \text{and} \quad M_{0\to0} = \tilde{P}_{0\to0} \tag{2.34}$$

Experimental data are shown in figure 2.11. $M_{1\to0}$ is an increasing function of τ whereas $M_{0\to0}$ is decreasing with τ. Their sum is always close to 1 (which is the same result that gives $\Delta F_{\text{eff}} \approx k_{\text{B}}T\ln 2$), and $M_{1\to0}$ is always smaller than $M_{0\to0}$. These observations are intuitive because the work is higher when the bead jumps from state 1 to 0 than when it stays in state 0, and the work is higher when τ is smaller. The interpretation of eq. 2.34 gives a little more information. It is indeed reasonable to think that for time-reversed procedures the probability of returning to state 1 is small for fast procedures and increases when τ is bigger, whereas the probability of returning to state 0 increases when τ is smaller[9].

To be more quantitative one has to measure $\tilde{P}_{0\to1}$ and $\tilde{P}_{0\to0}$, but the time-reversed procedure cannot be realised experimentally, because it starts with a very fast rising of the force, which cannot be reached in our experiment. Thus, we performed numerical simulations, where it is possible to realise the corresponding time-reversed procedure and to compute $\tilde{P}_{0\to1}$ and $\tilde{P}_{0\to0}$. We simply integrate eq. 2.3 with Euler's method, for different set of parameters as close as possible to the experimental ones. The Gaussian white noise is generated by the "randn" function from Matlab® (normally distributed pseudorandom numbers). For each set of parameters we repeat the numerical procedure a few thousand times. Some results are shown in table 2.1 (values are estimated with error bar ±0.02):

τ (s)	$f_{\max}$ (fN)	$M_{1\to0}$	$\tilde{P}_{0\to1}$	$M_{0\to0}$	$\tilde{P}_{0\to0}$	P_S (%)	$P_{S\,\text{force}}$ (%)
5	37.7	0.17	0.16	0.86	0.84	97.3	99.8
10	28.3	0.29	0.28	0.74	0.72	96.6	99.3
20	18.9	0.42	0.41	0.63	0.59	94	97.1
30	18.9	0.45	0.43	0.59	0.57	94.4	97.7

Table 2.1: Results for simple numerical simulations of the experimental procedure.

All the qualitative behaviours observed in the experimental data are retrieved, and the agreement between $M_{i\to0}$ and $\tilde{P}_{0\to i}$ is correct. It was also verified that for proportions of success $< 100\,\%$, if one takes all the trajectories, and not only the ones where the bead ends in the state 0, the classical Jarzynski equality is verified: $\left\langle \mathrm{e}^{-\beta W_{\text{st}}} \right\rangle = 1$. This result means that the small fraction of trajectories where the bead ends the erasure procedure where it shouldn't is enough to retrieve the fact that $\Delta F_{\text{Jarzynski}} = 0$. And it is verified even if this fraction represent less than $1\,\%$ of all the trajectories.

[9] Of course $\tilde{P}_{0\to1} + \tilde{P}_{0\to0} = 1$.

2.5 Conclusion

In conclusion, we have realised an experimental information erasure procedure with a 1-bit memory system, made of a micro-particle trapped in a double well potential with optical tweezers. The procedure uses an external drag force to reset the memory of the system in one state, *i.e.* erase the knowledge of previous state and lose information. We measured the proportion of success of erasure procedures with different durations τ and amplitudes of the force $f_{\max}$. These data were used to manually optimise the procedure, *i.e.* for a fixed τ we found the lowest force which gives a good erasure of information. By varying the duration of the information erasure procedure τ, we were able to approach the Landauer's bound $k_{\mathrm{B}}T\ln 2$ for the mean dissipated heat by the system $\langle Q\rangle$. We have also shown that $\langle Q\rangle$ seems to decrease as $1/\tau$, which is in agreement with the theoretical prediction for an optimal information erasure procedure [56], and was later confirmed experimentally with a more controlled experimental system [51].

We have computed the stochastic work received by the system during the procedure, which is in our particular case equal to the heat dissipated by the action of the external force. We used a modified version of the Jarzynski equality [54] for systems ending in a non-equilibrium state to retrieve the generalised Landauer's bound for any proportion of success on the mean stochastic work received by the system. This relation has been tested experimentally, and we have shown that the exponential average of the stochastic work, computed only on the trajectories where the information is actually erased, reaches the Landauer's bound for any duration of the procedure.

We also used a detailed version of the Jarzynski equality [55] to independently consider each sub-procedure where the information is erased ($1 \to 0$ and $0 \to 0$). This relation allowed us to link the exponential average of stochastic work, computed only on a subset of the trajectories (corresponding to one of the sub-procedures), to the probability that the system returns to its initial state under a time-reversed procedure. We have shown that the experimental data are qualitatively in agreement with this interpretation. Finally, we used some very simple numerical simulations of our experimental procedure to compare quantitatively the partial exponential averages to the probabilities that the system returns to its initial state under time-reversed procedures.

2.6 Appendix

Equation 2.23 is obtained directly if the system is considered as a two state system, but it also holds if we consider a bead that can take any position in a continuous 1D double potential along the x-axis. We place the reference $x = 0$ at the center of the double potential.
Equation 2.22 states:

$$\left\langle \mathrm{e}^{-\beta W_{\mathrm{st}}(t)} \right\rangle_{(x,t)} = \frac{\rho^{\mathrm{eq}}(x, \lambda(t))}{\rho(x,t)} \mathrm{e}^{-\beta \Delta F_{\mathrm{Jarzynski}}(t)} \tag{2.35}$$

where $\langle . \rangle_{(x,t)}$ is the mean on all the trajectories that pass through x at t.
We choose $t = T_{\mathrm{low}} + \tau$ the ending time of the procedure, and we will not anymore write the explicit dependence upon t since it's always the same chosen time. We recall that $\Delta F_{\mathrm{Jarzynski}} = 0$ at $t = T_{\mathrm{low}} + \tau$ for our procedure.
We define the proportion of success, which is the probability that the bead ends its trajectory in the left half-space $x < 0$:

$$P_{S\,\mathrm{force}} = \rho(x < 0) = \int_{-\infty}^{0} \mathrm{d}x\, \rho(x) \tag{2.36}$$

The conditional mean is given by:

$$\left\langle \mathrm{e}^{-\beta W_{\mathrm{st}}} \right\rangle_{x} = \int \mathrm{d}W_{\mathrm{st}}\, \rho(W_{\mathrm{st}}|x) \mathrm{e}^{-\beta W_{\mathrm{st}}} \tag{2.37}$$

where $\rho(W_{\mathrm{st}}|x)$ is the conditional density of probability of having the value W_{st} for the work, knowing that the trajectory goes through x at the chosen time $T_{\mathrm{low}} + \tau$.
We recall from probability properties that:

$$\rho(W_{\mathrm{st}}|x) = \frac{\rho(W_{\mathrm{st}}, x)}{\rho(x)} \tag{2.38}$$

where $\rho(W_{\mathrm{st}}, x)$ is the joint density of probability of the value W_{st} of the work and the position x through which the trajectory goes at the chosen time $T_{\mathrm{low}} + \tau$.
We also recall:

$$\rho(W_{\mathrm{st}}|x < 0) = \frac{\int_{-\infty}^{0} \mathrm{d}x\, \rho(W_{\mathrm{st}}, x)}{\int_{-\infty}^{0} \mathrm{d}x\, \rho(x)} = \frac{\int_{-\infty}^{0} \mathrm{d}x\, \rho(W_{\mathrm{st}}, x)}{P_{S\,\mathrm{force}}} \tag{2.39}$$

Then by multiplying equation 2.35 by $\rho(x)$ and integrating over the left half-space $x < 0$ we have:

$$\int_{-\infty}^{0} \mathrm{d}x\, \rho(x) \left\langle \mathrm{e}^{-\beta W_{\mathrm{st}}} \right\rangle_{x} = \int_{-\infty}^{0} \mathrm{d}x\, \rho^{\mathrm{eq}}(x) \tag{2.40}$$

Since the double potential is symmetric:

$$\int_{-\infty}^{0} \mathrm{d}x\, \rho^{\mathrm{eq}}(x) = \frac{1}{2}. \tag{2.41}$$

By applying definition 2.37 and equality 2.38, it follows:

$$\int_{-\infty}^{0} \mathrm{d}x \int \mathrm{d}W_{\mathrm{st}}\, \rho(W_{\mathrm{st}}, x) \mathrm{e}^{-\beta W_{\mathrm{st}}} = \frac{1}{2} \tag{2.42}$$

Then using equality 2.39:

$$P_{S\,\text{force}} \int \mathrm{d}W_{\text{st}}\, \rho(W_{\text{st}}|x<0)\mathrm{e}^{-\beta W_{\text{st}}} = \frac{1}{2} \tag{2.43}$$

Finally we obtain:

$$\left\langle \mathrm{e}^{-\beta W_{\text{st}}} \right\rangle_{x(T_{\text{low}}+\tau)<0} = \frac{1/2}{P_{S\,\text{force}}} \tag{2.44}$$

which is equation 2.23 of the main text.

Chapter 3

(Absence of) Effective Temperature in Gelatin after a Fast Quench

En essayant continuellement on finit par réussir. Donc : plus ça rate, plus on a de chances que ça marche.

Devise Shadok

3.1 Introduction and Motivations

3.1.1 Gelatin and the sol-gel transition

Gelatin is a thermoreversible gel [57]. It is a heterogeneous mixture of water-soluble denatured collagen protein chains, extracted by boiling animal by-products (skin, tendons, ligaments, bones, etc.) in water. Collagen molecules are rods of 300 nm length, made of three strands, with high average molecular weights. This triple-helix structure is stabilised by hydrogen bonds and has a diameter of ~ 1.4 nm. The chemical treatment used to produce gelatin breaks crosslinks between strands, but can also hydrolyse strands into fragments. Thus a broad molecular weight distribution is obtained for gelatin [58, 59].

Above a temperature $T_{\text{melt}} \sim 40\,^{\circ}\text{C}$, the gelatin chains are in coil conformation. The gelatin solution is in a viscous liquid phase, called "sol" phase. Below a temperature $T_{\text{gel}} \sim 30\,^{\circ}\text{C}$ renaturation of the native triple helix structure occurs, and chains form a percolating three-dimensional network of helical segments connected by single strand coils. The gelatin solution is in an arrested state with elastic behaviour, called "gel" phase. The coil-helix transition is completely reversible and the transition from one phase to the other is called the "sol-gel" transition [57].

Physical properties of the sol phase, and of the sol-gel transition are studied in [60, 61] for different gelatin concentrations above 4 wt%. In particular, it was seen that there are at least three successive steps in the transition: monomer to aggregate formation, random-coil-single-helix transition (disorder-order transition), and single-helix-triple-helix transition (order-order transition). It is then possible to identify different phase states in the sol domain: the sol state

I where the chains have random coil conformations and the sol state II where single and triple helices begin to form (without reaching gelation).

The gel phase was also shown to share properties with glassy materials, which are out-of-equilibrium metastable systems. After a quench at $T < T_{\text{gel}}$ the system is frustrated by topological constraints because each gelatin chain is involved in at least two helices, and neighbouring helices are competing for the shared portions of non-helical chain. Therefore, the system displays physical aging: its physical properties slowly evolve with time, through a process known as structural recovery. For example, the small-strain shear modulus of a 5 wt% gelatin solution quenched at 20 °C increases logarithmically as a function of the ageing time [62]. And the elasticity of gelatin gels during slow cool and heat cycles exhibits memory and rejuvenation effects similar to the ones found in spin glasses [63].

Although it is known that mechanical properties of gelatin gels are very sensitive to temperature variations, previous thermal history of the gel, and time, this system has some interesting experimental features:

- The fact that the transition is thermoreversible allows us to do melting/gelation cycles simply by controlling the temperature of the sample.
- The ageing rate can in theory be controlled by changing the quench depth.
- The length-scale of the collagen chains (300 nm) is big enough to be sensed by a microparticle of 2 µm.

This particular sol-gel transition was chosen for previous works done in the laboratory about fluctuations of Brownian particles in quenched gelatin samples [64–66].

A summary of the previous works results and our motivations are presented in the next section.

3.1.2 Previous work: anomalous variance, heat flux and Fluctuation Dissipation Theorem violation in an ageing bath

Previous works [64–66] showed that a particle trapped with optical tweezers in a liquid droplet of gelatin solution, quenched at a temperature below T_{gel} exhibits anomalously high position fluctuations right after the quench. These anomalous fluctuations can be interpreted as an effective temperature, which motivated us to look at the interactions of two particles trapped in the same gelatin droplet, undergoing sol-gel transition after a quench. Indeed if two particles are trapped at two different positions in the same gelatin droplet, they could sense different effective temperatures. Our aim was therefore to see the effect of these different temperatures on two particles interacting through the surrounding fluid.

We reproduce here some figures from [64–66] and recall the associated key results:

- The variance of the position exhibits anomalously high value for short times (~ 5 s) right after the quench, then stabilises at the equipartition value $k_{\text{B}}T/k$ for ~ 200 s, and finally decreases logarithmically for long times after the quench. See figure 3.1a.
- The Probability Distribution Functions of position fluctuations are Gaussian at any time after the quench, but their variances decreases with time (in agreement with previous result). See figure 3.1b.

- The Probability Distribution Function of the heat exchanged between the particle and the bath during short times after the quench is asymmetrical. See figure 3.2.
- The Fluctuation Dissipation Theorem is violated only for short times after the quench, and this violation can be linked with the amount of heat exchanged between the particle and the bath during the same time. See figure 3.3.

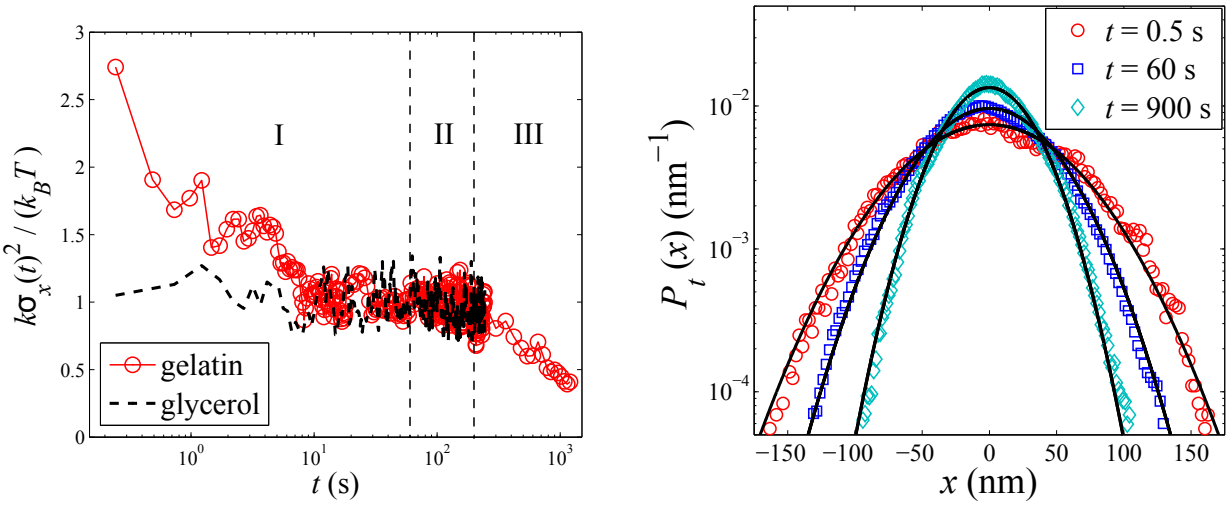

(a) (b)

Figure 3.1: (a) Evolution of the normalised variance of the position fluctuations of one particle trapped in gelatin solution (10 wt%) or glycreol, quenched at 26 °C, for different times t after the quench. (b) Evolution of the Probability Distribution Function of the position fluctuations of the particle trapped in gelatin solution.

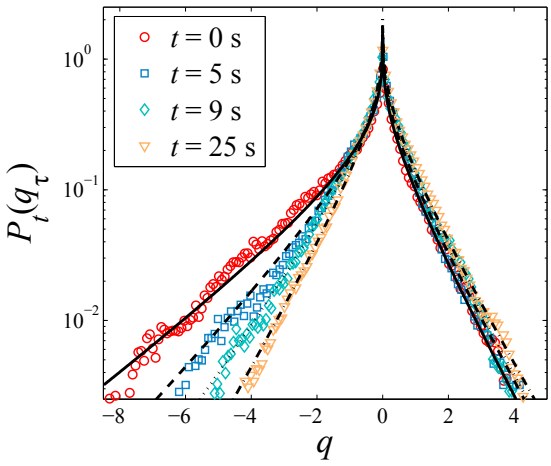

Figure 3.2: Probability Density Function of the normalised heat q exchanged during $\tau = 30$ s computed at different times t after the quench in gelatin.

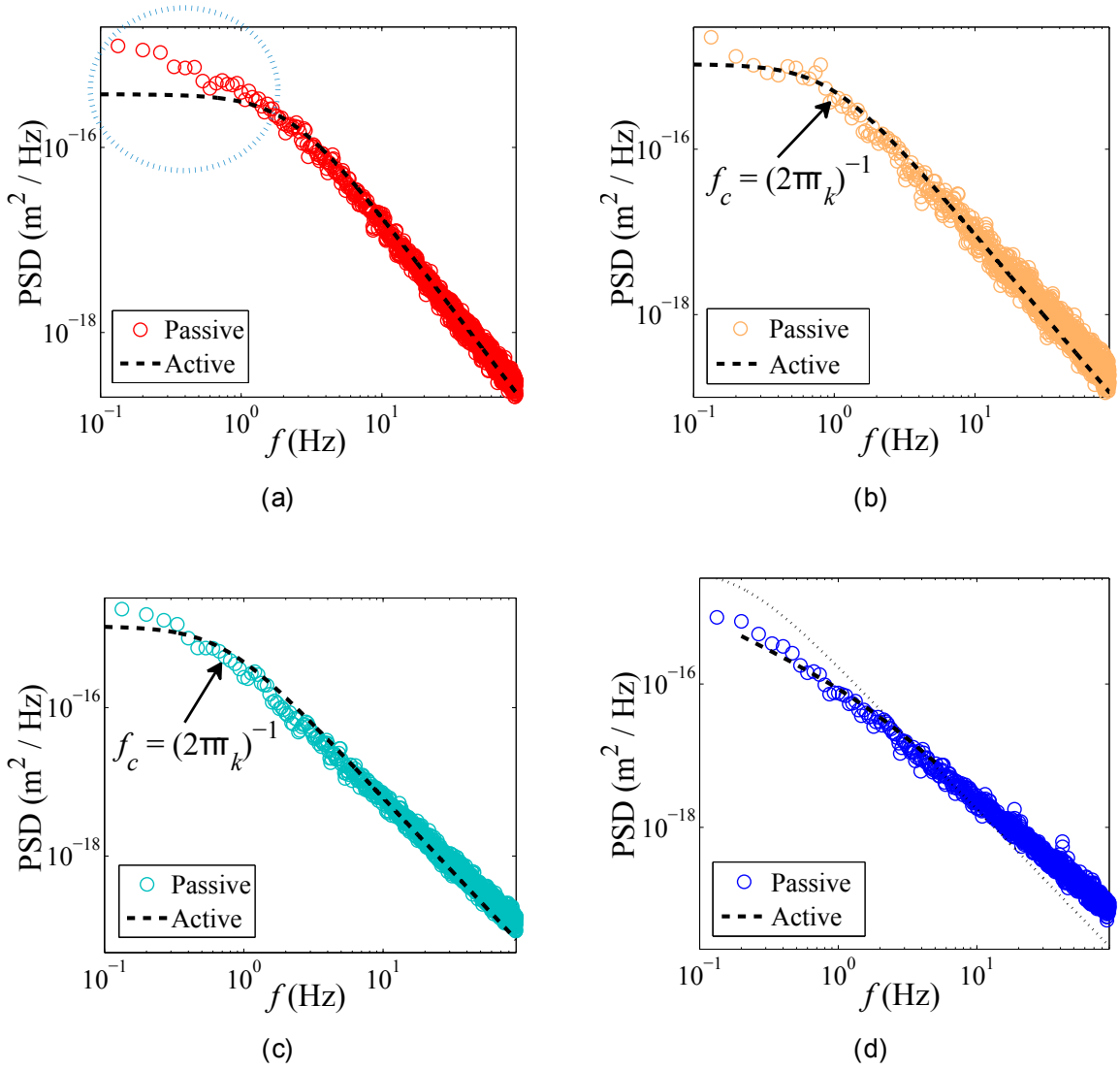

Figure 3.3: Passive Power Spectral Densities of the position fluctuations (color points) and Fourier transform of the active response function (black dashed-lines) computed at different times after the quench. (a) For $0\,\mathrm{s} < t < 15\,\mathrm{s}$. (b) For $30\,\mathrm{s} < t < 45\,\mathrm{s}$. (c) For $75\,\mathrm{s} < t < 90\,\mathrm{s}$. (d) For $1200\,\mathrm{s} < t < 1215\,\mathrm{s}$. If the Fluctuations Dissipation Theorem is verified, the two quantities should be equal, which is not the case for low-frequency in (a).

Unfortunately, none of those key results was found to be reproducible, and we believe that they were only due to an artefact in the data and/or in the analysis method. Therefore, we present in this chapter a detailed and careful analysis of trajectories of particles trapped in a droplet of gelatin solution quenched at a temperature below T_{gel}. We show that there is indeed no effective temperature for this system.

3.2 Experimental set-up

3.2.1 Gelatin sample preparation

We use gelatin powder from porcine skin, produced by Sigma-Aldrich®: gel strength ∼ 300 g Bloom, Type A, BioReagent, suitable for cell culture. This gelatin is derived from acid-cured tissue, whereas type B is derived from lime-cured tissue.

We work with gelatin at a weight concentration of 5 wt%. The samples are prepared following a standard protocol [67]: the wanted amount of powder is dissolved in bidistilled water, which is then heated for ∼ 30 min at ∼ 60 °C while slowly stirred until the solution is transparent and homogeneous. While the solution is still liquid, ∼ 2 mL are filtered using a Millex® syringe driven filter unit with 0.45 µm pore size mixed cellulose esters membrane. Then 15 µL of an aqueous solution of silica beads (radius $R = 1.00 \pm 0.05$ µm) with concentration 10^7 particle · mL^{-1} are added, and the solution is strongly agitated. The non-filtered and final solutions are then let gelify at room temperature and kept in the refrigerator for later use.

We use the disk-shape glass cell, already described in 1.1.2, with an Indium Tin Oxyde (ITO) coated microscope slide, a free-volume to avoid problems if the volume of solution changes during gelation, and a *Wavelength Electronics* TCS10K5 thermal sensor for temperature measurement (see figure 3.4). To fill the cell, the gelatin solution with dispersed silica particles is taken from the refrigerator and heated at ∼ 50 °C until it is in the sol phase.

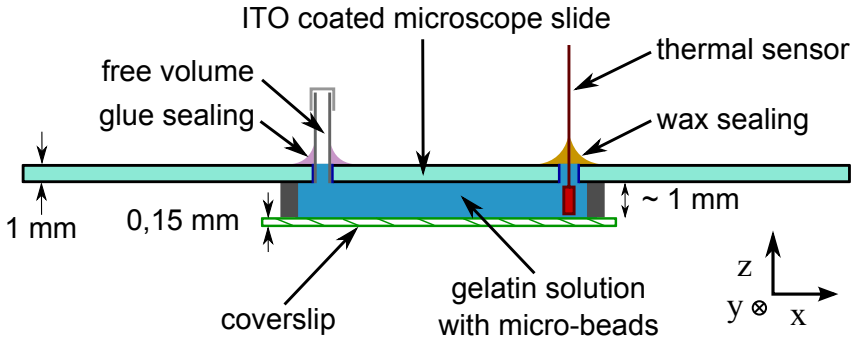

Figure 3.4: Schematic representation of the cell used to trap particles in gelatin solution (view from the side). The microscope slide is ITO-coated, which enables us to heat the cell by sending an electrical current through the glass surface.

3.2.2 Optical trapping and controlled gelation

For different purposes we used two variations of the optical tweezers set-ups described in 1.1.3:

The first set-up uses a laser beam ($\lambda = 532$ nm) separated in two cross-polarised beams which enables us to have two traps with no interference between them. A laser diode ($\lambda = 980$ nm) is aligned with the green laser and used to heat locally the sample. The tracking is done using a fast camera which is able to track two particles at 600 Hz. By previously using a calibration target, we can directly convert the displacement of the particles from pixels to µm. See figure 3.5.

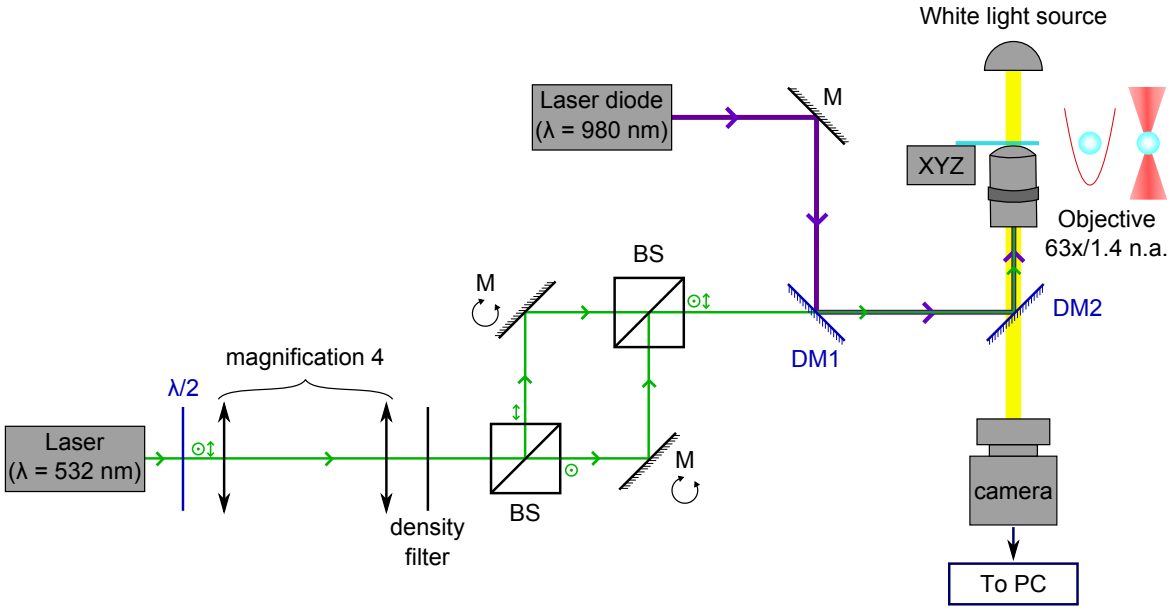

Figure 3.5: Schematic representation of optical tweezers set-up used to trap two particles in gelatin solution with a green laser. An infrared laser diode is used to melt the gelatin. "BS" are beam-splitters, "M" are mirrors and "DM" are dichroic mirrors.

The second set-up uses a single laser diode ($\lambda = 980\,\text{nm}$) to trap the particle and to heat locally the sample. A He-Ne laser ($\lambda = 632.8\,\text{nm}$) is aligned with the laser diode and deflected by the particle. This deflection is measured using a position sensing diode which is able to track one particle at more than 10 kHz. The position signal is in arbitrary unit and a supplementary calibration is needed for each measurement to convert the trajectory of the particle in physical units. See figure 3.6.

For both set-ups, the microscope objective is an oil-immersion *Leica* HCX PL. APO ×63 with high numerical aperture $N.A. = 1.4$. The microscope objective is surrounded with a custom-made heating ring, made with a *Minco* flexible resistor and a *Wavelength Electronics* TCS10K5 thermal sensor for temperature measurement. A feedback control is managed by the temperature control module (TCM-39032) of a modular laser diode controller (ILX Lightwave LDC-3900). As already mentionned, another thermal sensor is inserted directly inside the cell (see figure 3.4) and another feedback control is done by mastering the current going through the ITO-coated microscope slide, with an *Instec* MK1 Board and a PID software. These two temperature devices ensure that the temperature of both the microscope objective and the cell are well controlled. The precision achieved on the temperature control is about $\pm 0.05\,°\text{C}$.

To trap particles, the temperature of both the microscope objective and the cell are set to 38 °C so that the gelatin is in the sol phase. Then, one or two (depending on the set-up used) particles are found and trapped at a given distance from the bottom surface of the cell (typically $h = 15\,\mu\text{m}$). Then, the temperature controls are set to a value below the gel transition (typically $T_{\text{fb}} = 27\,°\text{C}$) and the sample is let gelify for a few hours (typically between 6 and 10 hours). Since the gelatin shows a lot of hysteretic behaviour [58,59], this gelation procedure appears to be important and the rheology of the gel can vary if the gelifying time is very different (*e.g.* a few days). Moreover, one must pay attention to regularly check the distance between the bead

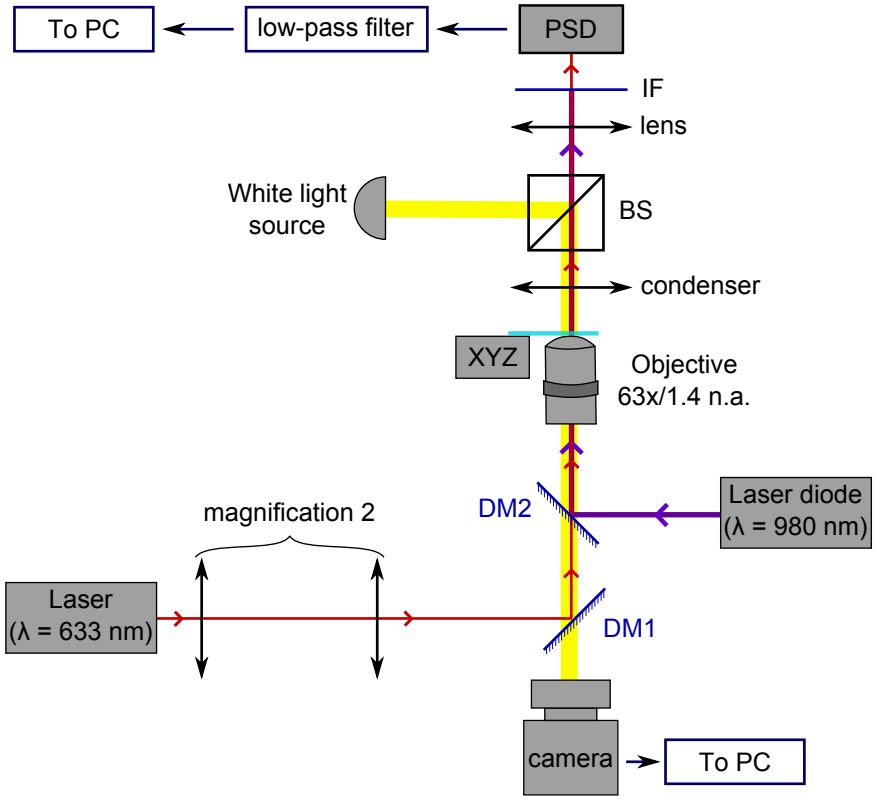

Figure 3.6: Schematic representation of optical tweezers set-up to trap one particle in gelatin solution. An infrared laser diode is used to trap and to melt the gelatin. The deflection of a He-Ne laser induced by the trapped bead is measured by the position sensing diode (PSD). The white light source and camera are only used for direct visualisation but not for the measurements. "BS" is a beam-splitter, "IF" and interferencial filter to suppress the infrared beam and "DM" are dichroic mirrors.

and the bottom surface of the cell, since the focal distance of the microscope objective always drifts slowly when its temperature is changing.

The refractive index of the liquid gelatine solution was measured $n_{\text{gel}} = 1.3415$, which is close to value in water $n_{\text{water}} = 1.3335$. It follows that the trapping stiffnesses in gelatin solution should be close to the ones in water with same experimental parameters.

3.2.3 Local heating and fast quenching method

When the particles are trapped and the sample is properly gelified at a given controlled temperature $T_{\text{fb}} < T_{\text{gel}}$, the local quenches are done in a similar way than the one presented in [64–66]: The power of the 980 nm laser diode is risen to a high value (typically[1] 230 mW) during a given time (typically $\tau_{\text{melt}} = 200\,\text{s}$). Because of the light absorption of the water molecules in the solution, the temperature of the gelatin around the particle (which is at the focal point of the

[1]This is the power measured on the beam before the microscope objective, so the "real" power at the focal point should be smaller, due to the loss in the objective.

microscope objective) increases by a small amount δT. Following the formula in reference [68]:

$$\delta T = \frac{P\alpha}{2\pi K}\left[\ln\left(\frac{2\pi h}{\lambda}\right) - 1\right] \tag{3.1}$$

where $\alpha = 50\,\mathrm{m}^{-1}$ is the attenuation coefficient of water at 27 °C for wavelength 980 nm [69], and $K = 0.61\,\mathrm{Wm}^{-1}\mathrm{K}^{-1}$ is the thermal conductivity of water. Here, we await:

$$\delta T \simeq 11\,^{\circ}\mathrm{C}. \tag{3.2}$$

This increase in temperature is only roughly estimated. Especially because we don't really know what is the absorption of the microscope objective for the near infrared, and because it is impossible to measure the temperature with a usual probe on this very small scale. But it is seen that the increase is strong enough to melt a small droplet of gelatin (radius $R_\mathrm{d} \sim 10\,\mu\mathrm{m}$) around the bead. Then, the power is quickly decreased to a low value (in the case where the same laser diode is used to trap and heat) or to zero (in the case where another laser is used to trap the particles), and the sample is let gelify for a given time (typically $\tau_\mathrm{rest} = 500\,\mathrm{s}$). Since the thermal diffusivity of water is $\kappa = 0.143 \times 10^{-6}\,\mathrm{m}^2 \cdot \mathrm{s}^{-1}$ at 25 °C, the time τ_κ needed to dissipate the heat from the droplet to the bulk is short:

$$\tau_\kappa \sim \frac{R_\mathrm{d}^2}{\kappa} \sim 2 \times 10^{-4}\,\mathrm{s}. \tag{3.3}$$

Hence, the gelatin is believed to experience a fast quench at temperature $T_\mathrm{fb} < T_\mathrm{gel}$ and should start ageing[2]. After the resting time τ_rest at low temperature T_fb, the power of the laser diode is risen again, and another quench is done. Note that the exact duration of τ_rest was not considered as important, because it was believed that the melting "resets" the gelatin sample and that all the anomalous behaviour occurs right after the quench.

The position(s) of the particle(s) trapped in the center of the melted droplet are continuously measured during a succession of several melting and ageing. For each measurement the quenching is repeated a few hundred times in order to perform proper ensemble averages.

An example of trajectory obtained with the second set-up is presented in figure 3.7. When the intensity of the laser is high, the gelatin droplet is in the "sol" phase and the particle is fluctuating in an optical trap with a high stiffness. When the intensity of the laser is low, the gelation is occurring and the stiffness of the trap is low (which is the reason why the position fluctuations are bigger).

[2] Actually, in the case where the same laser diode is used for trapping and melting the droplet, the temperature of the quench is a little bit above T_fb because of the absorption of the laser. Since the power of the laser is low, this increase is less than 1 °C and can easily be compensated by lowering T_fb accordingly.

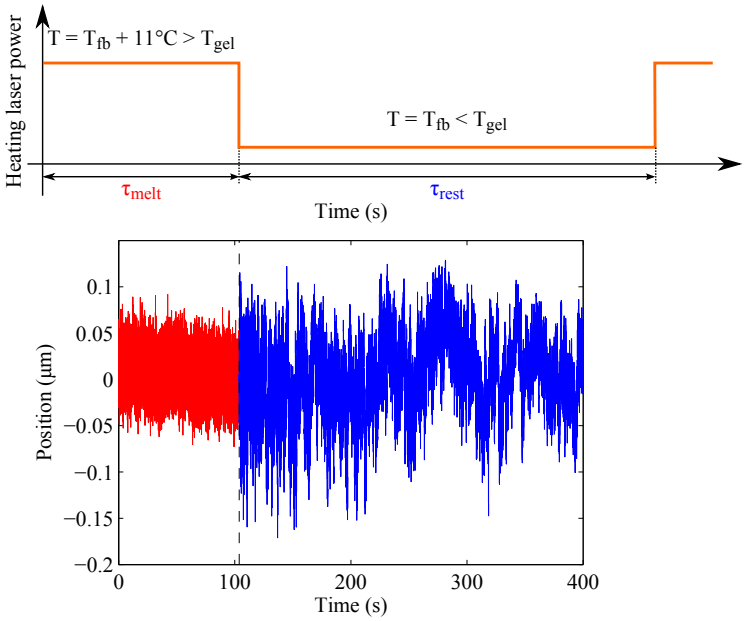

Figure 3.7: Trajectory of one particle trapped in gelatin sample kept at $T_{\mathrm{fb}} = 27.5\,^{\circ}\mathrm{C}$, around the quench. On the red part of the trajectory, the intensity of the laser is high and the gelatin droplet is liquid. On the blue part, the intensity of the laser is low and the gelation is occuring.

3.3 Results

In this section we present some results showing that there is no anomalous fluctuation occurring in the ageing of gelatin solution right after a fast quench. We also discuss why this effect that was previously observed is likely to actually be an artefact due to data analysis. Since our aim was to see the effect of the anomalous fluctuations on two coupled particles, some of the measurements were made with two particles, even though it might seem *a posteriori* that a single particle would have been enough.

3.3.1 Time evolution of bulk properties and hysteresis

We first did preliminary measurement of gelatin gelation in bulk (*i.e.* without the local heating method). We prepare a cell with gelatin solution as described in 3.2.1. We set the temperature controls of both the objective and of the cell at 37 °C for 30 min to melt the gelatin. We trap two particles and we switch both temperature controls to a given temperature T_{fb}. We wait a few tens of minutes (typically ~ 30 min) and we set the distance between the particles and the bottom of the cell when there is no more drift due to thermal expansion of the microscope objective. After that, we measure the positions of the two trapped beads for a long time (*e.g.* 8 h) at 400 Hz to see the bulk gelation of the sample.

For all these measurements, the distance between the bead and the surface is $h = 15\,\mu\text{m}$. The liquid gelatin solution at 37 °C is a Newtonian fluid, and the stiffness k of the trap can be computed directly from the variance of the position x of the bead[3]:

$$\sigma_x^2 = \left\langle x^2 \right\rangle = \frac{k_{\text{B}}T}{k} \tag{3.4}$$

For all these measurement the stiffness of the trap was $k = 0.46 \pm 0.01\,\text{pN}/\mu\text{m}$.

Since the T_{gel} is expected to be around 29 °C, we varied T_{fb} from 31 °C to 27.5 °C. It was found that above 28.5 °C, the gelation does not occur on the time of the experiment and the solution stays liquid, even if its viscosity increases continuously. Below 28.3 °C, the gelation occurs before the end of the experiment. It was estimated that the bulk gelation of the cell volume takes ~ 260 min at 28.3 °C and ~ 120 min at 27.5 °C.

Estimating the state ("sol" or "gel") of the gelatin solution, is not trivial, since the fluid can be really viscous without being completely gelified. Qualitatively, the trajectory of the trapped bead starts to be heckled, and the bead sometimes escapes the trapping (see figure 3.8). An *a posteriori* test consists in switching off the laser (resulting in switching off the trapping) and letting the sample at T_{fb} for a few more hours (typically over night) to see if the particle slowly fall to the bottom of the cell. If the particle does not fall, the gelatin solution is considered to be fully gelified.

To estimate the evolution of the viscosity during the gelation process, we used passive microrheology techniques [71]. The trajectories were divided in portions of ~ 1 h, and the Power Spectral Density (PSD) was computed for each portion. A long trajectory is required because we need low frequencies to correctly estimate the PSD. We explicitly assume that the bulk ageing is slow enough for not perturbing too much the estimation of the PSD when a long trajectory is taken. Or at least, that taking a long time window will only smooth the rheology result.

[3] The hydrodynamical coupling between two bead in a Newtonian fluid at thermal equilibrium is known to let the variance unmodified. [70]

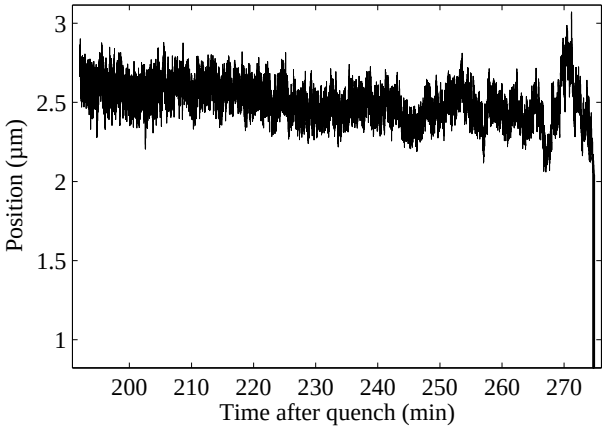

Figure 3.8: Evolution of the position of one trapped particle, in gelatin solution kept at 28.3 °C (after being melt at 37 °C for 20 min). At the end of the trajectory, gelation occurs and the particle is moved away from the optical trap.

As seen in figure 3.9a, shortly after the decrease of temperature, the PSD is still Lorentzian, as awaited for a particle trapped in a Newtonian fluid at equilibrium [23]. The mean viscosity term $\gamma = 6\pi R\eta$ (with η the dynamical viscosity of the solution) can be estimated from the value of the cut-off frequency $f_c = k/(2\pi\gamma)$. Here we find: $\eta = 21 \pm 1 \times 10^{-3}\,\mathrm{Pa \cdot s}$. As the gelation occurs, the PSD is less and less Lorentzian (see figure 3.9b), which is the sign that the gelatin solution starts to behave as a visco-elastic fluid [72].

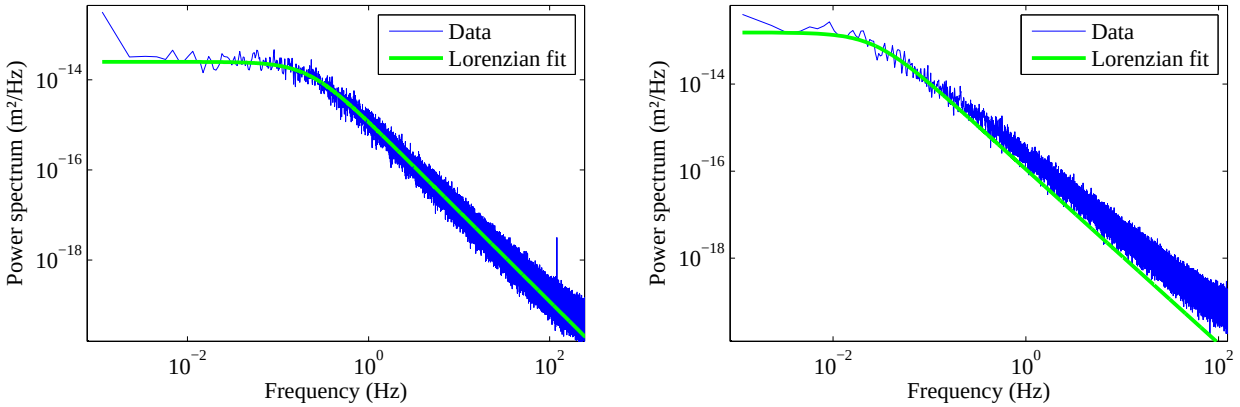

(a) 70 min after the temperature change.

(b) 320 min after the temperature change.

Figure 3.9: Power Spectral Density of the position of one particle trapped in gelatin solution kept at 28.5 °C (after being melt at 37 °C for 30 min). The PSD is estimated over a time window of 1 h. Shortly after switching the temperature the gelatin solution is still a Newtonian fluid and the PSD is Lorentzian. After some time, visco-elastic effects appear and the PSD is no longer Lorentzian.

We plot in figure 3.10 the evolution of the fitted cut-off frequency at different time after the gelatin solution was set at $T_{\mathrm{fb}} = 28.5\,°\mathrm{C}$. Even if the spectrum is no longer Lorentzian near the end of the measurement, it seems that the cut-off frequency decreases exponentially. Therefore,

the apparent viscosity increase is exponential.

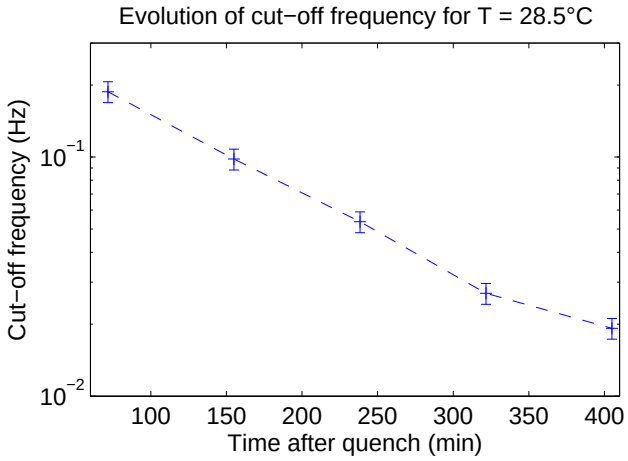

Figure 3.10: Evolution of the fitted cut-off frequency f_c, in gelatin solution kept at 28.5 °C (after being melt at 37 °C for 30 min).

From these preliminary measurements, we estimate that the T_{gel} is about 28.3 °C for our gelatin solution at 5 wt%. We chose to work with $T_{\text{fb}} < 28.3$ °C for all the following quenching experiments. As mentioned earlier, gelatin solutions have big hysteretic behaviour [58, 59]. It follows that the visco-elastic properties of the solution in an important temperature range around T_{gel} cannot be known independently of the sample's history.

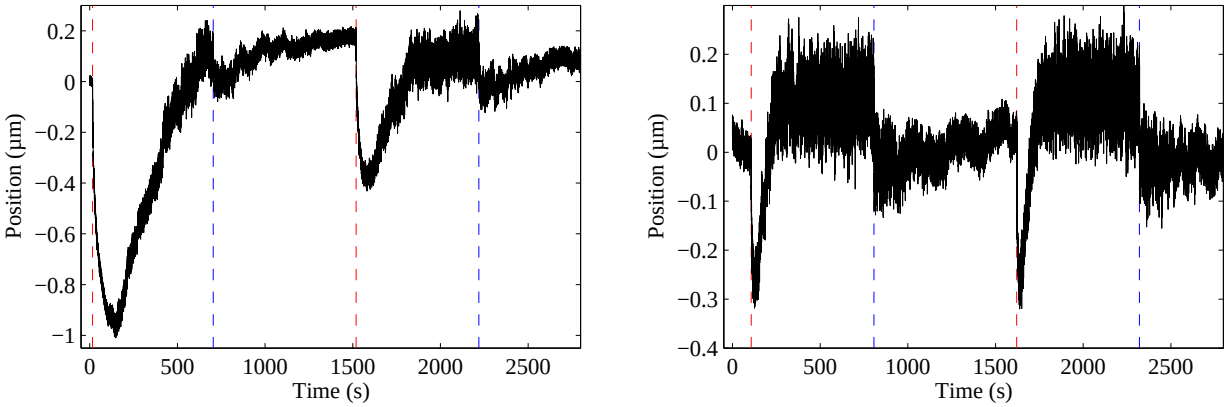

(a) First cycles.

(b) 3 h after starting the cycles.

Figure 3.11: Examples of trajectories for melting/regelifying cycles with a gelatine sample gelified at $T_{\text{room}} = 24$ °C for a long time. The red dashed-lines indicate when the heating laser is switched ON, and the blue ones when it is switched OFF. At the beginning, the melting is more difficult to reach, after a given time, the cycles look "reproducible".

Another consequence of the hysteretic behaviour is that the first bulk gelation of the sample must be done in a controlled and reproducible manner. If the sample is let gelify for a too long time, or at a too low temperature, the first melting/regelifying cycles used for the quenching experiment will be different from the following ones (where a "reproducible" state is reached).

Especially, in this case the first melting is more difficult to reach. Examples of trajectories are shown in figure 3.11. One can clearly see some position drifts occurring when the temperature is increased, before reaching a "sol" state where the particle fluctuates in the optical trap. Note that, contrary to figure 3.7, we use here the first set-up where the trapping laser is different from the heating laser. Hence, there is no change of the trap stiffness when the intensity of the heating laser is changed. The change of fluctuations amplitude when the heating laser is switched OFF is mostly due to the rapidly increase of gelatin viscosity when gelation occurs.

3.3.2 Difference between ensemble variance and temporal variance in the presence of a drift

We now consider quenching experiment as described in 3.2.3. We obtain several temporal trajectories of the particles positions for a given quenching temperature $T_{\text{fb}} < T_{\text{gel}}$. The important point is to estimate correctly the statistical properties from this set of data. In particular, we are interested in the variance of the position, which has been seen to have an anomalous increase right after the quench [64–66].

The correct ensemble variance should be estimated instantaneously at a given time t, by considering the N different trajectories at this time t. If one wants to increase the statistics by taking a small time windows δt, there are at least 3 ways to compute the variance from the set of trajectories. These different ways are schematically represented on figure 3.12. We call $x_i(t)$ the position of the particle for the i^{th} quench at the time t:

- The temporal variance σ^2_{time} is obtained by estimating the variance over the time δt for each quench, and then averaging over the N quenches:

$$\sigma^2_{\text{time}}(t) = \frac{1}{N}\sum_{i=1}^{N}\left[\frac{1}{\delta t}\int_t^{t+\delta t}\left(x_i(t') - \bar{x}_i(t)\right)^2 \,\mathrm{d}t'\right] \tag{3.5}$$

  where $\bar{x}_i(t) = \frac{1}{\delta t}\int_t^{t+\delta t} x_i(t')\,\mathrm{d}t'$ is the temporal mean of x for the i^{th} quench, between t and $t+\delta t$.

- The ensemble variance $\sigma^2_{\text{ensemble}}$ is obtained by estimating the variance over the N quenches at a time t and then averaging over the time window δt:

$$\sigma^2_{\text{ensemble}}(t) = \frac{1}{\delta t}\int_t^{t+\delta t}\left[\frac{1}{N-1}\sum_{i=1}^{N}\left(x_i(t') - \langle x(t')\rangle\right)^2\right]\mathrm{d}t' \tag{3.6}$$

  where $\langle x(t')\rangle = \frac{1}{N}\sum_{i=1}^{N} x_i(t')$ is the ensemble mean of the N trajectories $x_i(t')$ at time t'.

- The boxed variance σ^2_{box} is obtained by taking the N segments of trajectory from $x_i(t)$ to $x_i(t+\delta t)$, and then estimating the variance of the whole set of data:

$$\sigma^2_{\text{box}}(t) = \frac{1}{N\delta t}\sum_{i=1}^{N}\int_t^{t+\delta t}\left(x_i(t') - \boxed{x}(t)\right)^2 \,\mathrm{d}t' \tag{3.7}$$

  where $\boxed{x}(t) = \frac{1}{N\delta t}\sum_{i=1}^{N}\int_t^{t+\delta t} x_i(t')\,\mathrm{d}t'$ is the mean computed on the set of data made of the N segments from $x_i(t)$ to $x_i(t+\delta t)$. It is the variance used in references [64–66].

Nota Bene: Here to clearly distinguish the role of the time and the ensemble averages we have considered the time as a continuous variable and the number of trajectories as discrete. But experimentally the time is of course also a discrete variable, since we take measurements with a finite sampling frequency.

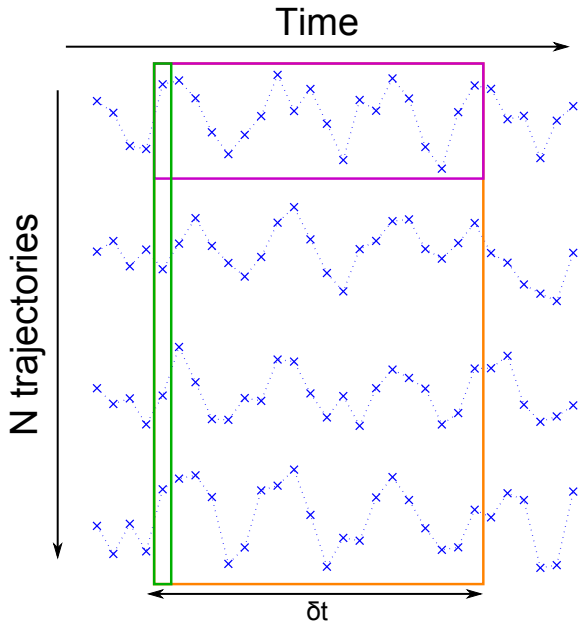

Figure 3.12: Schematic representation of the different ways to estimate the variance for a set of N trajectories with a time window δt. The temporal variance σ^2_{time} is computed by estimating the variance of the points in the fuschia box, and then averaging over the trajectories. The ensemble variance $\sigma^2_{\text{ensemble}}$ is computed by estimating the variance of the points in the green box, and then averaging over the time window δt. The boxed variance σ^2_{box} is computed directly by estimating the variance of all the points in the orange box.

If the system is at equilibrium and δt is big enough to correctly take account of the low-frequency of the motion, all these values should be equal to the equipartition value $k_{\text{B}}T/k$, with k_{B} the Boltzmann constant, T the temperature and k the trap's stiffness.

Unfortunately, when the system is non-stationary (which is the case for an ageing system), these 3 definitions of the variance are not equivalent. Especially, if there's a slow drift existing on each trajectory, the estimations that average over time (*i.e.* temporal and boxed variances) are likely to show a strong artefact.

To illustrate this effect, we have taken a set of 178 quenches done with the first set-up described in 3.2.2 at 28 °C, sampled at 400 Hz. The parameters were: melting time $\tau_{\text{melt}} = 250\,\text{s}$, melting intensity $I_{\text{melt}} = 235\,\text{W}$, resting time $\tau_{\text{rest}} = 305\,\text{s}$ and trap stiffness[4] $k = 3.7\,\text{pN/µm}$. One can clearly see on the trajectories that there is a small drift of $\sim 40\,\text{nm}$ which occurs right after the quench (see figure 3.13). Such a drift is often seen for this kind of measurement. We interpret it as a slow relaxation of the gel network, which occurs on a time much smaller than the gelation, but much greater than the heat dissipation. In other words, when the gelation

[4]The trap stiffness is measured when the gelatin sample is completely melt and kept at constant temperature $T = 37\,°\text{C}$, before the first bulk gelation.

occurs, the particle is trapped in the gel network at a given position. And even if we melt a small droplet, the gelatin network will somehow "remind" this position and pull the particle back to its place when it re-gelifies. Here the drift is very visible because the position of the trapping laser is not the same as the position of the locally heating laser. Thus the position where the particle was during the first bulk gelation is not the position where the particle is attracted to when the gelatin is melted. But even when there is only one laser used for both trapping and heating, this drift can occur. It is indeed impossible to verify that the position where the particle gelifies is exactly the position of the laser, and a drift of only a few nm can be visible.

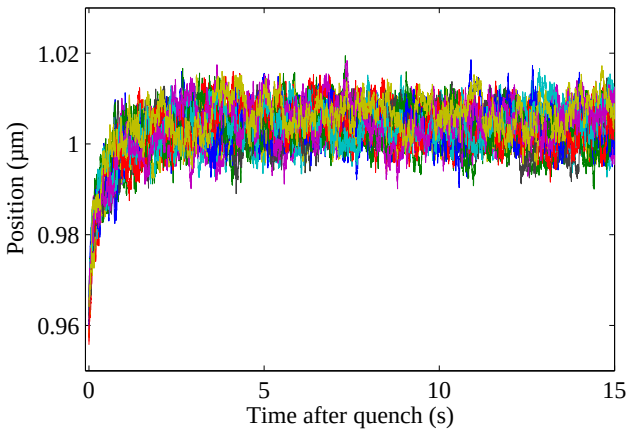

Figure 3.13: 20 first trajectories for a quench at $T_{\text{fb}} = 28\,°\text{C}$, sampled at 400 Hz. A slow drift of $\sim 40\,\text{nm}$ is clearly visible during the first $\sim 1\,\text{s}$. After that, the position only oscillates randomly around a mean value.

We then have three characteristic times :

- τ_{gel} the time needed for the gelatin solution to regelify completely. It goes from a few hundreds to more than 1000 s depending on the quench temperature T_{fb}.
- τ_{dynamics} the typical time of the particle motion, which is directly $\frac{1}{f_c}$ and evolves from ~ 5 to $\sim 100\,\text{s}$ during the gelation process.
- τ_{drift} the time where the drift is visible, which is typically 1 s for our experiment.

If we take a δt sufficiently small compared to τ_{drift}, the boxed and ensemble variances will give more or less the same result. Whereas, since $\tau_{\text{drift}} < \tau_{\text{dynamics}}$, it is clear that the temporal variance will dramatically underestimate the variance due to the lack of low frequencies signal. Indeed, the temporal variance would require a δt of the order of magnitude of τ_{dynamics} for a correct estimation, which cannot be used because of the drift and the ageing. Data are shown on figure 3.14 for $\delta t = 0.1\,\text{s}$.

Now, if the chosen δt is too big compared to the characteristic time of the drift, the boxed variances will start to show an anomalous increase. Data are shown on figure 3.15 for $\delta t = 1\,\text{s}$. This increase is not a real non-equilibrium effect due to the sol-gel transition, but only an artefact due to data analysis in presence of a slow drift. However, this slow drift is due to the fact that the sample is a gelatin solution, where an elastic network is created in the "gel" phase.

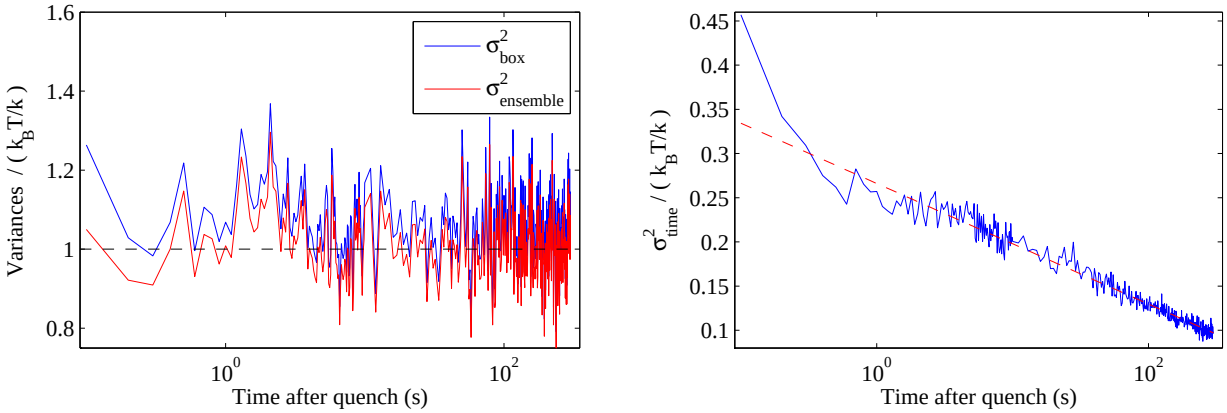

(a) Ensemble and boxed variances.

(b) Temporal variance.

Figure 3.14: Different variances computed for $\delta t = 0.1\,\mathrm{s}$ and normalised by the equilibrium value $k_\mathrm{B}T/k$. The ensemble and boxed values are nearly equal and seem to be close to the equilibrium value at any time after the quench. Whereas the temporal value is clearly below the equilibrium value and decreases logarithmically with time after the quench.

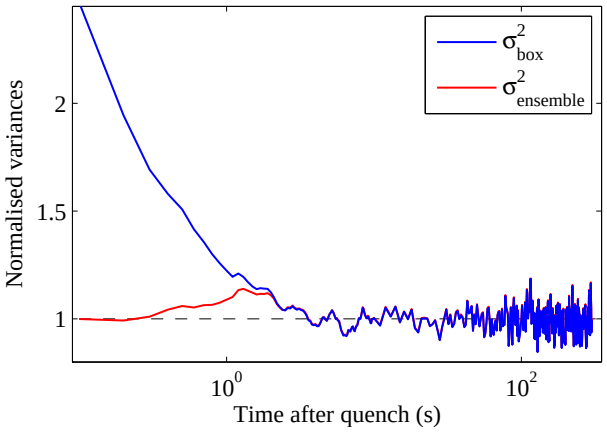

Figure 3.15: Ensemble and boxed variances computed for a $\delta t = 1\,\mathrm{s}$ and normalised by the equilibrium value $k_\mathrm{B}T/k$. The boxed variance clearly shows an anomalous increase at small times after the quench, which is the effect rapported in previous works.

It is nevertheless interesting to see that the correct ensemble variance seems to satisfy the equilibrium equipartition relation at any time after the fast quench, even though there is a clear evolution of the visco-elastic properties with time, and even in the presence of a slow drift at the beginning of the quench:

$$\forall t : \sigma^2_{\mathrm{ensemble}}(t) = \frac{k_\mathrm{B}T}{k}. \tag{3.8}$$

Similar results were seen for different quenches temperatures from 28 °C to 26 °C.

In [64–66] it is stated that for longer times after the quench, the variance should decrease because of the elasticity of the gelatin network (as seen figure 3.1a). This result is not clear. Of course, the dynamics of the particle will be slowed down by the gelation, and in the limit where the sample is completely gelified, the movement of the particle will be arrested. Therefore it is

clear that the temporal variance should go to zero. But there is no reason why the distribution of positions where the particle will stop for different quenches should shrink. It was verified that for τ_{rest} up to 900 s there is no such effect: the correct ensemble variance remains constant. Thus, the fact that the variance decreases for long time in previous works is a sign that the ensemble analysis is mixed with some temporal analysis.

3.3.3 Correct Position Distribution Function estimation

We now want to study not only the variance of the position fluctuations but also their complete Probability Distribution Function (PDF). In order to minimize the risk of slow drifts and to increase the sample frequency, we did new measurements with the second experimental set-up described in 3.2.2. With this set-up, the trapping and heating laser are the same, and the sample frequency can go up to 10 kHz. However, the calibration of the measured deflection from V to µm requires a supplementary assumption (for example, that the Fluctuation-Dissipation Theorem is verified, as it is done in [24]). We will start by doing no assumption and plot the results only in arbitrary units.

One must pay attention at which "position fluctuation" is considered, as people often look at the distribution of $\delta x = x - \langle x \rangle$. The $\langle x \rangle$ is the mean of the position x, which can be defined in several ways when the system is not a classic stationary ergodic system. Especially, when one considers a small time-windows δt, the correct mean should be the ensemble average $\langle x(t) \rangle$ estimated for each time t (as defined in equation 3.6). But if one takes instead the temporal average $\bar{x}_i(t)$, estimated for each trajectory between t and δt (as defined in equation 3.5), the results will differ.

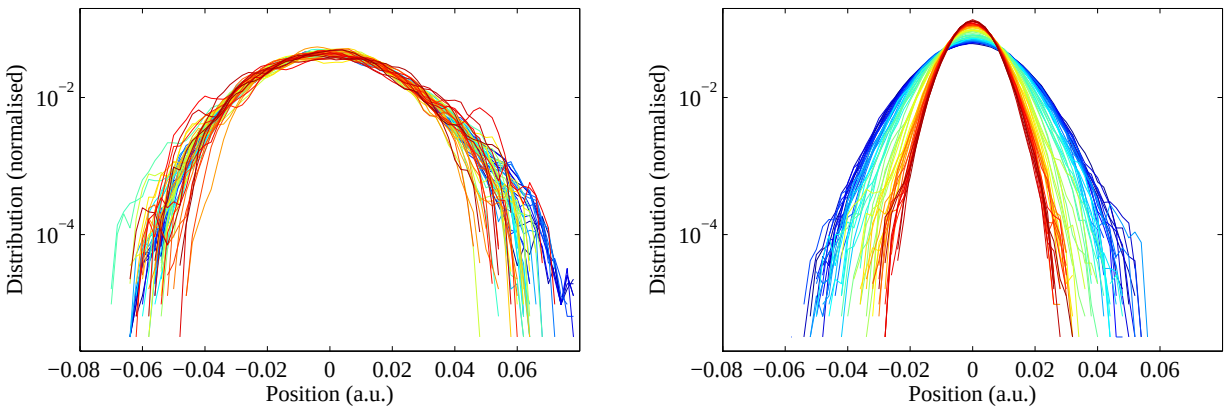

(a) When one subtracts the ensemble average. (b) When one subtracts the temporal average.

Figure 3.16: Evolution of the Probability Distribution Function of the position fluctuation δx depending on the definition taken for the subtracted average. The PDFs are computed on a time-window $\delta t = 0.5$ s for different times after the quench, going from $t = 0$ s (blue curves) to $t = 540$ s (red curves).

As an example, we take the data of 132 quenches at 27.5 °C, sampled at 8 kHz. The parameters are: melting time $\tau_{\text{melt}} = 200$ s, melting intensity $I_{\text{melt}} = 245$ W, resting time $\tau_{\text{rest}} = 570$ s, and trapping intensity $I_{\text{trap=26 W}}$ which corresponds to trap stiffness[5] $k \sim 5$ pN/µm. We com-

[5]The trap stiffness was measured in water (where viscosity is known) for the same laser intensity.

pare the Probability Distribution Function of the positions with a $\delta t = 0.5\,\mathrm{s}$ at different times after the quench, when we subtract either the ensemble average (figure 3.16a) or the temporal average (figure 3.16b). In the first case, the PDFs are nearly always Gaussian and do not evolve in time. In the second case, the PDFs are always nice gaussians, but with a variance that decreases in time. This is consistent with the previous results showing that the ensemble variance is constant at any time after the quench, whereas the temporal variance decreases logarithmically with the time after the quench. And the variances estimated by doing a Gaussian fit on the PDFs clearly shows the same behaviour (see figure 3.17).

This effect is simple to understand: the trajectories evolve on a time τ_{gel}. This time is much bigger than τ_{fluc}, the typical time of the fluctuations, and δt. On the time window δt, each portion of trajectory $x_i(t)$ can be written $x_i(t) = \bar{x}_i + \delta x_i(t)$, where $\bar{x}_i$ is the time average of the i^{th} trajectory over the time-window. When one considers the N trajectory fragments between t and $t+\delta t$, the difference between them is mostly due to the averaged value $\bar{x}_i$ of each trajectory fragment, and not to the fast fluctuations $\delta x_i(t)$. Which means that the distribution of all the $x_i(t)$ between t and $t+\delta t$ is nearly the same as the ensemble distribution of the $\bar{x}_i$. Whereas, the distribution of all the $\delta x_i(t)$ is nothing more than the distribution of the fast temporal fluctuations of one single trajectory.

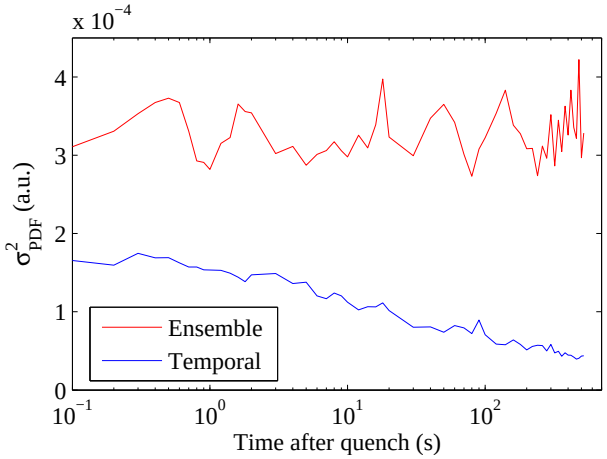

Figure 3.17: Evolution of the variance estimated by fitting the PDFs with a Gaussian, at different times after the fast quench. When subtracting the correct ensemble average the variance is constant. When subtracting the temporal average, the variance decreases almost logarithmically with the time after the quench.

This difference is very important, as any kind of high-pass filtering (for example a "detrend" function which is often used to suppress slow drifts) done to the trajectories will result in subtracting the temporal average, and thus distort the PDFs estimation.

The experimental results show that the correct estimated PDFs do not evolve in time after a fast quench. Since we have already shown that the correct ensemble variance always verifies the equilibrium equipartition relation, we can conclude that the variance of these PDFs is simply $k_{\mathrm{B}}T/k$. It is again interesting to see that, even if the gelatin solution is ageing, its ensemble statistical properties seem to verify relations that are normally verified at equilibrium.

It was also verified with some available data from [64–66] that the correct ensemble PDFs are not evolving with time after the quench.

3.3.4 What about heat and Fluctuation Dissipation Theorem?

In previous works [64–66] the anomalous fluctuations observed right after the quench were interpreted in terms of heat exchanges between the bath and the particle. Indeed, the heat exchanged between t and $t+\tau$ is equal to the variation of the particle's energy $\Delta U_{t,\tau} = \Delta U_{t+\tau} - \Delta U_t$:

$$Q_{t,\tau} = \Delta U_{t,\tau} = \frac{k}{2}\left(x^2(t+\tau) - x^2(t)\right). \tag{3.9}$$

In particular, the fact that the variance was decreasing after the quench was the sign of a heat transfer from the particle to the bath :

$$\langle Q_{t,\tau}\rangle = \frac{k}{2}\left(\sigma^2(t+\tau) - \sigma^2(t)\right) \leq 0. \tag{3.10}$$

The Probability Distribution Functions (PDF) of the $Q_{t,\tau}$ were shown to be asymmetrical for values of t and τ chosen right after the quench (*i.e.* where the anomalous fluctuations were observed).

A violation of Fluctuation-Dissipation Relation was also observed for times right after the fast quench. It was linked to the non-zero heat exchange by a modification of the Harada-Sasa equality [73, 74] for non-stationary systems:

$$\int_{1/\Delta t}^{\infty}\left[S_x(t,f) - \frac{2k_{\mathrm{B}}T}{\pi f}\mathrm{Im}\{\hat{R}(t,f)\}\right]\mathrm{d}f = \frac{2|\langle Q_{t,\Delta t}\rangle|}{k} \tag{3.11}$$

Where $S_x(t,f)$ is the Power Spectral Density of x and $\hat{R}(t,f)$ is the Fourier transform of the linear response function of the position x to a perturbative time-dependent force (these two quantifies are function of the frequency f, but also of the time t since the system is ageing).

All these interpretations comes from the fact that the variance was seen anomalously high right after the quench, and then reduces to the equipartition value after a given time. In particular, the asymmetry and the shape of the PDFs of $Q_{t,\tau}$ are simply mathematical consequences of the fact that $x(t+\tau)$ and $x(t)$ have Gaussian PDFs with different variances $\sigma^2(t+\tau) > \sigma^2(t)$. Since we have already shown that, if estimated correctly, the PDFs of x show no anomalous behaviour and have a constant variance equal to $k_{\mathrm{B}}T/k$, if follows directly that the PDFs of $Q_{t,\tau}$ are symmetrical. Consequently, in average there is no heat exchange between the particle and the bath, for any t and $t+\tau$.

Considering the Fluctuation-Dissipation Theorem, one must remind that it is *a priori* not a good idea to test it in Fourier space. Indeed it is necessary to assume that the system is stationary and ergodic to link the correlation function to the power spectrum with the Wiener–Khinchine theorem [75, 76]. Therefore, when the system is not stationary, one should in theory look at the proper ensemble correlation function:

$$\mathrm{EnsCorr}_{xx}(t,\tau) = \frac{1}{N}\sum_{i=1}^{N}\left[x_i(t) - \langle x(t)\rangle\right] \times \left[x_i(t+\tau) - \langle x(t+\tau)\rangle\right] \tag{3.12}$$

instead of the Power Spectral Density (PSD), which is a temporal quantity. Of course, one can always define a PSD of x_i on a given time-window δt for each trajectory $S_{x_i}(t,f)$. And this PSD would be equal to the Fourier Transform (FT) of the temporal correlation of x_i computed on the same time-window:

$$\mathrm{TimeCorr}_{xx}(t,\tau) = \frac{1}{\delta t}\int_t^{t+\delta t}\left[x_i(t') - \bar{x_i}\right] \times \left[x_i(t'+\tau) - \bar{x_i}\right]\mathrm{d}t' = \mathrm{FT}\{S_{x_i}(t,f)\}. \tag{3.13}$$

But the system needs to be considered stationary and ergodic on the time-window δt, so that the ensemble and temporal correlations should be equal.

Here, the assumption of local stationarity is reasonable since the PSD were computed on 15 s long time windows (which is short compared to the ~ 900 s necessary to gelify). However, it seems probable that the observed violation of Fluctuation-Dissipation Theorem was only due to the same kind of artefact already responsible for anomalous variance increase (for example: slow drifts for times right after the fast quench), because PSDs are sensible to low-frequency noises. Thus, there is no reason that this apparent violation is linked to an heat exchange, which does not exist anyway.

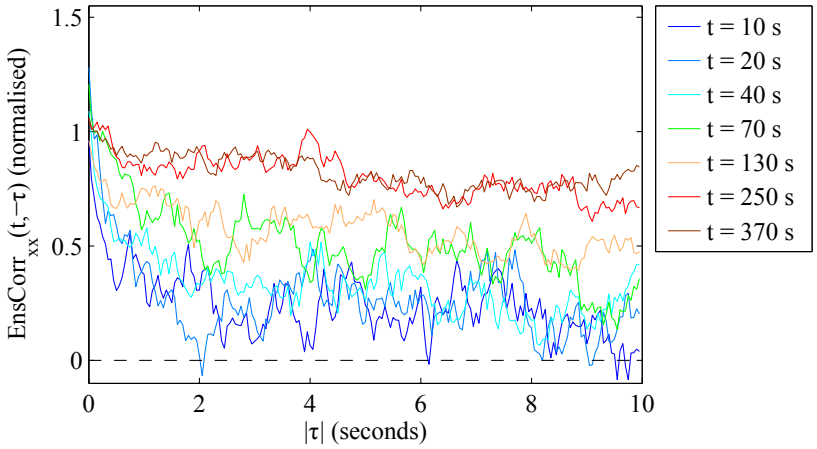

Figure 3.18: Normalised ensemble correlation function for a quench at 27 °C. Here we keep t fixed and we vary τ from -10 s to 0 s. The normalisation is done by dividing $\mathrm{EnsCorr}_{xx}(t,\tau)$ by the value of $k_\mathrm{B}T/k$ extracted from the variance of the position PDFs.

Some ensemble correlation functions of the particle's position are shown in figure 3.18 for a set of 40 quenches at 27 °C, sampled at 8 kHz. The parameters are: melting time $\tau_\mathrm{melt} = 200$ s, melting intensity $I_\mathrm{melt} = 270$ W, resting time $\tau_\mathrm{rest} = 570$ s, and trapping intensity $I_{\mathrm{trap}=26\,\mathrm{W}}$ which corresponds to trap stiffness[6] $k \sim 5$ pN/µm. The data are very noisy, but there is a tendency: the characteristic time increases after the quench, which is reasonable since the gelatin viscosity is also increasing during the gelation. The correlation functions are not simply exponential relaxations, which is consistent with the fact that the PSD are not Lorentzian (as shown in figure 3.9b).

We also made some experimental tests of Fluctuation Dissipation Theorem (FDT), by looking at the ensemble correlation of x and the response to an Heaviside change of the position of the trap. For these measurements, the position of the trap is changed from X_1 to X_2 at a time t_R after the first quench, and the sample is let gelify in X_2. Then, for the second quench, the position of the trap is moved back to X_1 at time t_R after the quench, and the sample is let gelify in X_1. The procedure is then repeated alternatively. The perturbation introduced by the change of trapping position allows us to compute a normalised response function, averaged over the trajectories:

$$\chi(t_R,\tau) = \frac{\langle x(t_R+\tau) - X_\mathrm{initial}\rangle}{X_\mathrm{final} - X_\mathrm{initial}} \tag{3.14}$$

[6]The trap stiffness was measured in water (where viscosity is known) for the same laser intensity.

where $[X_{\text{initial}}; X_{\text{final}}] = [X_1; X_2]$ or $[X_2; X_1]$. It corresponds to the usual definition of the response function:

$$\chi(t) = \frac{\langle x(t)_{\text{perturbed}} - x(t)_{\text{unperturbed}} \rangle}{\text{perturbation amplitude}}. \tag{3.15}$$

We use $X_{\text{final}} - X_{\text{initial}}$ which is proportional to the perturbation amplitude. And we simply take X_{initial} as the average value of the unperturbed trajectory, because the mean position of the bead is constant and equal to the position of the trap if there is no perturbation[7].
If the FDT is verified, the response function should verify:

$$\chi(t_R, \tau) = 1 - \frac{k}{k_{\text{B}}T} \text{EnsCorr}_{xx}(t_R, \tau) \tag{3.16}$$

Some data are presented in figure 3.19 for 50 quenches at 26 °C, sampled at 8 kHz. The parameters are: melting time $\tau_{\text{melt}} = 200\,\text{s}$, melting intensity $I_{\text{melt}} = 270\,\text{W}$, resting time $\tau_{\text{rest}} = 570\,\text{s}$, and trapping intensity $I_{\text{trap=26\,W}}$ which corresponds to trap stiffness[8] $k \sim 5\,\text{pN/µm}$. The values of X_1 and X_2 are estimated by computing the mean position of the bead when the gelatin is melted (which gives alternatively X_1 and X_2). The exact value of $k_{\text{B}}T/k$ was extracted from the variance of the position PDFs computed before changing the position of the trap. These measurements are a bit noisy because it requires a lot of statistics to compute a proper ensemble correlation function, but no apparent violation of the FDT was found for the times tested.

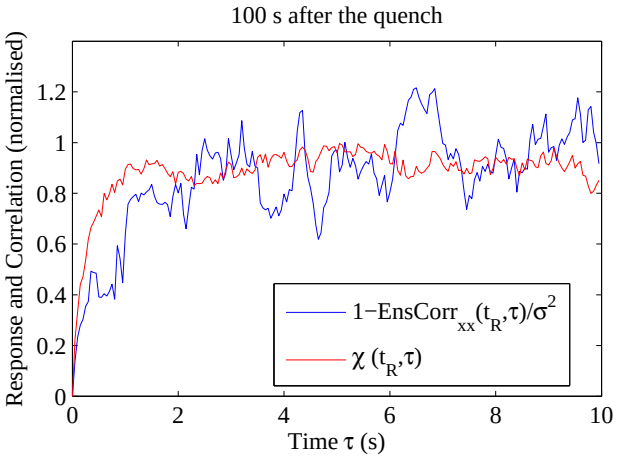

Figure 3.19: Normalised response function $\chi(t_R, \tau)$ and ensemble correlation function for $t_R = 100\,\text{s}$ after the quench, and τ going from 0 to 10 s.

We didn't test the Fluctuation Dissipation Theorem for times t_R taken shortly after the quench, because the ensemble correlation shows a characteristic time which is very short at this time (see figure 3.18). It is then more difficult to compute a proper ensemble correlation right after the quench, than when the viscosity of gelatin has already started to increase. We also didn't compute the response function by varying t_R for a fixed $t_R + \tau$, because it would require a lot of time to do the experiments. Indeed, each set of t_R requires one day of measurement to compute $\chi(t_R, \tau)$, and the sample cannot be kept a lot of days without degrading.

[7] One could also take $\langle x(t_R) \rangle$ to guarantee that $\xi(t_R, 0) = 0$, but it wasn't necessary here.
[8] The trap stiffness was measured in water (where viscosity is known) for the same laser intensity.

3.4 Conclusion and Perspectives

In conclusion, we were unable to reproduce the results of previous works [64–66], but we have identified some experimental and data analysis artefacts which may explain the effects previously observed. We have locally studied the gel transition of gelatin solution, and analysed the effect of time windows on proper ensemble averages, which are important to study ageing systems.

It was shown that in the hysteresis range of temperature ($28.3\,°\mathrm{C} < T < 36\,°\mathrm{C}$), bulk gelation can occur on very long times, and visco-eslatic properties gradually appear. The characteristic time of the particle trapped in the bulk-gelifying sample was seen to decrease exponentially before the gelation (whereas the viscosity evolves logarithmically after the gelation).

For fast quenches of a small droplet of gelatin solution, it was found that the Probability Distribution Functions of the position of the trapped particle do not evolve with time after the quench, even if the gelatin sample is undergoing ageing and the visco-elastic properties are clearly evolving. Moreover, these PDFs show equilibrium-like properties, being Gaussian with a variance equal to the equipartition value $k_\mathrm{B}T/k$. These results seem not so surprising *a posteriori*, since it was already observed in the previous works that, after $\sim 15\,\mathrm{s}$ the Brownian motion of the trapped particle behaves like in equilibrium with the thermal motion of the gelatin chains. Only the very first seconds after the quench showed anomalous behaviour, which was strange, because the complete gelation occurs on much larger scales ($\sim 900\,\mathrm{s}$). In agreement with the absence of anomalous behaviour, no violation of the Fluctuation Dissipation Theorem was seen, as it would be expected in an equilibrium medium.

For systems which are not ergodic or stationary, time properties can be very different from ensemble properties. And it was also shown that some artefacts (like slow drifts) or analysis bias (like high-pass filter) can greatly modify the results if ensemble properties are estimated on time-windows. Therefore, one must be very careful when studying statistical properties of an ageing system. This kind of problems had already arisen for other ageing systems. For example, it was already shown in [77] that increase in effective temperature previously seen in suspension of Laponite [78] were in fact artefacts due to analysis methods.

Finally, since it seems that there is no anomalous variance increase in gelatin after a fast quench, there is no reason to introduce an effective temperature in studying such systems. It follows that this system is not appropriate to study the interactions of two particles trapped at different effective temperatures.

Chapter 4

Effective Temperature by External Random Forcing

Il vaut mieux pomper même s'il ne se passe rien que risquer qu'il se passe quelque chose de pire en ne pompant pas.

Devise Shadok

4.1 Introduction and Motivations

We have convinced ourselves that the sol-gel transition of gelatin solutions is not a good choice to study the effect of two different effective temperatures on trapped beads. Thus we started to look for another system where one can achieve high effective temperatures. A very simple set-up is presented in [79]: by adding an external random force to the trapped sphere, the amplitude of its Brownian fluctuations is increased and the effective kinetic temperature of the particle can reach $\sim 3000\,\mathrm{K}$. In this study, the random forcing is done with random electric fields applied to optically trapped dielectric spheres which electric charges remain constant. We chose to use the same kind of technique, but instead of using an external electric field, the random force is created by modulating the position of one trap. This allows us to have different effective temperatures on different particles, which is not possible with a non-local electric field. The idea is then to trap two particles nearby, and to create an artificial temperature gradient by forcing one of them.

This system is interesting because the energy flux between two micro-systems kept at different temperatures and coupled only by thermal fluctuations plays an important role in out of equilibrium thermodynamics. It has been widely studied theoretically for classical [80–85] and quantum [81, 86–88] systems, but only a few experiments have analysed this problem. For example by measuring the heat flux between two electrical conductors kept in different heat baths and coupled by a capacitor [89], or within a single-electron box consisting of two islands, coupled to separate heat baths, with a tunnel junction [90]. The experimental set-ups are not numerous because of the intrinsic difficulty to produce a large temperature difference on small scales. Moreover, most of the studies consider only systems coupled by conservative forces.

The dissipative coupling is however a very important case because the coupling of two close Brownian particles is dominated by their hydrodynamic interactions in low Reynold-number regimes.

Hydrodynamic interactions between colloidal particles in low Reynold-number fluids have been widely studied starting from the theoretical hydrodynamic calculation [91–94]. Several recent experimental set-ups, made possible by tools like holographic optical tweezers [16, 17], have shown that these indirect interactions mediated by the solvent play an important role in various physical situations. For example, they modify the Brownian diffusion of two nearby particles [95, 96]. The displacement cross-correlations between two trapped particles also show an anti-correlation at finite time, which has been studied both experimentally and numerically [97–100]. Systems with arrays of more than two trapped particles coupled by hydrodynamic interactions show complex dynamics [101–103] and can behave as an elastic medium [104]. The hydrodynamic coupling is also responsible for the synchronisation of colloidal oscillators which can be linked to collective motions of biological systems like cilia or flagella [105–108], and for the pair-attractions of particles driven on a circular ring [109, 110].

In this chapter, we use an analytical model based on classical hydrodynamic coupling tensor to study how the equilibrium statistical properties of two coupled trapped particles are modified when one particle is randomly forced. The connection to stochastic thermodynamics is done by assimilating the random forcing to a "kinetic effective temperature" [79, 111]. We are then able to identify stochastic heat exchanges between the two particles kept at different effective temperatures, and to compare our experimental data to the model's predictions. The results described in this chapter were partially presented in the publication [112].

4.2 Experimental set-up

4.2.1 Trapping two particles

The experimental set-up requires two independent traps, with the ability to modulate the position of at least one of them. We use another configuration of our optical tweezers set-up: a laser beam (wavelength 532 nm) is separated in two beams with crossed polarisations so that there is no interference between them. A custom-built vertical optical tweezers with an oil-immersion objective (HCX PL. APO 63×/0.6-1.4) is used to focus both beams. Thus each of them creates a quadratic potential well where a silica bead (radius $R = 1\,\mu\text{m} \pm 5\%$) is trapped. One of the beams goes through an acousto-optic deflector (AOD) that allows to switch the position of the trap very rapidly (up to 1 MHz). See figure 4.1.

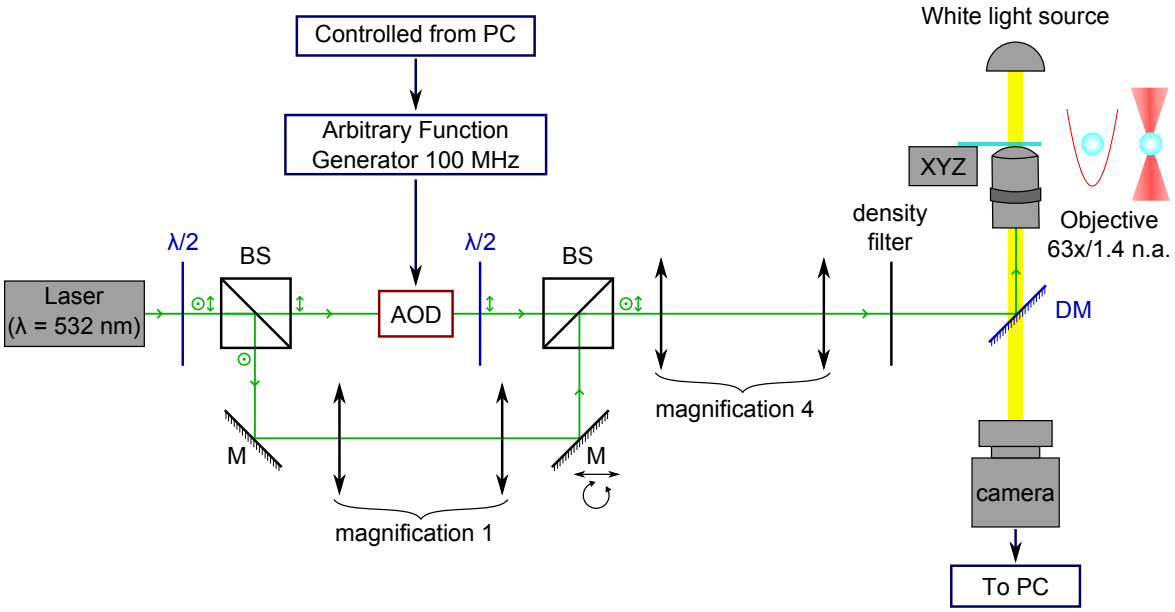

Figure 4.1: Schematic representation of optical tweezers set-up used to trap two particles nearby in crossed polarised double well potentials. The Acousto-Optic Deflector (AOD) is used to modulate rapidly the position of one of the two traps. "M" are mirrors and "DM" is a dichroic mirror.

The beads are dispersed in bidistilled water at low concentration to avoid interactions with multiple other beads. The beads solution is contained in a disk-shaped cell (18 mm in diameter, 1 mm in depth), already described in section 1.1.2. The beads are trapped at $h = 15\,\mu\text{m}$ above the bottom surface of the cell. The positions of the beads are tracked by a fast camera with a resolution of 119 nm per pixel, which after treatment gives the position with an accuracy better than 5 nm. The camera's speed can go up to 1600 frame/s for small image sizes but the trajectories are usually sampled at 800 Hz. The stiffness of the traps k is proportional to the laser intensity and is typically $4\,\text{pN}/\mu\text{m}$. It can be modified by turning an half-wave plate placed before the polarization separation or by adding neutral density filters on the beams trajectory. The two particles are trapped on a line (called "x axis") and separated by a distance d which is tunable. For all the distances used (between 2.8 and 6 µm) the Coulombian interaction between

the particle surfaces is negligible. Thus they only interact through the surrounding fluid. A schematic representation of the two trapped particles is shown in figure 4.2.

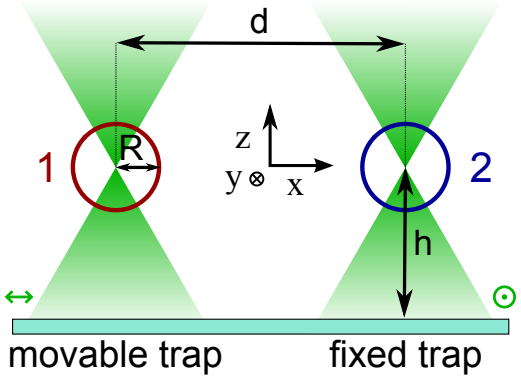

Figure 4.2: Schematic representation of the two trapped particles separated by a distance d along x axis. The particle are immersed in bidistilled water. The camera (not represented here) records the displacements of the beads in directions x and y, at a rate of 800 Hz.

The stiffness of one trap at equilibrium can be measured by calculating the variance of the x-displacement of the bead σ_x^2 or by fitting the Power Spectral Density (PSD) of the x-displacement. Indeed, because of the energy equipartition theorem we expect:

$$\sigma_x^2 = \frac{k_B T}{k} \tag{4.1}$$

where k_B is the Boltzmann constant and T the temperature. Because the particles are overdamped, the PSD is Lorentzian:

$$S_x(f) = \frac{4\gamma k_B T/k^2}{1 + f^2/f_c^2}. \tag{4.2}$$

with the cut-off frequency f_c that verifies $f_c = k/(2\pi\gamma)$ where $\gamma = 6\pi R\eta$ and η is the dynamic viscosity of water. The two methods give compatible results, assuming that the viscosity of water and then Faxén corrections, due to the finite distance h between the particle and the bottom of the cell, are known. Nevertheless, big distances d can only be achieved experimentally by moving the laser beam away from the center of the microscope objective. It was observed that when the beam is not well centred, the shape of the potential is always a bit impaired, which gives a lower value of k as well as some noise at low frequency in the bead's displacement. Hence, we prefer to estimate the stiffness values from the PSD, where we can easily see low frequency noise which may alter the measured value of σ_x^2.

4.2.2 Effective temperature on one particle

To add an external force on one of the particles, we modulate the position of the corresponding trap (here we call 1 the particle in the movable trap, and 2 the particle in the fixed trap nearby). The force exerted by the trap is : $-k(x - x_0)$, where x_0 is the position of the trap, and x the particle's position. Then, an instantaneous trap displacement of δx_0 will create an instantaneous force equal to $k\delta x_0$, given that the displacement is small enough to remain in the linear regime.

To create an effective temperature we need an external force with the same statistical properties as the thermal noise. Thus we send a numerically generated Gaussian white noise to the AOD so that the position of the corresponding trap is moved randomly in the x direction. The noise is created by a Labview® program and is sampled at 100 kHz with a tunable amplitude A (typically of $\sim 1\,\mathrm{V}$). It is generated by the analog output of a *NI PXIe-6366* card. The conversion factor for the displacement due to the AOD is 2.8 µm/V. We have experimentally observed that directly using this noise results in a change of stiffness rather than an effective temperature. We believe this effect is due to the fact that the position of the trap is moved too fast with respect to the typical relaxation time of the trapped particle[1]. Thus we added a numerical low-pass filter at 1 kHz to the generated noise. The typical voltage of the noise after filtration is between $\pm 0.25\,\mathrm{V}$. Then, when the random force is switched on, the bead quickly reaches a stationary state with an "effective temperature" for the randomly forced degree of freedom.

The Power Spectral Densities of one bead's displacement in the x-direction with different noise amplitude (between 0 and 1.8 V) are shown in figure 4.3. The displacement in the y-direction is not modified by the added noise.

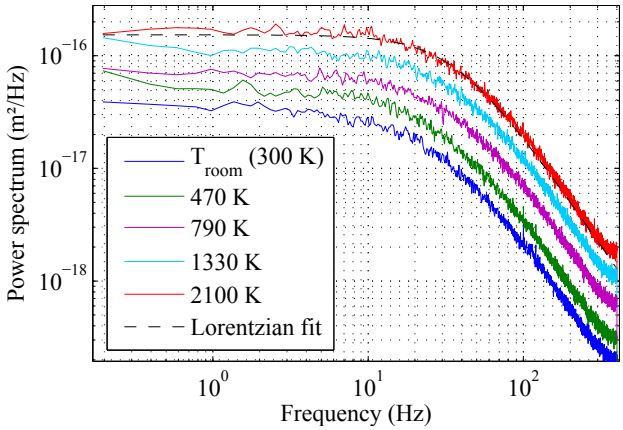

Figure 4.3: Power Spectral Densities of the x-displacement of one bead of radius $R = 1\,\mu\mathrm{m}$ trapped with stiffness $k = 3.4\,\mathrm{pN/\mu m}$ in water at room temperature, at equilibrium (lowest blue curve), and for noise amplitude A from 0.6 to 1.8 V (A is incremented of 0.4 V between each curve). The black dashed line is a Lorentzian fit of the spectrum with $A = 1.8\,\mathrm{V}$. The indicated effective temperatures are calculated from the variances, assuming that the equipartition theorem remains valid.

As in [79], the PSDs when the bead is randomly forced are just vertical translations of the equilibrium ones. The PSDs remain Lorentzian, and the cut-off frequency $f_c = k/(2\pi\gamma)$ obtained by fitting them is not modified by more than a few hertz when the amplitude of the forcing is lower than 1.5 V. Since the viscosity term γ is not modified by the forcing, it means that the stiffness k of the trap is let unchanged by the random force. Then, only a change of effective temperature can explain the observed PSDs (see equation 4.2).

For forcing amplitudes higher than 1.5 V, f_c starts to be modified and the spectrum starts to be slightly less accurate at high frequency. This happens because the forced random dis-

[1] The typical cut-off frequency f_c is 30 Hz.

placement of the trap is too big compared to the size of the harmonic interval of the trapping potential. However, with an amplitude of 1.5 V, the effective temperature is already 1500 K, which gives us a wide range to work with.

Finally, our set-up allows us to trap two particles nearby and to add a random force with chosen properties to one of them.

4.3 Hydrodynamic coupling model

We use a classical hydrodynamic coupling model to describe the system of the two interacting trapped particles.

4.3.1 Coupled Langevin equations

In low Reynolds-number flow, the motion of two particles free to rotate (with no external torque) can be described by the following equations [97, 113]:

$$\frac{\mathrm{d}\vec{r_i}}{\mathrm{d}t} = \sum_{j=1}^{2} \mathbf{H}_{ij}\, \vec{F_j} \tag{4.3}$$

where $\vec{r_i}$ is the position of the particle i, $\mathbf{H}_{ij}$ is the hydrodynamic coupling tensor (also often called the mobility matrix) which depends on $(\vec{r_i} - \vec{r_j})$, and $\vec{F_i}$ is the force acting on the particle i.

Following [97–99], if we consider only the longitudinal motion of two thermally excited trapped particles (as shown in figure 4.2), we can use the two coupled Langevin equations:

$$\begin{pmatrix} \dot{x}_1 \\ \dot{x}_2 \end{pmatrix} = \mathcal{H} \times \begin{pmatrix} F_1 \\ F_2 \end{pmatrix} \tag{4.4}$$

where x_i is the position of the particle i relative to its trapping position (the particles are trapped along the x-axis), and $\dot{x}_i$ is the time derivative of x_i.
At equilibrium the forces acting on the particles are:

$$F_i = -k_i \times x_i + f_i \tag{4.5}$$

where k_i is the stiffness of the trap i and f_i are the Brownian random forces which verify:

$$\begin{array}{rcl} \langle f_i(t) \rangle & = & 0 \\ \langle f_i(t) f_j(t') \rangle & = & 2k_\mathrm{B}T\, (\mathcal{H}^{-1})_{ij}\, \delta(t-t') \end{array} \tag{4.6}$$

where k_B is the Boltzmann constant and T the temperature of the surrounding fluid.
For two identical particles of radius R trapped at positions separated by a distance d, assuming that their displacements are small compared to the mean distance between them, the hydrodynamic coupling tensor reads:

$$\mathcal{H} = \begin{pmatrix} 1/\gamma & \epsilon/\gamma \\ \epsilon/\gamma & 1/\gamma \end{pmatrix} \tag{4.7}$$

where γ is the Stokes friction coefficient ($\gamma = 6\pi R\eta$ where η is the viscosity of water) and ϵ is the coupling coefficient ($\epsilon = \frac{3R}{2d}$ if one takes the first order of the Oseen tensor [113], $\epsilon = \frac{3R}{2d} - \left(\frac{R}{d}\right)^3$ if one takes the Rotne-Prager diffusion tensor [103]).

To describe the effective temperature, we simply add an external random force f^* on the first particle. This force is completely decorrelated with the Brownian random forces and characterised by an additional effective temperature ΔT (the particle 1 is then at an effective temperature $T^* = T + \Delta T$):

$$\begin{array}{rcl} \langle f^*(t) \rangle & = & 0 \\ \langle f^*(t) f_i(t') \rangle & = & 0 \\ \langle f^*(t) f^*(t') \rangle & = & 2k_\mathrm{B}\Delta T\gamma\delta(t-t') \end{array} \tag{4.8}$$

It follows that our system of equations is:

$$\begin{cases} \gamma\dot{x}_1 = -k_1x_1 + \epsilon(-k_2x_2 + f_2) + f_1 + f^* \\ \gamma\dot{x}_2 = -k_2x_2 + \epsilon(-k_1x_1 + f_1 + f^*) + f_2 \end{cases} \tag{4.9}$$

It can be rewritten:

$$\begin{cases} \dot{x}_1 = g_1(x_1, x_2) + \xi_1 \\ \dot{x}_2 = g_2(x_1, x_2) + \xi_2 \end{cases} \tag{4.10}$$

with:

$$g_i(x_i, x_j) = -\frac{1}{\gamma}k_ix_i - \frac{\epsilon}{\gamma}k_jx_j \tag{4.11}$$

and:

$$\begin{array}{rcl} \xi_1 & = & \frac{1}{\gamma}(f_1 + \epsilon f_2 + f^*) \\ \xi_2 & = & \frac{1}{\gamma}(f_2 + \epsilon f_1 + \epsilon f^*) \end{array} \tag{4.12}$$

which are the equivalent Brownian random forces (normalised by γ).

4.3.2 Variances and cross-variances

The system is stationary[2], and the first quantities we can easily compute are the variances and cross-variance:

$$\begin{aligned} \sigma_{11}^2 &= \langle x_1x_1 \rangle \\ \sigma_{22}^2 &= \langle x_2x_2 \rangle \\ \sigma_{12}^2 &= \langle x_1x_2 \rangle = \sigma_{21}^2. \end{aligned} \tag{4.13}$$

The equations 4.10 are close to those describing the energy exchanged between two heat baths coupled by thermal fluctuations [89] and it can be proved that the time evolution of the joint Probability Distribution Function (PDF) $P(x_1, x_2, t)$ is governed by the Fokker-Planck equation [114]:

$$\frac{\partial P}{\partial t} = -\frac{\partial(g_1P)}{\partial x_1} - \frac{\partial(g_2P)}{\partial x_2} + 2\theta_{12}\frac{\partial^2 P}{\partial x_1 \partial x_2} + \theta_{11}\frac{\partial^2 P}{\partial x_1^2} + \theta_{22}\frac{\partial^2 P}{\partial x_2^2} \tag{4.14}$$

where θ_{ij} is defined by:

$$\langle \xi_i(t)\xi_j(t') \rangle = 2\theta_{ij}\delta(t - t'). \tag{4.15}$$

Here we have:

$$\begin{aligned} \theta_{11} &= k_{\mathrm{B}}(T + \Delta T)/\gamma \\ \theta_{12} &= k_{\mathrm{B}}\epsilon(T + \Delta T)/\gamma \\ \theta_{22} &= k_{\mathrm{B}}(T + \epsilon^2\Delta T)/\gamma. \end{aligned} \tag{4.16}$$

The stationary solution of equation 4.14 can be written:

$$P_s(x_1, x_2) = \frac{\sqrt{ac - b^2}}{\pi}\mathrm{e}^{-(ax_1^2 + 2bx_1x_2 + cx_2^2)} \tag{4.17}$$

[2]We did not look at the transient regime when the random force is added or when it's amplitude is changed.

where:

$$\begin{aligned} a &= \frac{k_1(k_1+k_2)\left((k_1+k_2)T+\epsilon^2 k_2\Delta T\right)}{\Theta} \\ b &= \frac{-\epsilon k_1 k_2(k_1+k_2)\Delta T}{\Theta} \\ c &= \frac{k_2(k_1+k_2)\left((k_1+k_2)T+(k_1+k_2(1-\epsilon^2))\Delta T\right)}{\Theta} \end{aligned} \tag{4.18}$$

with:

$$\Theta = 2k_\mathrm{B}\left((T^2+T\Delta T)(k_1+k_2)^2-\epsilon^2(\epsilon^2-1)k_2^2\Delta T^2)\right). \tag{4.19}$$

Then, one can compute the variances of each position and the cross-variance between the two particles:

$$\sigma_{ij}^2 = \iint_{-\infty}^{+\infty} x_i x_j P_s(x_1,x_2)\,\mathrm{d}x_1\mathrm{d}x_2 \tag{4.20}$$

We find:

$$\begin{aligned} \sigma_{11}^2 &= \frac{k_\mathrm{B}(T+\Delta T)}{k_1} - \frac{k_2}{k_1}\frac{\epsilon^2 k_\mathrm{B}\Delta T}{k_1+k_2} \\ \sigma_{12}^2 &= \frac{\epsilon k_\mathrm{B}\Delta T}{k_1+k_2} \\ \sigma_{22}^2 &= \frac{k_\mathrm{B}T}{k_2} + \frac{\epsilon^2 k_\mathrm{B}\Delta T}{k_1+k_2} \end{aligned} \tag{4.21}$$

This result shows several expected behaviours, like the increase of σ_{11}^2 due to the random forcing, or the increase of σ_{22}^2 due to the coupling between the two particles. But it also shows the appearance of a non-zero cross-variance σ_{12}^2 which does not exist in the equilibrium case (when $\Delta T = 0$). The random forcing done on only one particle induces an instantaneous cross-correlation of the particle's x-displacements. One can also identify an energy exchange between the two particles. Indeed the variances can be rewritten:

$$\begin{aligned} \sigma_{11}^2 &= \sigma_{1\,\mathrm{n.c.}}^2 - \frac{k_2}{k_1}\frac{\epsilon^2 k_\mathrm{B}\Delta T}{k_1+k_2} \\ \sigma_{22}^2 &= \sigma_{2\,\mathrm{n.c.}}^2 + \frac{\epsilon^2 k_\mathrm{B}\Delta T}{k_1+k_2} \end{aligned}$$

where $\sigma_{i\,\mathrm{n.c.}}^2$ is the variance of the particle i with no coupling, *i.e.* the variance that the particle i would have if it was alone (*i.e.* $\epsilon = 0$).
It follows that the variance of the "hot" particle (the forced one) is decreased by the presence of the "cold" particle, and reciprocally the variance of the cold one is increased by the presence of the hot one.

This behaviour is well verified experimentally and presented in figure 4.4. For a fixed distance d (figure 4.4a), when the first bead is forced we observe that the variance of its x-displacement σ_{11}^2 and the variance of the second particle's displacement σ_{22}^2 increase. The cross-variance σ_{12}^2 also ceases to be zero and increases with the amplitude of the random noise. For a fixed noise amplitude A (figure 4.4b), the values of σ_{22}^2 and σ_{12}^2 slightly decrease with the distance d between the particles, which is normal since ϵ decreases when d is increased.

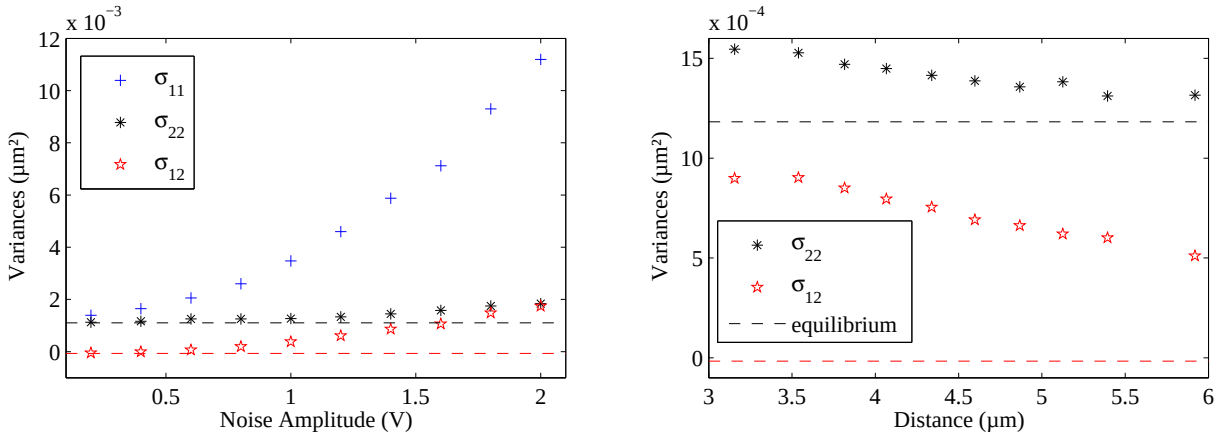

(a) (b)

Figure 4.4: Variance of the displacement of each bead (σ_{22}^2 and σ_{11}^2) and cross-variance between the two displacement (σ_{12}^2). (a) When the random forcing amplitude A is increased on the first bead and the distance between the traps is kept constant, $d = 3.2\,\mu\text{m}$, the variances and the cross-variance increase. The dashed-lines are the values of σ_{22}^2 and σ_{12}^2 measured when there is no random forcing. (b) Zoom on σ_{22}^2 and σ_{12}^2 for a fixed forcing amplitude $A = 1.5\,\text{V}$, both values decrease with d the mean distance between the two particles (σ_{11}^2 which is not shown remains nearly constant and equal to $5.7 \times 10^{-3}\,\mu\text{m}^2$). The dashed-lines are the values of σ_{22}^2 and σ_{12}^2 averaged over d when there is no random forcing.

To be more quantitative, one can measure σ_{11}^2,σ_{12}^2 and σ_{22}^2, and solve the system 4.21 to find the values of T, ΔT and ϵ (given that k_1 and k_2 are measured separately). One finds:

$$\begin{aligned} T &= \frac{k_1\sigma_{11}^2 + 3k_2\sigma_{22}^2 - \Upsilon}{4k_\text{B}} \\ \Delta T &= \frac{k_1\sigma_{11}^2 - k_2\sigma_{22}^2 + \Upsilon}{2k_\text{B}} \\ \epsilon &= \frac{-k_1\sigma_{11}^2 + k_2\sigma_{22}^2 + \Upsilon}{4k_2\sigma_{12}^2} \end{aligned} \tag{4.22}$$

with:

$$\Upsilon = \sqrt{8k_2(k_1+k_2)\sigma_{12}^4 + (k_1\sigma_{11}^2 - k_2\sigma_{22}^2)^2}. \tag{4.23}$$

Some experimental values for a given distance d and different amplitudes of forcing A applied on particle 1 are shown in figure 4.5. Values for a given forcing amplitude and different distances are shown in figure 4.6. For these data, the values of σ_{12}^2 used for computation are corrected by subtracting the value of the cross-variance when the system is at equilibrium (this value should theoretically be zero and gives an estimation of the incertitude on σ_{12}^2). As expected:

- T is always nearly constant and equal to room temperature (all values are compatible with room temperature of 297 K with a precision of 10%)
- ϵ depends only on the distance between the particles (in figure 4.5b all values are between 0.37 and 0.42)
- ΔT depends only on the forcing amplitude applied on the first particle.

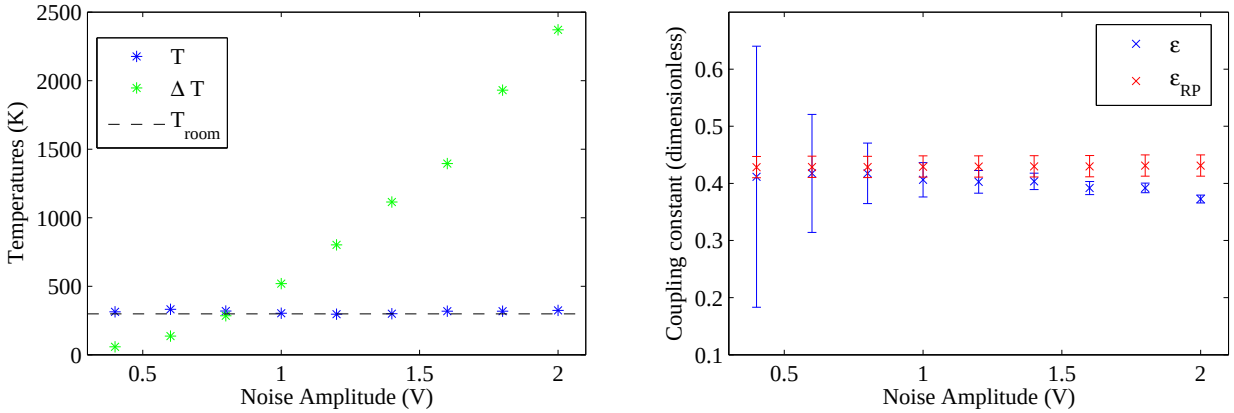

(a) (b)

Figure 4.5: Coupling coefficient (ϵ), temperature of the bath (T) and effective temperature (ΔT), measured from the values of σ^2_{11},σ^2_{12} and σ^2_{22}, for two particles trapped at distance $d = 3.2\,\mu\text{m}$ as a function of the amplitude A of the forcing done on one particle. The theoretical coupling coefficient from the Rotne-Prager diffusion tensor (ϵ_{RP}) is computed for particles of radius $R = 1\,\mu\text{m} \pm 5\%$.

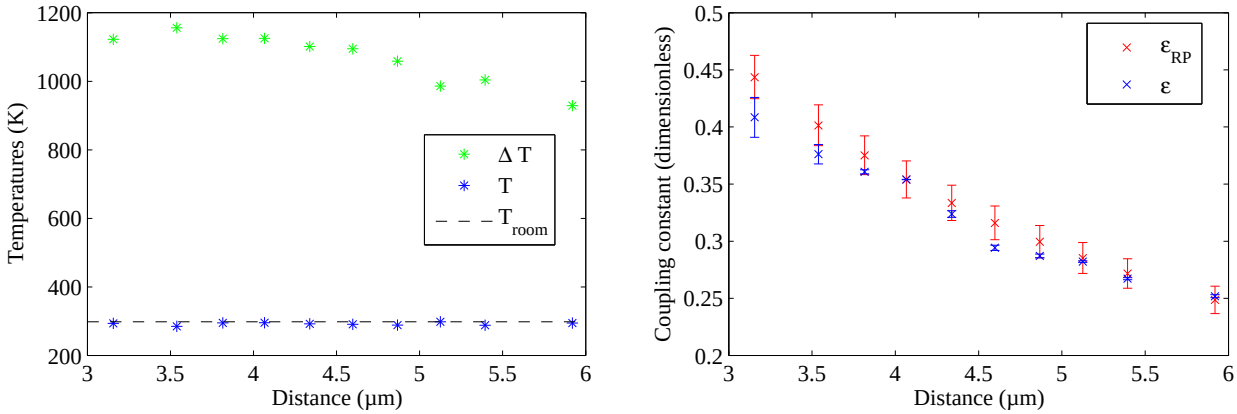

(a) (b)

Figure 4.6: Coupling coefficient (ϵ), temperature of the bath (T) and effective temperature (ΔT), measured from the values of σ^2_{11},σ^2_{12} and σ^2_{22}, for two particles at different effective temperature as a function of the distance d between the particles. The theoretical coupling coefficient from the Rotne-Prager diffusion tensor (ϵ_{RP}) is computed for particles of radius $R = 1\,\mu\text{m} \pm 5\%$.

In figures 4.5b and 4.6b we notice that the measured value of ϵ is always slightly lower than the theoretical one (estimated by the Rotne-Prager diffusion tensor). However it also shows the expected dependence in the distance d between the two particles ($\epsilon \propto 1/d$). We do not have a definitive explanation for this discrepancy, but we have verified that it is not due to the finite distance to the bottom surface h by changing it to $10\,\mu\text{m}$ or $20\,\mu\text{m}$ without observing significant change of ϵ. It might simply be a problem of calibration in the trap stiffnesses, or in the particles radius R from the manufacturer. There also are at least two experimental problems with the estimation of ϵ: for very low forcing (i.e. low ΔT), the errorbars are big because they

are estimated considering that the main source of incertitude is the value of σ_{12}^2, which is very low when forcing is low. When the forcing is very high, the estimation of ϵ starts to be less precise because, as already mentioned, the added random force begins to be less accurate for high displacements of the trap position. This effect is also noticeable in figure 4.5a, where one can see that ΔT is not perfectly linear in A. In figure 4.6a the effective temperature ΔT is not perfectly constant but slightly decreases when the distance d is increased. This effect is due to the less accurate response of the AOD far from the center of the apparatus: the shape of the trap is always altered when the beam is not well centred, which lowers the stiffness of the trap and consequently the ΔT corresponding to a given noise amplitude[3].

4.3.3 Position cross-correlations

The position cross-correlation functions were first measured for two trapped particles interacting in a thermal bath at equilibrium in [97]. If the two stiffnesses are equal $k_1 = k_2 = k$, the cross-correlations verify:

$$\langle x_1(t)x_2(0)\rangle = \langle x_1(0)x_2(t)\rangle = \frac{k_\mathrm{B}T}{2k}\left[\mathrm{e}^{-k(1+\epsilon)t/\gamma} - \mathrm{e}^{-k(1-\epsilon)t/\gamma}\right]. \tag{4.24}$$

Nota Bene: the usual cross-correlation is $\langle (x_1 - \langle x_1\rangle)(x_2 - \langle x_2\rangle)\rangle$ but here we have $\langle x_1\rangle = 0$ and $\langle x_2\rangle = 0$ because the average position of the particle i is the position of its trap.
The shape of the curve is plotted in figure 4.7, for stiffness $k = 3.5\,\mathrm{pN/\mu m}$, particle radius $R = 1\,\mu\mathrm{m}$, viscosity $\eta = 9.67\,\mathrm{Pa\cdot s}$ (which is the viscosity of water at 23 °C, with the Faxén corrections for a distance to the bottom surface $h = 15\,\mu\mathrm{m}$) and distance between the beads $d = 4\,\mu\mathrm{m}$. The cross-correlation function is zero at $t = 0$, and shows an anti-correlation with a maximum at a finite time $t_{\min} = (\gamma/2k\epsilon)\ln\left((1+\epsilon)/(1-\epsilon)\right) \approx (\gamma/k)$.

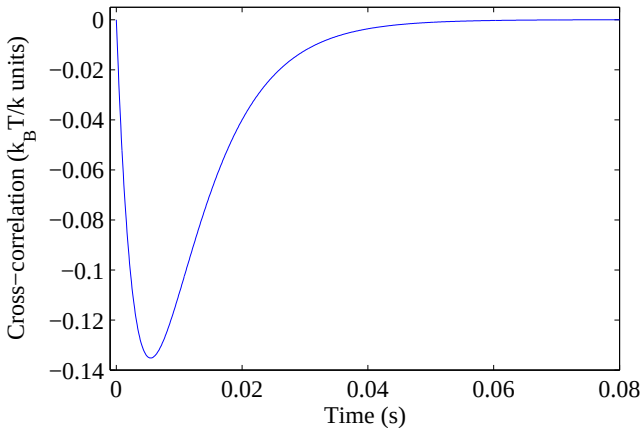

Figure 4.7: Theoretical position cross-correlation function $\langle x_1(t)x_2(0)\rangle$, for parameters close to the experimental ones.

Since the system is stationary, we have $\langle x_1(-t)x_2(0)\rangle = \langle x_1(0)x_2(t)\rangle$. Then we can experimentally compute only $\langle x_1(0)x_2(t)\rangle$ for positive and negative times to have access to both $\langle x_1(0)x_2(t)\rangle$ and $\langle x_1(t)x_2(0)\rangle$. Some cross-correlation functions with no random force are shown

[3] ΔT should be proportional to A and k_1.

in figure 4.8. The agreement with the theoretical formula is not perfect, in particular we do not have exactly $\langle x_1(0)x_2(0)\rangle = 0$ for small distances d between the beads. But the functions are quite symmetrical, which is normal because the two beads play the same role, and the global shape is corresponding to the expected one.

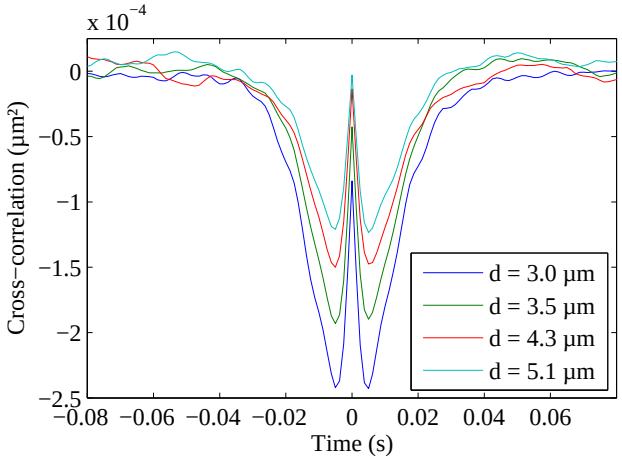

Figure 4.8: Experimental position cross-correlation functions $\langle x_1(0)x_2(t)\rangle$, for two particles trapped at different distances d, in a thermal bath at equilibrium at room temperature.

To compute the cross-correlation functions in the case where the random forcing is done on particle 1, we can use the method described in [99]. We compute the Laplace transform of equations 4.9:

$$\begin{aligned}\gamma(\hat{x}_1(s) - x_1(0)) &= -k_1\hat{x}_1(s) - \epsilon k_2\hat{x}_2(s) + \gamma\hat{\xi}_1(s)\\ \gamma(\hat{x}_2(s) - x_2(0)) &= -k_2\hat{x}_2(s) - \epsilon k_1\hat{x}_1(s) + \gamma\hat{\xi}_2(s)\end{aligned} \tag{4.25}$$

where $\hat{x}(s) = \int_0^\infty x(t)\mathrm{e}^{-st}\,\mathrm{d}t$. If we multiply the equations 4.25 by $x_2(0)$ and compute the ensemble average, we get a system of equations with the cross-correlation $\langle\hat{x}_1(s)x_2(0)\rangle$ and the auto-correlation of the second particle $\langle\hat{x}_2(s)x_2(0)\rangle$:

$$\begin{aligned}\gamma\left(\langle\hat{x}_1(s)x_2(0)\rangle - \sigma_{12}^2\right) &= -k_1\langle\hat{x}_1(s)x_2(0)\rangle - \epsilon k_2\langle\hat{x}_2(s)x_2(0)\rangle\\ \gamma\left(\langle\hat{x}_2(s)x_2(0)\rangle - \sigma_{22}^2\right) &= -k_2\langle\hat{x}_2(s)x_2(0)\rangle - \epsilon k_1\langle\hat{x}_1(s)x_2(0)\rangle\end{aligned} \tag{4.26}$$

If we multiply the equations 4.25 by $x_1(0)$ and compute the ensemble average, we get a system of equations with the cross-correlation $\langle\hat{x}_2(s)x_1(0)\rangle$ and the auto-correlation of the first particle $\langle\hat{x}_1(s)x_1(0)\rangle$.

$$\begin{aligned}\gamma\left(\langle\hat{x}_1(s)x_1(0)\rangle - \sigma_{11}^2\right) &= -k_1\langle\hat{x}_1(s)x_1(0)\rangle - \epsilon k_2\langle\hat{x}_2(s)x_1(0)\rangle\\ \gamma\left(\langle\hat{x}_2(s)x_1(0)\rangle - \sigma_{21}^2\right) &= -k_2\langle\hat{x}_2(s)x_1(0)\rangle - \epsilon k_1\langle\hat{x}_1(s)x_1(0)\rangle\end{aligned} \tag{4.27}$$

We were interested by the cross-correlation functions[4] so we solved the two systems, using equations 4.21, and we get:

$$\begin{aligned}\langle\hat{x}_1(s)x_2(0)\rangle &= \frac{k_\mathrm{B}\gamma\epsilon\left[(k_1+k_2)T + \Delta T(k_2(\epsilon^2-1) - s\gamma)\right]}{(k_1+k_2)(k_1k_2\epsilon^2 - (k_1+s\gamma)(k_2+s\gamma))}\\ \langle\hat{x}_2(s)x_1(0)\rangle &= \frac{k_\mathrm{B}\gamma\epsilon\left[(k_1+k_2)T + \Delta T(k_2(1-\epsilon^2) - s\gamma)\right]}{(k_1+k_2)(k_1k_2\epsilon^2 - (k_1+s\gamma)(k_2+s\gamma))}\end{aligned}$$

[4]The auto-correlation functions can easily be computed following the same method.

Then, by taking the inverse Laplace Transform:

$$\langle x_1(t)x_2(0)\rangle = \frac{\epsilon k_\mathrm{B}}{2(k_1+k_2)\kappa}\Big[\Big(\Delta T(\kappa+k_1+k_2(2\epsilon^2-1))+2T(k_1+k_2)\Big)\,\mathrm{e}^{-(k_1+k_2-\kappa)t/2\gamma} + \Big(\Delta T(\kappa-k_1-k_2(2\epsilon^2-1))-2T(k_1+k_2)\Big)\,\mathrm{e}^{-(k_1+k_2+\kappa)t/2\gamma}\Big] \quad (4.28)$$

$$\langle x_1(0)x_2(t)\rangle = \frac{\epsilon k_\mathrm{B}}{2(k_1+k_2)\kappa}\Big[\Big(\Delta T(\kappa+k_1+k_2(3-2\epsilon^2))+2T(k_1+k_2)\Big)\,\mathrm{e}^{-(k_1+k_2-\kappa)t/2\gamma} + \Big(\Delta T(\kappa-k_1-k_2(3-2\epsilon^2))-2T(k_1+k_2)\Big)\,\mathrm{e}^{-(k_1+k_2+\kappa)t/2\gamma}\Big] \quad (4.29)$$

with :

$$\kappa = \sqrt{k_1^2-2k_1k_2+k_2^2+4\epsilon^2k_1k_2}. \quad (4.30)$$

Finally, we can simplify these equations by considering that $k_1 = k_2 = k$, and we get:

$$\langle x_1(t)x_2(0)\rangle = \frac{k_\mathrm{B}}{4k}\Big[(-2T+\Delta T\epsilon(1-\epsilon))\,\mathrm{e}^{-k(1-\epsilon)t/\gamma}+(2T+\Delta T\epsilon(1+\epsilon))\,\mathrm{e}^{-k(1+\epsilon)t/\gamma}\Big] \quad (4.31)$$

$$\langle x_1(0)x_2(t)\rangle = \frac{k_\mathrm{B}}{4k}\Big[\Big(-2T+\Delta T(-2+\epsilon+\epsilon^2)\Big)\,\mathrm{e}^{-k(1-\epsilon)t/\gamma}+\Big(2T+\Delta T(2+\epsilon-\epsilon^2)\Big)\,\mathrm{e}^{-k(1+\epsilon)t/\gamma}\Big] \quad (4.32)$$

A few physical comments can be made about these results:

- If $\Delta T = 0$, we retrieve the cross-correlation function for two particles interacting in a thermal bath at equilibrium already calculated in [97–99] (see equation 4.24).
- In our case $\langle x_1(t)x_2(0)\rangle \neq \langle x_1(0)x_2(t)\rangle$ because we introduce an asymmetry by forcing only one bead.
- Of course, we retrieve the fact that $\langle x_1(0)x_2(0)\rangle \neq 0$ when $\Delta T \neq 0$, contrary to the equilibrium case.
- $\langle x_1(0)x_2(t)\rangle$ always shows a time-delayed anti-correlations more pronounced than in the equilibrium case whereas $\langle x_1(t)x_2(0)\rangle$ doesn't show any anti-correlation as soon as $\Delta T \geq 2T/[\epsilon(1-\epsilon)]$. This behaviour can be understood in the following way: $\langle x_i(0)x_j(t)\rangle$ is linked to how x_j at a time $t>0$ is influenced by x_i at the time $t=0$. Since x_1 is forced, it is less sensitive to the motion of x_2. On the contrary, x_2 is more sensitive to the motion of x_1 which is bigger than its own motion.

Since every parameter can be measured (k_1 and k_2 are estimated independently, γ is known for water, and ϵ, ΔT and T are estimated from the values of the variances), we can directly test equations 4.31 and 4.32 on our data. Some experimental cross-correlations $\langle x_1(0)x_2(t)\rangle$ are shown in figure 4.9 and compared to the theoretical predictions with the measured values of the parameters. For those measurements, the distance is $d = 3.2\,\mathrm{pN/\mu m}$ and the stiffnesses are $k_1 = 3.3\,\mathrm{pN/\mu m}$ and $k_2 = 3.7\,\mathrm{pN/\mu m}$. Here we have taken $k = (k_1+k_2)/2$ and we do not show the predictions from equations 4.28 and 4.29, because they are very close to the ones where we assume $k_1 = k_2 = k$. The predictions are not perfectly verified on the experimental data, but since we took no free parameter to adjust the data and the theoretical curves, the agreement is still very satisfactory. In particular, the strong asymmetry and the increase of instantaneous cross-correlation when ΔT is increased are very clear.

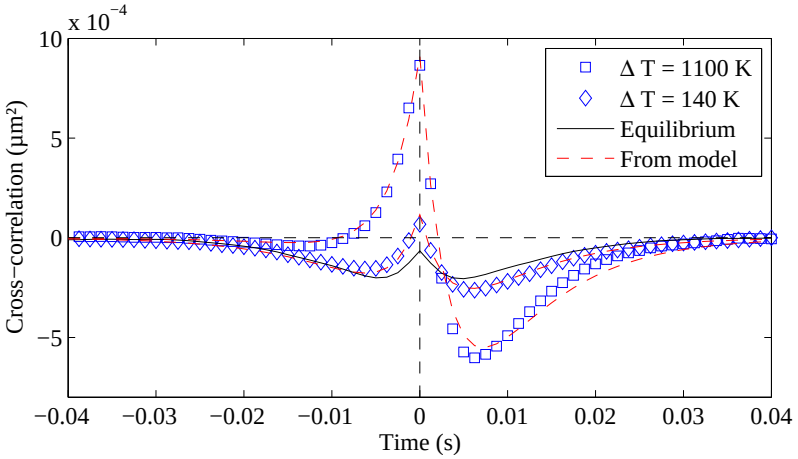

Figure 4.9: Experimental position cross-correlation functions $\langle x_1(0)x_2(t)\rangle$, for two particles trapped at a fixed distance $d = 3.2\,\mu\text{m}$, with different effective temperatures ΔT applied on particle 1. The black curve is a measurement for $\Delta T = 0$, the function is not 0 at $t = 0$ because the distance between the particles is too small, as in figure 4.8. The red curves are the predictions from equations 4.31 and 4.32.

4.4 An experimental set-up with one single laser beam

We used the set-up described in figure 4.1 because we wanted two real physical traps, but it requires a very good precision in the alignment of the two laser beams to avoid optical aberrations. We also tested a simpler set-up, where the two traps are created by only one beam which is switched very rapidly between two positions thanks to the acousto-optic deflector (AOD)[5]. To create the same situation as before, we simply switch the laser beam between one fixed position (which will be the trap at equilibrium temperature T) and a position which is randomly modulated (which will be the trap at effective temperature $T + \Delta T$). In this case, we have two control frequencies: a very high frequency (10 kHz) which is the frequency of switching positions between the two traps, and a lower frequency (1 kHz) which is the cut-off frequency of the white noise sent to modulate the position where we want to create the effective temperature. An example of the control signal that can be sent to the AOD is shown in figure 4.10: the lower position is fixed and the upper position is modulated by a numerically low-pass filtered Gaussian white noise.

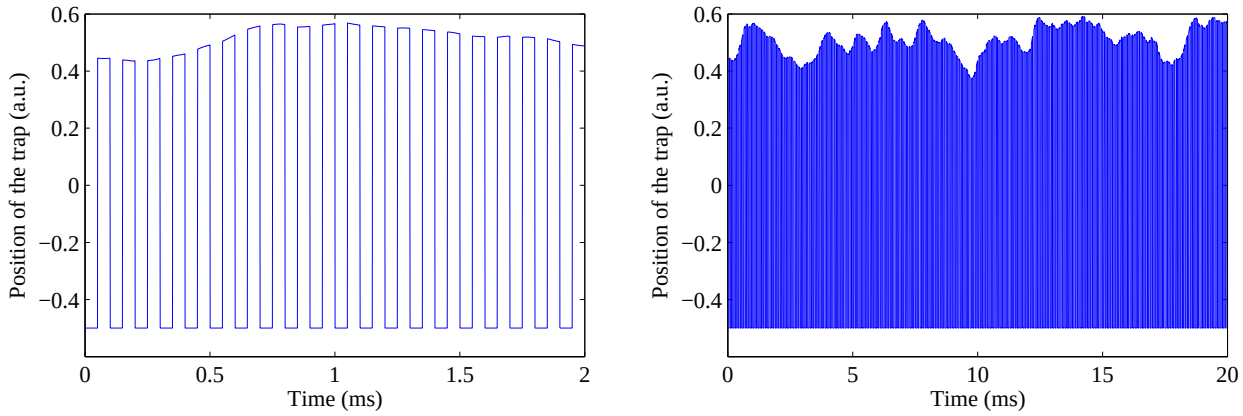

(a) Small time scale

(b) Larger time scale

Figure 4.10: Example of control signal that can be sent to the acousto-optical deflector to create two independent traps by switching rapidly the position of one single laser beam. One trap has a fixed position (-0.5 in arbitrary units) and is at equilibrium with the fluid. The other trap is randomly modulated around its mean position ($+0.5$ in arbitrary unit) so that the trapped particle will have a higher effective temperature.

This set-up is easier to use than the one presented in the previous section and gives similar results. The data presented in the following section were done using this simpler set-up.

[5]The set-up is then the same as the one presented in chapter 2.

4.5 Stochastic heat dissipated by the particles

Once the hydrodynamic model has been validated, we can look at some stochastic thermodynamics quantities. For example we can compute the heat flux between the two particles, to see if it respects the Second Law of Thermodynamics and if it verifies a Fluctuation Theorem for two sources at different temperatures.

4.5.1 Average heat and work exchanges

We consider that ξ_1 and ξ_2 are the normalised effective Brownian random forces acting on particles 1 and 2, *i.e.* the forces due to their respective heat bath. Following [30], the heat dissipated by the particle i during the time τ is given by:

$$Q_i(\tau) = \int_0^\tau (\gamma \dot{x}_i - \gamma \xi_i)\, \dot{x}_i \, \mathrm{d}t. \tag{4.33}$$

Using equations 4.10 it can be decomposed in two terms:

$$Q_i(\tau) = Q_{ii} + Q_{ij} \tag{4.34}$$

Where:

$$\begin{aligned} Q_{ii} &= -k_i \textstyle\int_0^\tau x_i \dot{x}_i \, \mathrm{d}t \\ Q_{ij} &= -\epsilon k_j \textstyle\int_0^\tau x_j \dot{x}_i \, \mathrm{d}t \end{aligned} \tag{4.35}$$

with $j \neq i$ (*i.e.* $j = 2$ if $i = 1$ and reciprocally). We experimentally measured the four Q_{ij} (with $\{i, j\} \in \{1, 2\}$) for different parameters and computed their average[6]. We plot in figure 4.11a the four $\langle Q_{ij}(\tau) \rangle$ for $\tau = 0.2\,\mathrm{s}$. The quantities are expressed in $\mathrm{k_B T}$ units, where T is the room temperature, which is the real equilibrium temperature of the bath ($T \approx 300\,\mathrm{K}$). The quantities $\langle Q_{11} \rangle$ and $\langle Q_{22} \rangle$ are equal to zero. This is normal since:

$$\int_0^\tau -x_i \dot{x}_i \, \mathrm{d}t = -\left[\frac{1}{2} x_i^2\right]_0^\tau. \tag{4.36}$$

We also see that $\langle Q_{12} \rangle = -\langle Q_{21} \rangle$. Here this effect is due to the fact that $k_1 \approx k_2$, otherwise we would simply have:

$$\left\langle \int_0^\tau x_1 \dot{x}_2 \, \mathrm{d}t \right\rangle = -\left\langle \int_0^\tau x_2 \dot{x}_1 \, \mathrm{d}t \right\rangle \tag{4.37}$$

because the boundary term in the integration by parts vanishes in average:

$$\langle [x_1 x_2]_0^\tau \rangle = \sigma_{12}^2 - \sigma_{12}^2 = 0. \tag{4.38}$$

In figure 4.11b we show that $\langle Q_{ij} \rangle$ is linear in τ, which is expected because the system is stationary. A least squares numerical fit gives $-\langle Q_{12} \rangle = A\tau + B$ with $A = 21.7\,\mathrm{k_B T \cdot s^{-1}}$ and $B = -0.03\,\mathrm{k_B T}$ which is very close to 0.

Finally, the average heat dissipated by the particle i during a time τ is $\langle Q_i(\tau) \rangle = \langle Q_{ij}(\tau) \rangle$ and depends linearly in τ and in ΔT, as it would be observed for a normal stationary heat flux between two real heat baths at different temperatures. One could find strange that $Q_{12} < 0$ and $Q_{21} > 0$, because it means that the particle 1, which is in the hot bath, is receiving positive

[6] Since the system is stationary, the average is simply estimated by computing $Q(\tau)$ on different segments of trajectories that are considered independent.

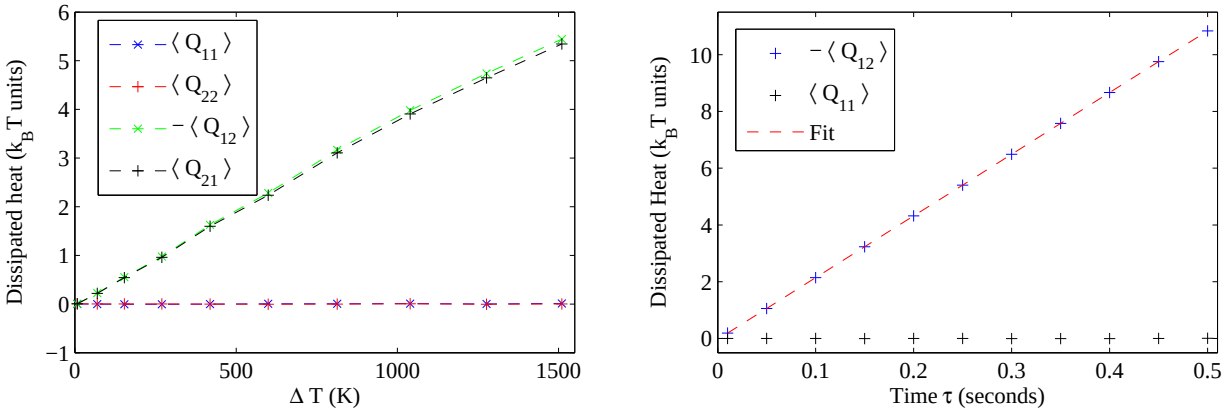

(a) (b)

Figure 4.11: Heat dissipated by the particles, with $d = 4.1\,\mu\text{m}$, $k_1 = 3.6\,\text{pN}/\mu\text{m}$ and $k_2 = 3.7\,\text{pN}/\mu\text{m}$. a) For $\tau = 0.2\,\text{s}$ and different ΔT. b) For $\Delta T = 1000\,\text{K}$ and different τ.

heat, whereas the particle 2, which is in the cold bath, is dissipating positive heat. Actually this is normal, since the two baths can only exchange heat through the interactions of the two particles. The mean heat flux has to go from the hot bath to the cold bath, then the particle in the hot bath must receive heat from its bath, whereas the particle in the cold bath must give heat to its bath. Of course, none of the particles can store energy, so we must verify that in average the work that they receive is equal to the heat that they dissipate.

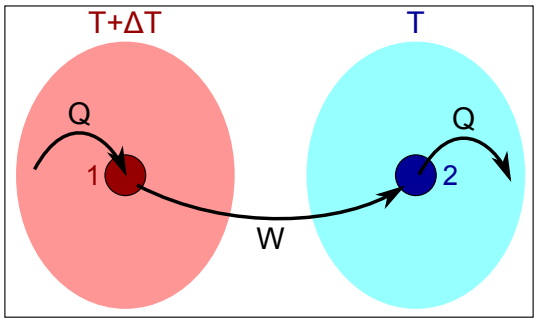

Figure 4.12: Schematic representation of energy exchanges in the system of two beads kept at different effective temperatures and coupled by hydrodynamic interactions, if $k_1 = k_2$. Q is positive heat and W positive work.

We consider that for particle 1, the particle 2 is an external agent (and reciprocally). Then [31], the heat received by the particle i during the time τ is given by:

$$W_i(\tau) = \int_0^\tau \frac{\partial V_i}{\partial x_j}(x_i, x_j, t)\dot{x}_j \, \mathrm{d}t \tag{4.39}$$

where $V_i(x_i, x_j, t) = \frac{1}{2}k_i x_i^2 + \epsilon k_j x_j x_i$ (and as before $j = 2$ if $i = 1$). Then:

$$W_i(\tau) = \epsilon k_j \int_0^\tau x_i \dot{x}_j \, \mathrm{d}t. \tag{4.40}$$

Using equation 4.37, it follows directly that:

$$\langle Q_i(\tau)\rangle = \langle W_i(\tau)\rangle. \tag{4.41}$$

This is the behaviour expected: the average heat dissipated by the particle i is equal to the average work received by this particle.

Finally, if $k_1 = k_2$, we can have a very simple picture of the energy exchanges in the system: the hot heat bath transfers heat to particle 1, which transfers work to particle 2, which transfers heat to the cold heat bath. A schematic representation is shown in figure 4.12. In the following part, we keep $k_1 = 3.6\,\mathrm{pN/\mu m} \approx k_2 = 3.7\,\mathrm{pN/\mu m}$.

4.5.2 Fluctuation Theorem for two sources at different temperatures

We can go further by looking not only at the average of the stochastic heat and work, but also at their fluctuations. In particular, the exchange Fluctuation Theorem (xFT) [81] states that the heat Q exchanged in a time τ between two systems previously kept in equilibrium at two different temperatures T_1 and T_2 verifies in the limit of large τ:

$$\ln\left(\frac{P(Q)}{P(-Q)}\right) = \left(\frac{1}{k_\mathrm{B}T_2} - \frac{1}{k_\mathrm{B}T_1}\right) Q \tag{4.42}$$

where $P(Q)$ is the probability of observing the amount of heat Q going from system 1 to system 2 during the time τ.

In our case, we can look at the heat that leaves the hot bath Q_1 or the heat that is received by the cold bath Q_2. The experimental Probability Distribution Functions (PDF) of the four Q_{ij} are shown in figure 4.13 for $\tau = 0.2\,\mathrm{s}$. The PDF of Q_{11} is wider when ΔT is higher, but it always remains symmetrical with zero mean. The PDF of Q_{22} is nearly not modified by the increase of ΔT and remains symmetrical with zero mean. The PDFs of Q_{12} and Q_{21} are nearly the opposite one of the other and are evolving significantly when ΔT is increased. When $\Delta T = 0$ they are Gaussian with zero mean, but as soon as $\Delta T > 0$ they have a non-zero average and their shape become asymmetrical with regard to their mean value. Since we compute the Q_{ij} in $\mathrm{k_B T}$ units, we can expect an exchange Fluctuation Theorem of the form:

$$\ln\left(\frac{P(Q_{21})}{P(-Q_{21})}\right) = \left(1 - \frac{T}{T+\Delta T}\right) Q_{21} \tag{4.43}$$

We call the symmetry function $\Sigma(Q) = \ln\left(P(Q)/P(-Q)\right)$.

The experimental symmetry function $\Sigma(Q_{21})$ for $\tau = 0.2\,\mathrm{s}$ and $\Delta T \approx 1000\,\mathrm{K}$ is shown in figure 4.14a. It is well verified that $\Sigma(Q_{21})$ depends linearly in Q_{21}. However, to be more quantitative, we have to check that the slope of $\Sigma(Q_{21})$ does not depend on τ, and is equal to $1 - T/(T+\Delta T)$. We show in figure 4.14b that the slope does not vary with τ, except for very short values (*i.e.* τ shorter than the relaxation time of the particles in the optical traps). We also show that the slope of $\Sigma(Q_{21})$ is very close to the slope of $\Sigma(-Q_{12})$, which is normal since the PDF of Q_{12} is nearly the opposite of the PDF of Q_{21}. Experimentally we have to choose a value of τ small enough to have a good statistic in the PDF near zero[7], and high enough to have a slope independent of τ. This is the reason why we chose $\tau = 0.2\,\mathrm{s}$.

[7] since $\langle Q_{21}\rangle$ increase linearly with τ, the PDF shifts far from $Q_{21} = 0$ when τ is increased

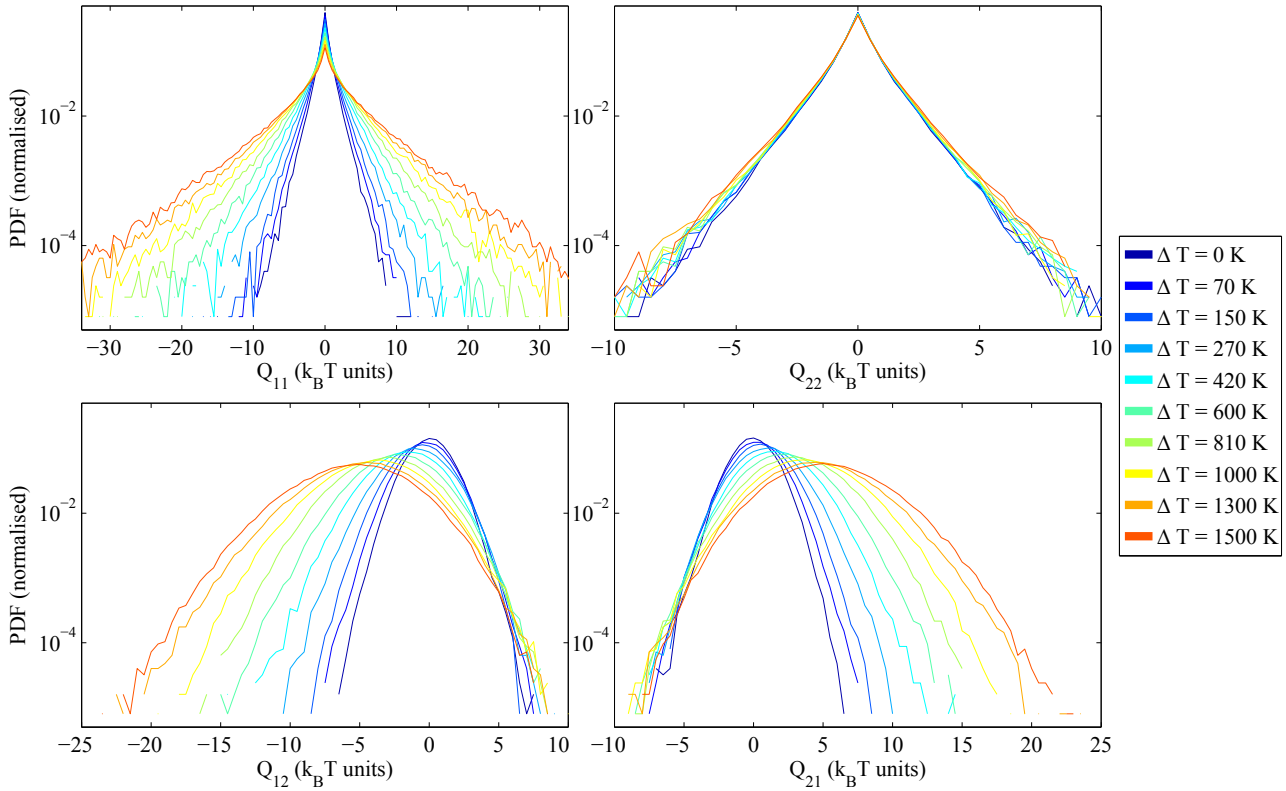

Figure 4.13: Experimental Probability Distribution Functions of the four heat terms Q_{ij}, computed with $\tau = 0.2\,\mathrm{s}$ for different ΔT.

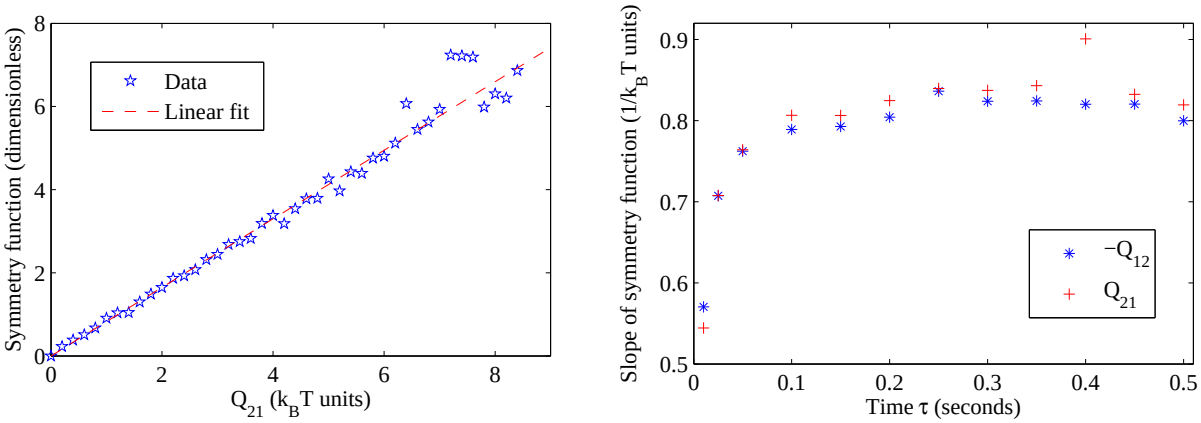

(a) Symmetry function

(b) Slope of the symmetry function

Figure 4.14: a) Symmetry function $\Sigma(Q_{21})$ computed for $\Delta T \approx 1000\,\mathrm{K}$ and $\tau = 0.2\,\mathrm{s}$ (ΔT is estimated from the hydrodynamic model). b) Slope of the symmetry function with $\Delta T \approx 1000\,\mathrm{K}$, computed for different τ.

Unfortunately, as seen in figure 4.15, the ΔT which is given by the slope of the symmetry functions is not in really good agreement with the one from the hydrodynamic model, as soon as $\Delta T > 300\,\mathrm{K}$.

This discrepancy can be explained by the difficulty to correctly estimate the slope of the

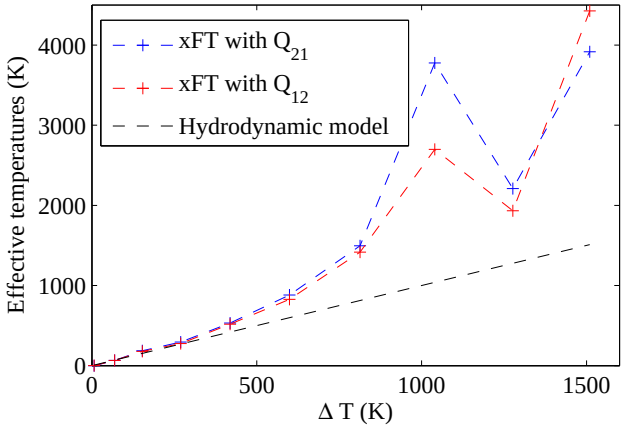

Figure 4.15: ΔT computed from hydrodynamic model (black) and the slope of the symmetry function, assuming that the exchange Fluctuation Theorem (equation 4.43) is verified.

symmetry function for high values of ΔT (because the slope should be in $1 - T/(T + \Delta T)$). In particular, the slope of the symmetry function can be greatly modified if the value of the stiffnesses k_1 and k_2 are not well estimated. For example, for a fixed forcing amplitude A, a change of only 5 % done to the stiffnesses taken in the calculation can vary the value of ΔT derived from the slope from 1200 K to 2300 K. In comparison the values of ΔT given by the hydrodynamic model varies only from 1280 K to 1430 K, for the same change of 5 % in k_1 and k_2. Given that we also need to estimate ϵ, the errorbars in figure 4.15 should be very big (at least 50 %). We nevertheless did some longer measurements (to increase the statistic in the PDF) with various forcing amplitudes. The ΔT measured from the hydrodynamic model and from the slope of the symmetry functions are presented in table 4.1.

Hydrodynamic model (K) ±10 %	xFT with Q_{12} (K) ±50 %	xFT with Q_{21} (K) ±50 %
613	675	675
1065	1574	1372
1429	1353	1293

Table 4.1: ΔT computed from hydrodynamic model and the slope of the symmetry function, assuming that the exchange Fluctuation Theorem (equation 4.43) is verified. The values are estimated for measurements of ~ 6 h continuously sampled at 800 Hz. The errorbars are estimated by taking into account the uncertainties of k_1, k_2 and ϵ.

Finally, it seems very difficult to conclude on the validity of the exchange Fluctuation Theorem for our experimental set-up. It seems well verified for values of ΔT which are reasonably small ($\Delta T \lesssim 300$ K), but the agreement for higher values of ΔT is not clear. It would however be interesting to study this point more deeply. Indeed it has been previously shown that when a random forcing term becomes larger than the thermal noise the Fluctuation Theorem fails [111, 115]. One can wonder whether we have here the same phenomenon, even if the accuracy of the experimental results does not allow us to check this hypothesis at the moment.

4.6 A note on effective temperature by random forcing

With the simpler set-up presented in section 4.4, it is possible to set the same effective temperature to both particles 1 and 2. We only need to generate two independent Gaussian white noises with same amplitude and filtered at a same given frequency, and to send one on each trap position controlled by the AOD. In this case, we have two particles trapped at the same effective temperature $T + \Delta T$.

Interestingly, the results are not exactly the ones expected for two particles in equilibrium in the same heat bath. For example, the variances σ_1^2 and σ_2^2 are nearly equal, but the cross-variance $\langle x_1 x_2 \rangle$ is not equal to zero. It is very visible in the position cross-correlation $\langle x_1(0) x_2(t) \rangle$ shown in figure 4.16: the cross-correlation is symmetrical in time because the beads play an equivalent role, but it shows a non-zero value at $t = 0$.

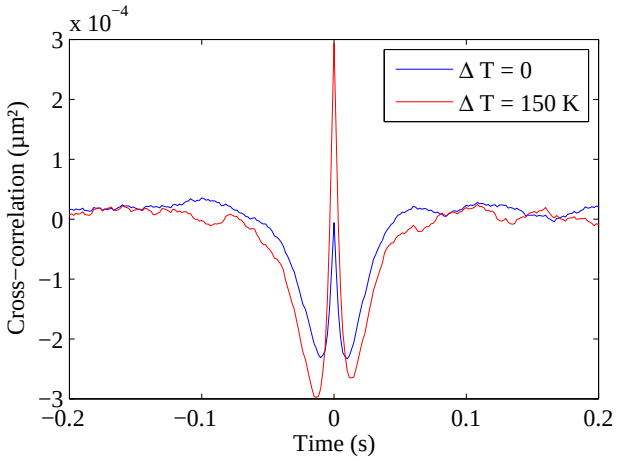

Figure 4.16: Position cross-correlation function $\langle x_1(0) x_2(t) \rangle$, computed for two particles trapped at distance $d = 3.6\,\mu\text{m}$ with the same effective temperature $T + \Delta T$. The curve for $\Delta T = 0$ is simply a measurement at equilibrium, with no noise added on any particle.

This effect is however normal, given that the noises added on each particle are independent. Indeed, in the equilibrium case, the Brownian random forces f_1 and f_2, which are due to the collisions with the fluid molecules, verify the properties:

$$\begin{aligned} \langle f_i(t) \rangle &= 0 \\ \langle f_i(t) f_j(t') \rangle &= 2 k_\text{B} T \, (\mathcal{H}^{-1})_{ij} \, \delta(t - t'). \end{aligned} \tag{4.44}$$

These properties are necessary to retrieve the fact that $\langle x_1 x_2 \rangle = 0$. Yet, the random forces f_1^* and f_2^* that we create only verify:

$$\begin{aligned} \langle f_i^*(t) \rangle &= 0 \\ \langle f_i^*(t) f_j^*(t') \rangle &= \delta_{ij} 2 k_\text{B} \Delta T \gamma \delta(t - t') \end{aligned} \tag{4.45}$$

where δ_{ij} is the Kronecker delta. Thus, it is normal that we do not retrieve completely equilibrium properties if the noises added on each particle are not chosen to satisfy particular relations.

This effect might remind us that we are dealing only with “effective” temperatures, and not “real” temperatures.

4.7 Perspectives and Conclusion

4.7.1 Perspectives

In this section, we briefly present some possible ways to extend our work on effective temperatures.

- It should be possible to compute the theoretical Probability Distribution Function of the dissipated heat with a Fokker-Planck equation as in [89]. It would be interesting to see if the theoretical results predict the validity of the suggested exchange Fluctuation Theorem (equation 4.43).
- One may wonder whether the presence of a randomly forced particle will modify the Kramers time [52] of another particle trapped nearby in a double well potential in the fluid at equilibrium, as represented in figure 4.17. We have tried to realise such an experiment, but it was really difficult to create a well calibrated double well potential nearby a forced trap with only one AOD, and we observed no significant effect in our preliminary measurements.

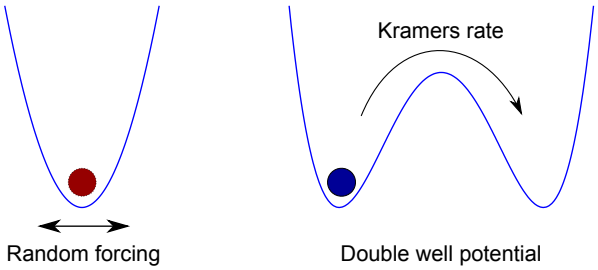

Figure 4.17: Schematic representation of one particle trapped at effective temperature, nearby a particle trapped in a double well potential at equilibrium. The Kramers time is the typical time needed by the particle in the double well potential to jump from one well to the other.

- One may study the cross-coupling between displacements in direction x and y. This requires two AODs but should not be much more complicated than what we have already done.
- One may study some conservative coupling between the particles, for example if they are charged, or if they are attached with a spring (or a spring-like tie). The difficulty will then be to separate the contribution due to the hydrodynamic coupling (which cannot be removed) from the contribution due to the conservative force between the particles. However, the results could then be compared with some other experiments with real temperature sources.
- One may try to achieve a negative ΔT using a feedback control on the position of one of the two traps, as in [116, 117].
- One may study interactions of more than two particles, as suggested in [103].
- One may look for different sources of effective temperatures, like shear flows, as it would be discussed in chapter 5.

4.7.2 Conclusion

In conclusion, we have studied the effect of hydrodynamic interactions between two particles trapped with optical tweezers in a fluid at temperature T, when one of them is randomly forced to have an effective temperature $T + \Delta T$.

We first have shown that the random forcing of the position of one trapped bead does not modify the trap stiffness and can be interpreted as an effective temperature for the bead. This result was previously shown in [79] by forcing the particle with an electric field, and we only changed the set-up used to create the external random force. Our set-up allows us to add different effective temperatures on different beads trapped nearby. Conversely the use of an electric field offers a bigger range of temperatures but cannot be applied locally to only one particle among others.

We have shown that the random forcing of one particle gives rise to an unusual instantaneous cross-correlation between the motions of the particles and an effective energy exchange from the "hot" bead to the "cold" bead. This behaviour was explained by using a classical hydrodynamic coupling model, and by resolving the two coupled Langevin equations with the equivalent Fokker-Planck equation. The hydrodynamic model allows us to compute the variances and cross-variances of particles positions, and to link them with both the effective temperature ΔT and the hydrodynamic coupling coefficient ϵ. It also predicts the position cross-correlation functions of the two particles, which are in good agreement with experimental observations.

We have also looked at stochastic thermodynamic quantities such as the stochastic heat or the work received by the particles. We have shown that the particle in the (effective) "hot" heat bath receives heat at a constant rate proportional to ΔT, whereas the particle in the (real) "cold" heat bath dissipates heat at a constant rate, also proportional to ΔT. We have also shown that for each particle the work received is equal to the heat dissipated in average. We have experimentally measured the Probability Distribution Functions of stochastic heat dissipated by the particles and we have tried to look for an exchange Fluctuation Theorem. Unfortunately, even if the experimental observations are not in total disagreement with the theoretical formula, the errorbars due to uncertainties on our experimental parameters do not allow us to clearly conclude on the validity of this exchange Fluctuation Theorem.

Finally, we have presented a few possible ways to extend our work on interactions between particles submitted to effective temperatures.

Chapter 5

External Noise due to a Shear-Flow

Pourquoi faire simple quand on peut faire compliqué ?

Devise Shadok

5.1 Introduction and Motivation

We have shown in chapter 4 that randomly modulating the position of one optical trap creates an effective temperature for the trapped particle. We then wanted to look for a more "physical" source of effective temperature for our trapped particle, that could be encountered in other experimental systems.

We chose to study the noise created by a shear-flow. Indeed, if a particle is trapped in a simple shear-flow, as represented in figure 5.1, its over-damped movement in the xy-plane will be described by the 2D Langevin equations [118]:

$$\begin{cases} \gamma\dot{x} = -k_x\, x + \gamma\dot{\Gamma} y + f_x \\ \gamma\dot{y} = -k_y\, y + f_y \end{cases} \tag{5.1}$$

where x and y are the coordinates of the particle relative to the trap position, γ is the Stokes friction coefficient ($\gamma = 6\pi R\eta$ with R the radius of the particle and η the viscosity of the fluid), k_x and k_y are the trap stiffnesses in x and y directions, $\dot{\Gamma}$ is the shear-rate, and f_x and f_y are the Brownian random forces due to the collisions with the molecules of fluid. The stochastic forces are supposed to be Gaussian white noise and verify:

$$\begin{gathered} \langle f_x(t)\rangle = 0 = \langle f_y(t)\rangle \\ \langle f_i(t) f_j(t')\rangle = \delta_{ij}\, 2k_{\mathrm{B}}T\gamma\, \delta(t-t') \end{gathered} \tag{5.2}$$

where $i, j \in \{x, y\}$, δ_{ij} is the Kronecker delta, k_{B} is the Boltzmann constant, and T the room temperature. With this description the y coordinate acts on the dynamics of the x coordinate due to the shear-flow, and it is simple to identify the term $\gamma\dot{\Gamma} y$ as a coloured noise acting on x.

The use of a shear-flow seems to be a good candidate to study the effect of a coloured noise acting on one particle, and to see if it can be described as an effective temperature. Moreover, this kind of system has already be widely studied in the past decades. For example the effects

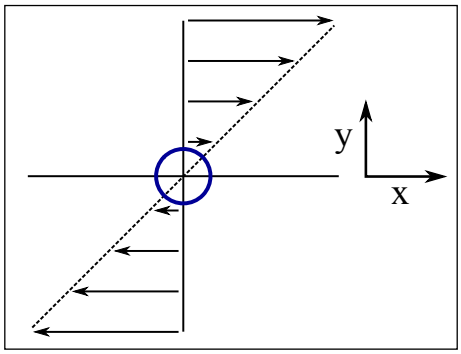

Figure 5.1: Schematic representation of one particle trapped in a shear-flow.

of a shear-flow on the diffusion of Brownian particles were studied both theoretically [119–121] and experimentally, using a rheometer placed on a confocal microscope [122]. Violations of the Fluctuations Dissipation Theorem (FDT) were numerically observed in a flow sheared beyond the linear response regime [123]. These effects are similar to those observed in glassy systems and allow for defining an effective temperature for the slow modes of the fluid [123, 124]. The hydrodynamic interactions of two particles trapped in a shear-flow were studied experimentally with a microfluidic system [125]. The shear-flow was shown to induce a non-zero instantaneous cross-correlation between displacements in perpendicular directions x and y, and to modify the Probability Distribution Functions (PDF) of particles positions [125, 126]. The Kramers rate for crossing the central barrier of a double-well potential was also numerically shown to be enhanced by a well chosen shear-flow applied to the fluid [127]. The diffusion and mobility of a single tagged particle in a sheared colloidal suspension was studied numerically [128, 129]. It was shown that the particle in the sheared suspension behaves like a trapped particle. And the relation between its response function and its velocity auto-correlation function can also be interpreted in terms of an effective temperature.

In this chapter our aim was to realise an experimental microfluidic system, that would allow us to trap one or several particles in a shear-flow. We were mostly inspired by the experimental set-up from [125]. We then wanted to test the Fluctuation Dissipation Theorem (FDT) for one particle trapped in the shear-flow. Since the system is out of equilibrium we await a clear violation of the FDT. We then tried to see if this violation could be interpreted in terms of an effective temperature, and if it could be linked to the amount of energy dissipated by the system using a Harada-Sasa equality [73]. Unfortunately, the microfluidic techniques required a lot of time to be mastered, and the final results were not obtained before the writing of this Thesis. This is the reason why we only present here a detailed description of the experimental set-up and some preliminary results.

5.2 Experimental set-up

In this section we describe the experimental microfluidic set-up used to create a shear-flow at the micro-scale. The set-up was mostly inspired by [125]. Denis Bartolo and Céleste Odier helped us in its realisation. The principle is the following: to create a shear-flow with zero mean velocity, two counter-propagating flows are sent in a microfluidic cell and meet in a central region. A schematic representation of the microfluidic cell's central region is shown in figure 5.2.

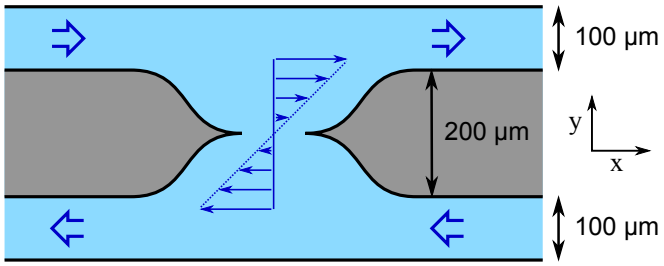

Figure 5.2: Schematic representation of the microfluidic cell with two counter-propagating flows that create a shear-flow with zero mean velocity in the central region.

5.2.1 Microfluidic cell

To create the microfluidic cell with two micro-channels joining in a central region, we have tried two different methods: one based on the UV-Curing Optical Adhesives "stickers" developed by Denis Bartolo and co-workers [130, 131], and one based on the standard PDMS[1] elastomer devices [132–134]. The main difference between them is their ability to resist to imposed pressure: the "stickers" are stiffer and do not deform themselves under high pressure flows. For us however, this point is not crucial since we are not going to work with rapid flows that would require high pressures to go through the micro-channels.

Shared steps

In both cases the first step is to realise a mould with the desired pattern for the cell. A magnified example of pattern is presented in figure 5.3. The difficulty is to make a mould with a good micro-scale resolution. People usually uses high-resolution printers ($\geq$ 5000 dpi) to create a transparency that will be used as a photomask in contact photolithography. Instead, we chose to use a micro-milling machine from *Minitech Machinery Corporation* to create plexiglas or aluminium moulds. The micro-milling machine can create patterns with a radius of curvature down to $\sim 10\,\mu$m (depending on the end mill used), it achieves really smooth vertical surfaces and a precision of a few microns in depth. As an example, we show on figure 5.4 two pictures of the central part of a double-channel microfluidic cell, made in plexiglas.

Depending on the method, the mould needs to be a positive or a negative image (in depth) of the desired pattern:

[1] Poly(dimethylsiloxane).

- In the case of the "stickers" technique, the mould must be a positive image of the microfluidic cell. It will be used to realise a negative mould in PDMS, that will itself be used to create the cell in *Norland Optical Adhesive 81* (NOA-81).

- In the case of the PDMS elastomer technique, the mould must be a negative image of the microfluidic cell. It will be used to directly create the cell in PDMS elastomer.

Depending on the exact shape of the microfluidic cell, it is not always possible to realise both a positive and negative image of it with the micro-milling machine, due to geometrical constraints. This is a reason why both techniques can be useful for us.

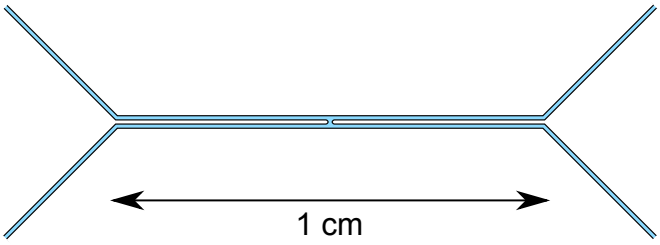

Figure 5.3: Example of pattern that needs to be engraved in a flat material to create the mould used to create microfluidic cells. The depth of engravement must be of $\sim 100\,\mu m$ and the design needs to have a good resolution at the micro-scale.

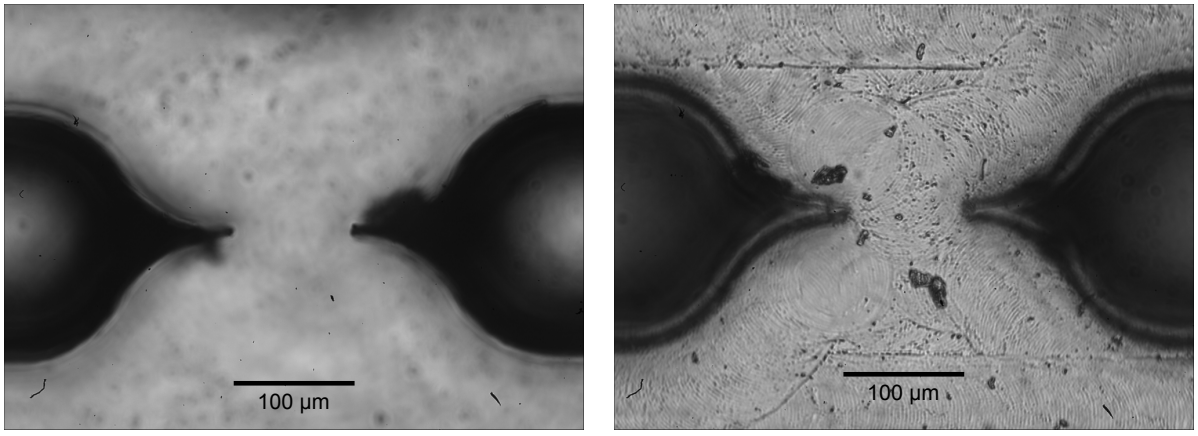

(a) Focus on the middle of the channel (b) Focus on the bottom of the channel

Figure 5.4: Microscope pictures of a channel engraved in plexiglas with the use of the micro-milling machine, with an end mill of diameter $100\,\mu m$. On the bottom of the channel, the grooves of the mill are visible, but have a very small depth ($\lesssim 1\,\mu m$.)

The second step is to realise a negative replica of the mould in PDMS elastomer. The PDMS is a silicon-based organic polymer which is cured by an organometallic cross-linking reaction to become an elastomer. The fabrication process is described below and summarised in figure 5.5:

- The mould is cleaned with an ultrasonic cleaner. If the mould is in plexiglas we use water with Micro-90® cleaning solution as a solvent. If the mould is in aluminium we use ethanol as a solvent. Then the mould is dried with a compressed air flow.
- The mould is surrounded with adhesive tape to create a small border that will allow us to pour a liquid solution inside. We use 3M™ office adhesive tape that we carefully press against the mould's edges. One should not use TimeMed® label tape, even if it is easier to stick, because it somehow reacts with PDMS when put at high temperature.
- A solution of liquid PDMS base (90 wt%) and curing agent (10 wt%) is prepared[2]. We use the commercial *Dow Corning* Sylgard® 184 silicone elastomer kit. The solution is very viscous and requires careful mixing. Then the solution is poured into the mould.
- The mould with the solution is placed in a vacuum bell jar connected to a vacuum pump. It stays under partial vacuum until all the air bubbles in the PDMS solution have disappeared. This usually takes ~ 1 h.
- The mould with the solution is placed in a laboratory oven to speed up curing. At room temperature the curing takes ~ 48 h. At 60 °C it takes ~ 4 h. It is faster at higher temperatures but the limitation is the maximal temperature that the mould (if it's in plexiglas) or the adhesive tape can tolerate without degrading.
- After curing, the PDMS is a solid elastomer, which is colorless and transparent. It is carefully removed from the mould to be used in the following steps of the microfluic cell fabrication.

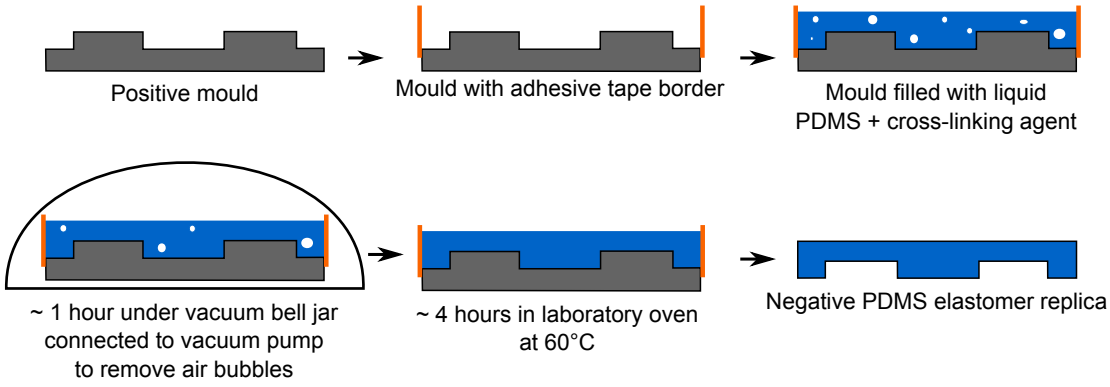

Figure 5.5: Schematic representation of steps to create a negative replica of a mould in PDMS elastomer.

The next steps depend on the technique used and are detailed in the following subsections.

NOA-81 stickers technique

For the "stickers" technique, we use the UV-Curing NOA-81 to create a negative replica of the PDMS elastomer mould previously made. The process has to be done in a clean-room

[2]To make a harder elastomer, one can put more than 10 wt% of curing agent.

to avoid dust being trapped into the microfluidic cell. We use a microscope slide previously drilled so that its holes correspond to the inlets/outlets of the microfluidic cell. The fabrication is described below and summarised in figure 5.6:

- The drilled microscope slide, a cover slip and the PDMS mould are carefully cleaned with isopropyl alcohol (IPA) and dried with a compressed air flow.
- The microscope slide is put on a flat surface (usually done in PDMS elastomer) and a droplet of NOA-81 is poured on it. To avoid injecting air in the NOA-81 it is better not to press too much its container.
- The PDMS mould is carefully pressed against the slide, squeezing the droplet. This step is rather difficult because one must take real care to avoid air bubbles being trapped in the NOA-81. It is recommended to keep the PDMS in partial vacuum before using it, so that it will spontaneously absorb some of the air bubbles. We use a stereo microscope to verify that there is no air bubble trapped in the NOA-81.
- The NOA-81 is submitted to UV for a controlled time to achieve a partial curing. PDMS is permeable to O_2 which inhibits the curing reaction. Thus the NOA-81 in the bulk is cured and becomes rigid, but the thin upper layer in direct contact with the PDMS mould remains liquid. It can then be glued to the cover slip to seal the microfluidic cell.
- The PDMS mould is removed, and holes are made in the NOA-81 with a needle.
- Finally, the cover slip is placed on the open side of the cell to seal it, and carefully pressed against the NOA-81. The cell is then put for a long time under a UV lamp to end the curing, which hardens the NOA-81 and closes the cell. For this step, it is easier to have a cover slip smaller than the PDMS mould, so that it will not go over the edges of the partially cured NOA-81.

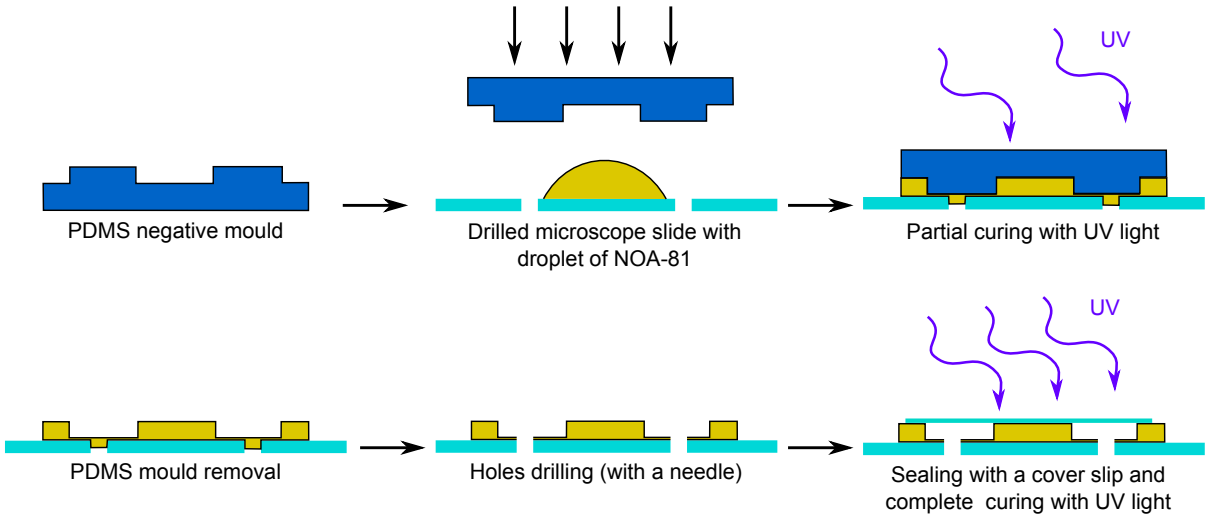

Figure 5.6: Schematic representation of steps to create a microfluidic cell from a PDMS mould with the NOA-81 “stickers” technique.

PDMS elastomer technique

The PDMS elastomer technique is simpler: the PDMS replicate of the initial mould will directly be used as the microfluidic cell. To close the cell, we do a plasma treatment of the PDMS so that it will bond on an oxidized glass surface. Other effects of plasma treatment on PDMS surfaces were recently studied in [135, 136]. The fabrication process is the following:

- Holes are extruded in the PDMS open cell with a biopsy punch of known diameter.
- The PDMS open cell and a cover slip are cleaned with isopropyl alcohol and dried with a compressed air flow.
- The PDMS open cell and the cover slip are put in a Harrick Plasma cleaner (PDC-002) for 1 min. The plasma does an oxidation of the PDMS so that it will covalently bond on the oxidized cover slip by the creation of a Si-O-Si bond.
- The cell is closed by carefully putting the oxidized surface of the cover slip on top of the oxidized PDMS.
- The closed cell is put on a hot plate at 40 °C for 20 min to ensure an homogeneous sealing.

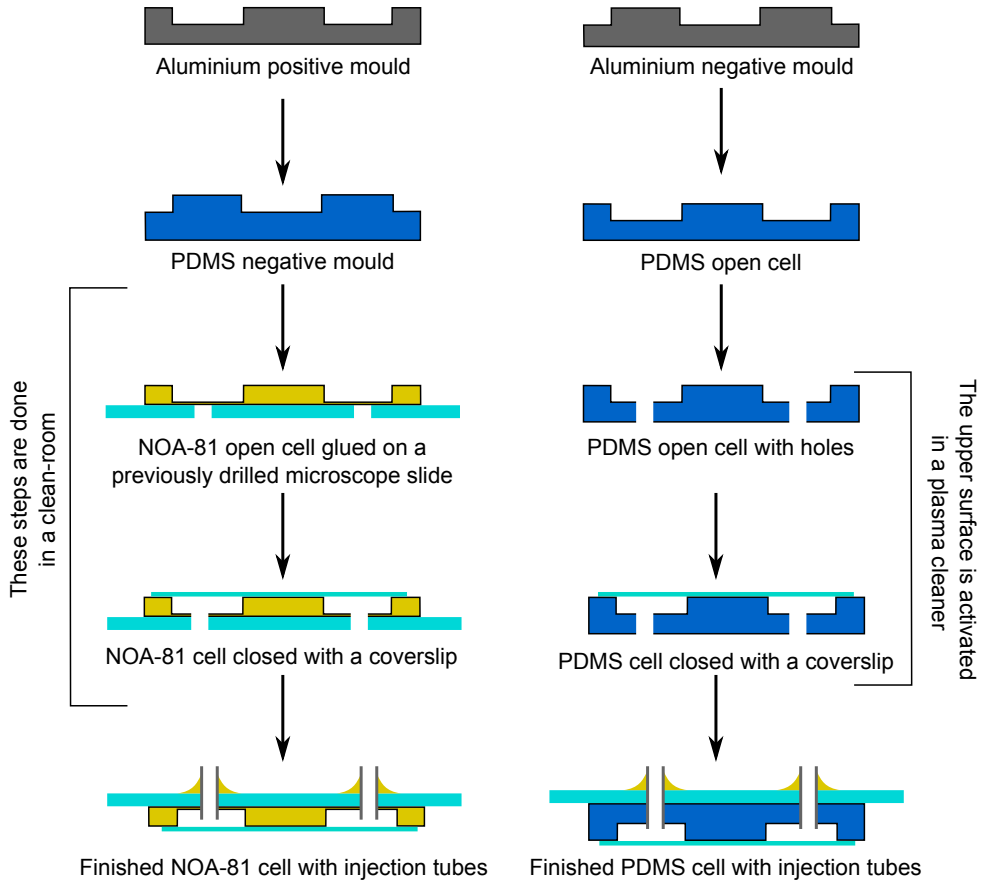

Figure 5.7: Summary of the two methods to make a microfluidic cell. Left: "stickers" technique. Right: PDMS elastomer technique.

The final step of both methods, is to add small metal tubes that will allow us to connect inlets/outlets to a water circuit. The tubes are chosen to exactly match the size of the holes (this is especially important for the PDMS technique). Then they are glued to the microscope slide using NOA-81. The two complete processes are summarised on figure 5.7.

The final cell

As already mentioned, mastering the different microfluidic techniques required some time and, at the moment when this Thesis is written, we only ended up with improvable prototypes. One of them is shown in figure 5.8. It was made with the PDMS elastomer technique, from an aluminium mould. The central region is simpler that the one presented in figure 5.2 but has nice edge and bottom shape. The depth of the channel is 100 µm. We have put large circles at the end of each micro-channel to simplify the connection with the metal tubes. Retrospectively, we should not have put these circles because small air bubbles tend to get stuck in these large areas. One should rather use a design without circles, as presented in figure 5.3.

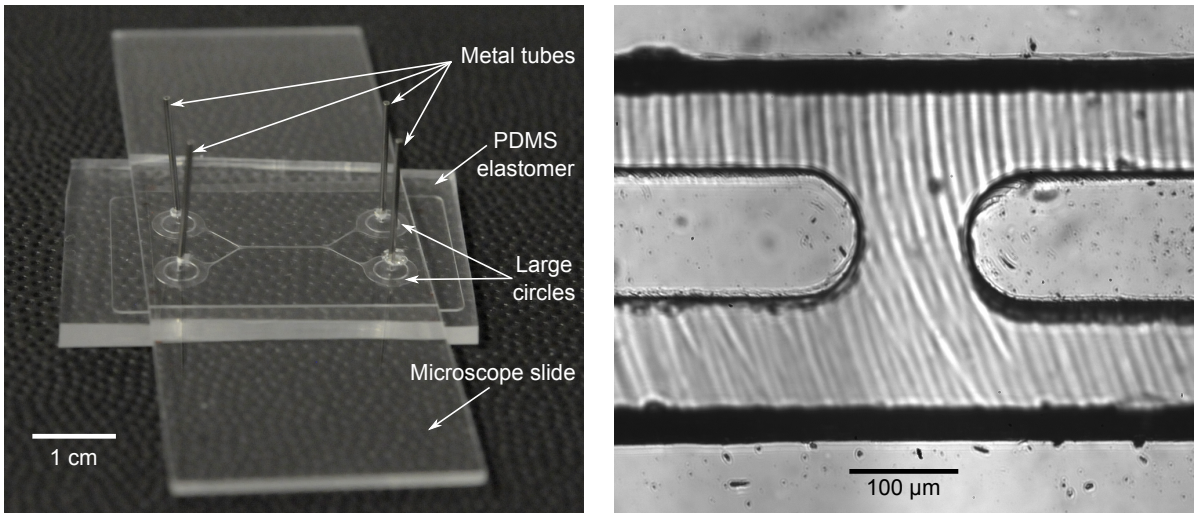

(a) Large view (b) Microscope view of the central part

Figure 5.8: Pictures of a PDMS elastomer cell with two channels meeting in the central region. This cell can be directly used on our custom-made optical tweezers.

The microfluidic cell we made is designed to be directly compatible with our custom-made optical tweezers set-up. Hence, we can easily trap particles in the central region of the cell and follow their Brownian motion with the usual method.

5.2.2 Fluid flow

To create the two counter-propagating fluid flows, we need to inject water in the two micro-channels, as represented in figure 5.9.

We first used a syringe pump (*Harvard Apparatus PHD 2000*) to impose the fluid flow. We connected each inlet to a syringe, and both syringes were controlled by the same syringe pump. Hence, both micro-channels should have the same fluid flow, whatever the small differences that

may exist between them[3]. Unfortunately, the use of the syringe pump was not very compatible with the optical tweezers measurements. We saw a lot of noise on the motions of particles trapped in the microfluidic cell, even when there was no flow induced by the pump. We believe that the stepper motor of the pump was inducing vibrations in the whole system. Moreover the plastic syringes we used were too deformable and a fluid flow was still observed in the micro-channels several minutes after switching off the syringe pump. Finally, it was not easy to introduce micro-particles in the cell because the syringes were placed horizontally in the pump and the silica particles tend to sediment inside them.

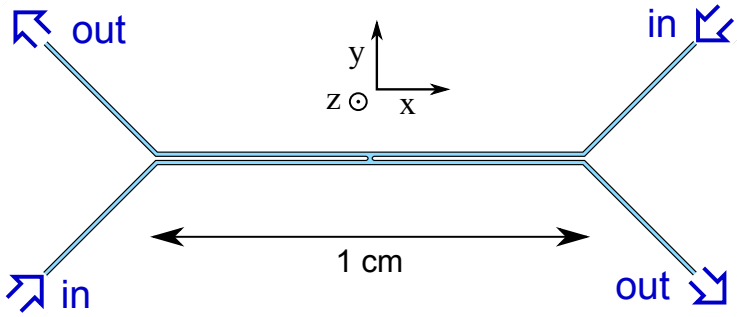

Figure 5.9: Schematic representation of the microfluidic cell with water inlets and outlets.

For these reasons, we finally chose to use flows driven by gravitational potential difference. The set-up is the following: a water tank filled with bidistilled water is connected to a 4 ways switching valve, with a "T" port (allowing to connect together 3 of the 4 ways). Two ways are connected to the inlets of the microfluidic cell. The fourth way of the switching valve is connected to a syringe with a solution of silica micro-particles (radius $R = 1.00 \pm 0.05\,\mu m$) dispersed in bidistilled water. This syringe allows us to manually inject particles in the cell when needed, and can be easily deconnected thanks to the switching valve. Each outlet of the cell is connected to a small beaker with a tunable water height inside. We use flexible Tygon® S-54-H tubing. We call h the vertical distance between the water tank and the beakers, and Δh the difference of water level between the two beakers. When the tank is connected to the two inlets, the water flows through the cell thanks to the pressure difference $\Delta P = \rho g h$ (with g the gravitational acceleration and ρ the density of water). Since we want really small fluid velocities, we need a very small flow rate (typically $\sim 1\,\mu L \cdot min^{-1}$). Thus about 10 cm of PEEK® polymer tubing with 100 µm inside diameter are added at the end of the outlet tubing to increase the hydraulic resistance of the complete microfluidic device. It allows us to have reasonable height $h \approx 10\,cm$ for the desired flow rate. The tunable height Δh between the beakers' water levels allows us to equilibrate the counter-propagating flows in the two micro-channels if their hydraulic resistances are not equal. Since the flow rates are really small compared to the volume of the beakers and of the water tank, we can consider that the water level does not significantly change during the experimental times (*e.g.* a few hours). All the connections between tubing are done with standard connectors (for example fittings with a ferrule). The set-up is schematically represented in figure 5.10.

[3]Even though the microfluidic cell is built to be symmetrical, we cannot be sure that both micro-channels have the same exact hydraulic resistance.

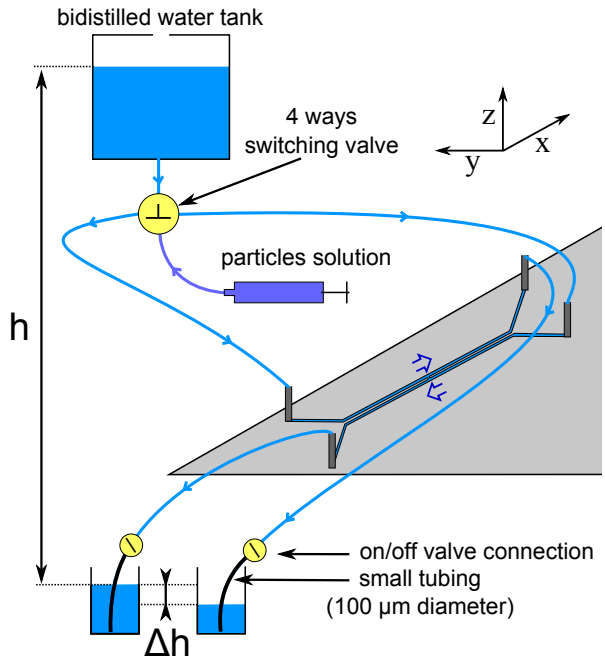

Figure 5.10: Schematic representation of the tubing set-up used to connect the microfluidic cell to a water tank. The fluid flow is driven by the gravitational potential difference $\Delta P = \rho g h$.

5.2.3 A word on "effective" shear-flows

Before building the microfluidic set-up, we tried different approaches to achieve an "effective" shear-flow, without really shearing the fluid. The simplest one is to use our usual optical tweezers set-up with a single laser beam and an acousto-optic deflector (AOD) that allows us to modulate the position of the trap in the x-direction. The set-up is schematically represented in figure 5.11 and is equivalent to the one used in chapter 2. Our camera is able to track one particle at a maximum speed of 1600 Hz.

With this set-up, we can change the position of the trap x_0 to add a force acting on the trapped particle f_{AOD}, as described in chapter 4. Then the x-displacement of the particle verifies the over-damped Langevin equation:

$$\gamma \dot{x} = -kx + f_{\mathrm{AOD}} + f_x \tag{5.3}$$

and we can choose f_{AOD} to have the same statistical properties as the y-displacement of the particle[4]. Then, f_{AOD} becomes equivalent to the force due to a flow with a shear-rate $\dot{\Gamma} \propto A$, where A is the amplitude of f_{AOD}. Of course, in this case f_{AOD} is only a numerically generated coloured noise and is not really equal to $\gamma \dot{\Gamma} y$.

One could really apply an external force proportional to the y-displacement by using a feedback loop. This is easy to do in principle but requires a fast enough acquisition and processing rate, so that the position y measured at time t can be applied on the position of the trap at a time t' close enough to t.

We also thought about another way to create an effective shear-flow by rotating the trap in the xy-plane at a speed slow enough so that the particle can follow the trap displacement. The

[4]The y-displacement can be previously measured with the same particle trapped at equilibrium.

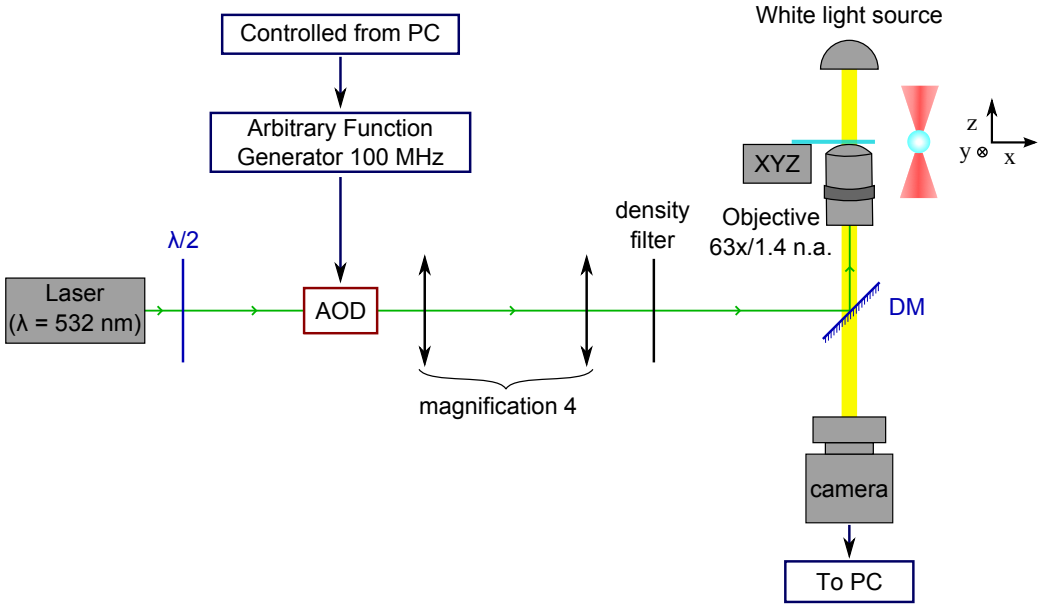

Figure 5.11: Schematic representation of our optical tweezers set-up with one acousto-optic deflector (AOD) to modulate the position of the trap in one direction (called x-direction).

rotation is schematically presented in figure 5.12: the trap is rotating at a constant speed ω_0 on a circle of radius r_0 and we call r and θ the polar coordinates of the trapped particle. Naively, one may think that because the particle's speed in the angular direction is $r\dot{\theta}$ with $\dot{\theta} \approx \omega_0$, a fluctuation in the radial coordinate r will change the speed in the angular coordinate. Hence, the particle should experience a shear-flow.

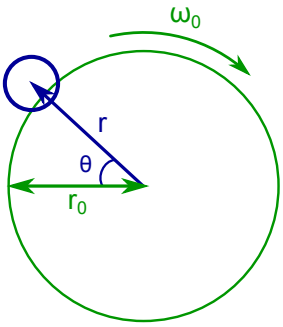

Figure 5.12: Schematic representation of one trap rotated at constant speed ω_0 on a circle of radius r_0. The polar coordinates of the trap particle are called r and θ.

Unfortunately, complete calculations show that this argument is a bit too simplistic. Indeed the equations of motion for the trapped particle are:

$$\begin{cases} \gamma\dot{x} = -k(x - r_0\cos\omega_0 t) + f_x \\ \gamma\dot{y} = -k(y - r_0\sin\omega_0 t) + f_y. \end{cases} \tag{5.4}$$

By solving the averaged equation, we find:

$$\langle x(t)\rangle = \langle r\rangle \cos(\langle\theta(t)\rangle) \tag{5.5}$$

with:

$$\begin{aligned} \langle r\rangle &= \frac{r_0}{\sqrt{1+\omega_0^2\gamma^2/k^2}} \\ \langle\theta(t)\rangle &= \omega_0 t - \phi \\ \phi &= \arctan\left(\frac{\omega_0\gamma}{k}\right). \end{aligned} \tag{5.6}$$

Which means that on average, the particle is rotating at a constant speed ω_0 on a circle of radius $\langle r\rangle < r_0$, with a phase change of ϕ with regard to the trap's rotation.
Then the system of equations 5.4 can be rewritten in the polar coordinates:

$$\begin{cases} \gamma\dot{r} = -k\left(r - r_0\cos(\omega_0 t - \theta)\right) + f_r \\ \gamma r\dot{\theta} = k r_0 \sin(\omega_0 t - \theta) + f_\theta \end{cases} \tag{5.7}$$

with:

$$\begin{aligned} f_r &= f_x\cos\theta + f_y\sin\theta \\ f_\theta &= -f_x\sin\theta + f_y\cos\theta \end{aligned} \tag{5.8}$$

Finally, by looking at the first order in small fluctuations $\delta r = r - \langle r\rangle$ and $\delta\theta = \theta - \langle\theta\rangle$, we find:

$$\begin{cases} \gamma\dot{\delta r} = -k\delta r + \gamma\omega_0\langle r\rangle\delta\theta + f_r \\ \gamma\langle r\rangle\dot{\delta\theta} = -k\langle r\rangle\delta\theta - \gamma\omega_0\delta r + f_\theta. \end{cases} \tag{5.9}$$

Thus we find two coupled Langevin equations that are not equivalent to the equations in the case of a real shear-flow (equations 5.1).

5.3 Preliminary results

Since a fully operational microfluidic cell was not realised before the writing of this Thesis, we only present here some preliminary results that were obtained with "effective" shear-flows and with cell prototypes.

5.3.1 Simulating a shear-flow using an AOD

By applying a random coloured noise on the x-displacement of one trapped particle, we achieve a situation similar to an "effective" shear-flow. The particle's motion is described by the over-damped Langevin equations:

$$\begin{cases} \gamma \dot{x} = -k_x\, x + f_{\mathrm{AOD}} + f_x \\ \gamma \dot{y} = -k_y\, y + f_y \end{cases} \tag{5.10}$$

where x and y are the coordinates relative to the trap position, γ is the Stokes friction coefficient ($\gamma = 6\pi R\eta$ with R the radius of the particle and η the viscosity of the fluid), k_x and k_y are the trap stiffnesses in x and y directions (here $k_x \approx k_y \approx 3.1\,\mathrm{pN/\mu m}$), f_{AOD} is the external noise creating by displacing the AOD, and f_x and f_y are the Brownian random forces. The external force f_{AOD} is a Gaussian white noise with an amplitude A (in volts), low-pass filtered with a cut-off frequency chosen to be $f_c = k_y/(2\pi\gamma) \approx 30\,\mathrm{Hz}$. When $A \neq 0$ the system quickly reaches an non-equilibrium steady-state.

The experimental Power Spectral Densities (PSD) of x and y are shown in figure 5.13 for different values of A. As expected, the y-displacement of the particle is not modified by the noise added to x: the PSDs are Lorentzians. The PSD of the x-displacement shows an increase at low-frequencies for increasing values of A but always matches with the equilibrium PSD at high-frequencies. By comparison with numerical simulations, we found that $A = 0.5\,\mathrm{V}$ corresponds to $\dot{\Gamma} \approx 180\,\mathrm{s}^{-1}$ and $A = 1\,\mathrm{V}$ to $\dot{\Gamma} \approx 360\,\mathrm{s}^{-1}$.

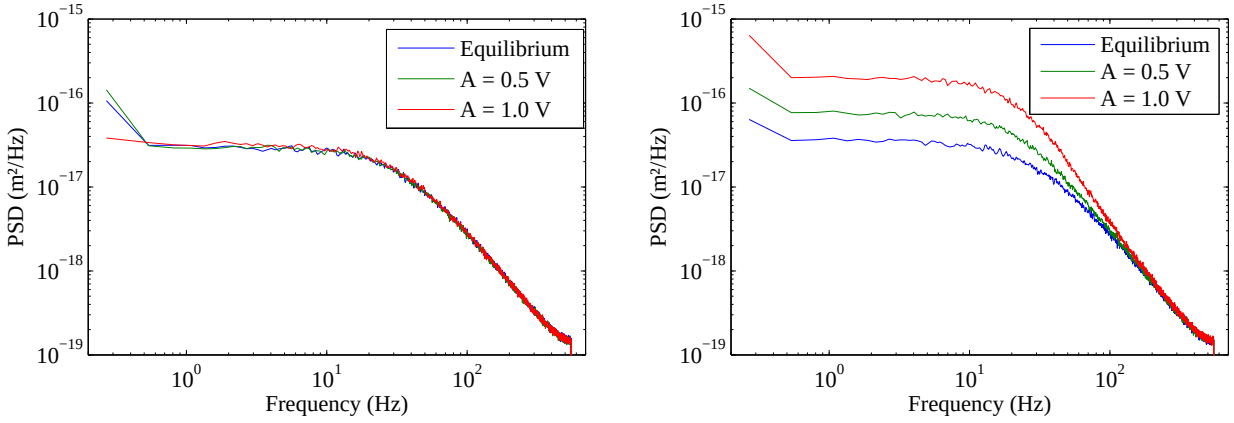

(a) y-displacement PSD (b) x-displacement PSD

Figure 5.13: Measured Power Spectral Densities (PSD) of the particle's motion for different random forcing amplitude.

To test the Fluctuation-Dissipation Theorem (FDT) we measured the response to an Heaviside change of the trap's position. For these measurements, the position of the trap is changed

from X_1 to X_2 at a given time called $t = 0$. The system is then let return to its new (non-equilibrium) stationary state during a time τ. After this time[5], the trap's position is again changed from X_2 to X_1, and the procedure is repeated alternatively. Since the system is supposed to be stationary and ergodic, each change of trap's position can be considered as and independent realisation of the same Heaviside perturbation, and we can average them to compute a response function:

$$\begin{aligned}\chi(t) &= \frac{\langle x(t)_{\text{perturbed}} - x(t)_{\text{unperturbed}} \rangle}{\text{perturbation amplitude}} \\ &= \frac{\langle x(t) \rangle - X_{\text{initial}}}{k_x (X_{\text{final}} - X_{\text{initial}})}\end{aligned} \tag{5.11}$$

where $[X_{\text{initial}}; X_{\text{final}}] = [X_1; X_2]$ or $[X_2; X_1]$.
If the FDT is verified, the response function should verify:

$$\chi(t) = \frac{1}{k_{\text{B}} T} (\text{C}_{xx}(0) - \text{C}_{xx}(t)) \tag{5.12}$$

where $\text{C}_{xx}(t)$ is the auto-correlation function of the x-displacement computed when no Heaviside perturbation is applied:

$$\text{C}_{xx}(t) = \langle (x(0) - \langle x \rangle)(x(t) - \langle x \rangle) \rangle \,. \tag{5.13}$$

Nota Bene: since we take the trap's position as the origin of the x-axis, we directly have $\langle x \rangle = 0$ and $\text{C}_{xx}(t) = \langle x(0)x(t) \rangle$.

The experimental response and auto-correlation functions are shown in figure 5.14. The response function is not modified by the external random force, whereas the auto-correlation function is modified (which was expected, because the auto-correlation function is theoretically the Fourier Transform of the Power Spectral Density). Thus, we have a clear violation of the FDT (equation 5.12) when $A \neq 0$, which was also expected because we are not at equilibrium.

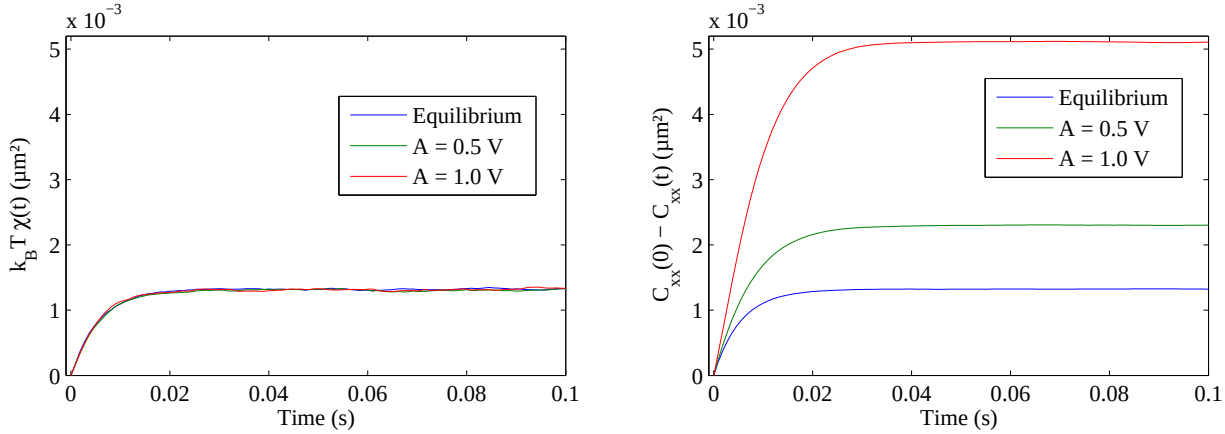

(a) Response functions

(b) Auto-correlation functions

Figure 5.14: Measured response functions $k_{\text{B}} T \chi(t)$ and auto-correlation functions $\text{C}_{xx}(0) - \text{C}_{xx}(t)$ of the particle's x-displacement, for different random forcing amplitudes.

[5]For the experiment $\tau = 5\,\text{s}$ which is long compared to the typical relaxation time of the particle: $1/f_c \approx 0.03\,\text{s}$.

An usual way to see if this violation can be interpreted as an effective temperature is to plot the response function with respect to the correlation function. We chose to plot $\chi_{\text{norm}}(t)$ with respect to $\text{C}_{\text{norm}}(t)$, which are normalised response and correlation functions:

$$\chi_{\text{norm}}(t) = \frac{k_{\text{B}} T \chi(t)}{\text{C}_{xx}(0)} \tag{5.14}$$

$$\text{C}_{\text{norm}}(t) = \frac{\text{C}_{xx}(t)}{\text{C}_{xx}(0)} \tag{5.15}$$

If the FDT is verified $\chi_{\text{norm}}(t) = 1 - \text{C}_{\text{norm}}(t)$, and we have an linear function with a slope of -1. If the FDT is verified with an effective temperature$T_{\text{eff}} > T$, we should have a linear function with a slope < 1. The experimental data are presented in figure 5.15. We see that the FDT is verified at equilibrium, but when $A \neq 0$ the FDT is violated. This violation cannot be interpreted as an effective temperature because we do not have a linear relation between $\chi_{\text{norm}}(t)$ and $\text{C}_{\text{norm}}(t)$.

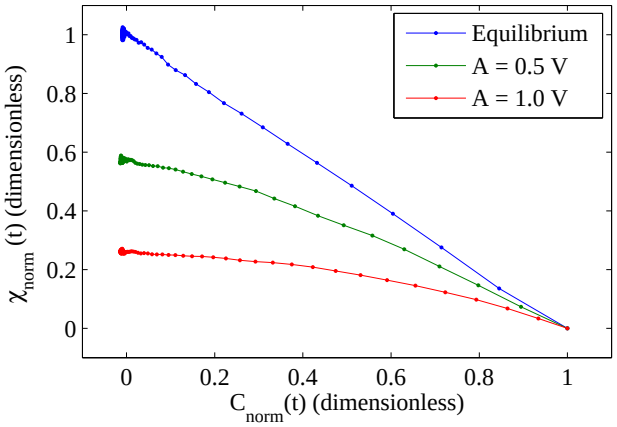

Figure 5.15: Measured normalised response functions $\chi_{\text{norm}}(t)$ plotted with regard to the measured normalised correlation functions $\text{C}_{\text{norm}}(t)$.

This result is not very surprising, since the random noise f_{AOD} was not chosen to verify the statistical properties awaited for a heat bath (contrary to what we have done in chapter 4). It was already visible in the PSDs (figure 5.13) that the external force could not be interpreted as an effective temperature, because the PSDs were not translations one of the others. These results are however a good basis and could be compared with results obtained in a real shear-flow.

5.3.2 First glimpse of microfluidic results

We also made some measurements with the microfluidic cell's prototypes. We had some experimental problems:

- The microfluidic cell was not perfectly symmetrical and it was difficult to equilibrate the flow speeds in the two micro-channels.

- We lacked reproducibility because air bubbles tend to get stuck in the tubing and change the hydraulic resistance of the microfluidic cell.
- We had no small tracers to visualise the fluid's flow and we used the silica beads to see the streamlines. We then had difficulties to trap only one particle, without being perturbed by the others' displacements.
- To achieve reasonable shear-flows, we had to increase the trap stiffness ($k \geq 10\,\mathrm{pN/\mu m}$) to be able to keep the particle trapped[6].
- Because all the valves and height control were manually operated, it was very difficult to change the flow speed without losing the trapped particle[7].
- It was difficult to control the flows so that the measured directions x and y correspond to the actual axes of the shear-flow.

We nevertheless had some encouraging results that are presented in figure 5.16. We trapped one particle in the region that was supposed to have zero-mean velocity, and we measured its x and y displacements. The PSD of x is bigger than the PSD of y at low-frequencies, but the two PSDs are equal at high frequencies. This corresponds to what is expected if the y displacement is acting on x through the coupling induced by the shear-flow. We also estimated the trapping potential shape $U(x, y)$ by computing the distribution of the particle's positions ($P(x, y) \propto \exp(-\frac{U(x,y)}{k_B T})$). As expected, the potential is skewed in the shear direction, even if it shows a rather strange shape. However, these preliminary measurements were hardly reproducible, and are clearly not sufficient to conclude yet on the validity of the results.

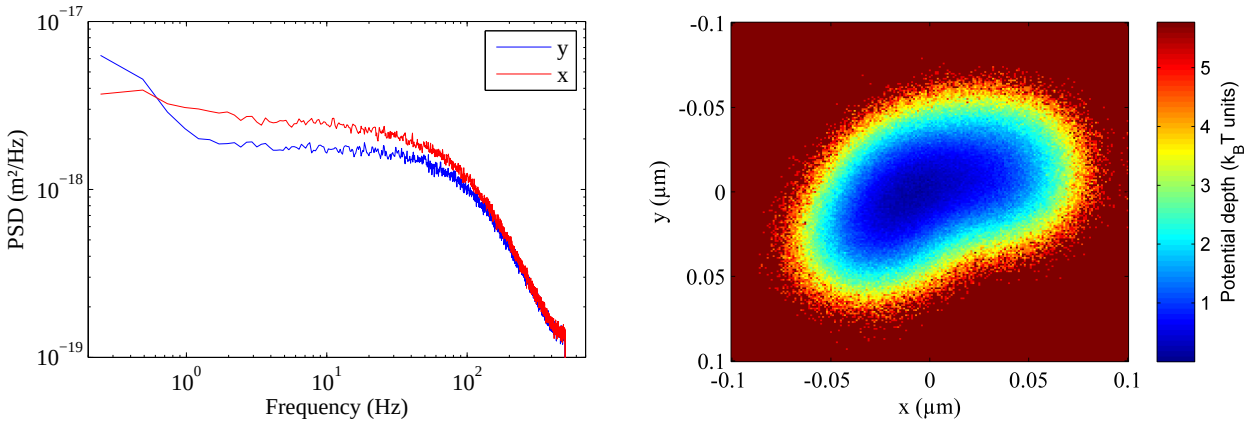

(a) x and y PSDs

(b) Trapping potential

Figure 5.16: a) Measured Power Spectral Densities of x and y-displacement of the trapped particle in the fluid flow. b) Trapping potential estimated by the distribution of particle's positions.

[6]The increase of the stiffness results in an increase of the characteristic frequency of the trapped particle $f_c = k/(2\pi\gamma)$, which may be a problem if the tracking speed is too low.

[7]When a valve is manually closed or opened, the vibrations induced in the system are big enough for the bead to escape the optical trap.

5.4 Conclusion and perspectives

In conclusion, we built microfluidic cells to create a shear-flow with a zero-mean velocity at the micro-scale, and we developed a way to simulate a shear-flow on a trapped particle with the use of an acousto-optic deflector (AOD).

All the final goals of this experiment were not achieved before the writing of this Thesis, but we have already shown that a shear-flow can be seen as an external coloured noise acting on the trapped particle in one direction (called x in this chapter). The coloured noise has a cut-off frequency equal to the typical cut-off frequency of the particle's motion, which is very visible in the Power Spectral Density (PSD) of x. This non-equilibrium steady-state situation results in a clear violation of the Fluctuation Dissipation Theorem (FDT). However, this violation cannot be interpreted as an effective temperature because the relation between the response function and the auto-correlation function is not linear.

The shear-flow can also be a good candidate to test the Harada-Sasa equality [73] linking the violation of the FDT to the amount of energy dissipated by the system. Indeed, to measure the energy dissipated, one has to know the forces that are acting on the particle. Conveniently, in a "real" shear-flow, the external force acting on the x-displacement is only proportional to the y-displacement and can then easily be measured. In the case of the "effective" shear-flow, it would of course also be easy to measure the random signal sent to the AOD.

Finally, if we design and construct a microfluidic cell with the good hydrodynamic properties, we will then be able to compare the analytical results from the coupling model (which is solvable), the results from the "effective" shear-flow, and the results from the real shear-flow, which should be interesting.

Conclusion

In conclusion, we have used different configurations of multiple optical traps as a tool to address some basic research questions in statistical physics of small systems. This kind of set-up opens a lot of experimental possibilities: the ability to control the position of one trap on a wide range of frequencies allows for creating complex trap shapes, as a double well potential or a toroidal trap. It also allows for trapping several micro-particles at the same time, and for adding external noises on particles positions. Even in simple Newtonian fluids like water, the physics of the created situations can be very rich, and we only tested a small number of them:

- In chapter 2 we created a 1-bit memory system with a single particle in a double well potential. By adding an external drag force, which is created by displacing the fluid with respect to the trap position, we realised a memory erasure procedure. This procedure resets the system to a chosen state (state 0), regardless of its initial state (0 or 1), and is characterised by a proportion of success. We measured the stochastic heat associated to this logically irreversible procedure, and we have shown that it approaches the Landauer's bound $k_{\mathrm{B}}T\ln 2$ in average for long procedure durations. We also used a detailed version of the Jarzynski equality to retrieve the Landauer's bound for any procedure duration. Finally we have linked the stochastic work received during each sub-procedure ($1 \to 0$ and $0 \to 0$) to the probability that the system returns to its initial state under a time-reversed procedure.

- In chapter 3 we were interested in studying the interactions between two particles trapped nearby at different effective temperatures. We used the sol-gel transition of a gelatine solution because it was previously shown that a bead trapped in gelatine exhibits anomalous high fluctuations when the sample is locally quenched below the gelation temperature. In the end, we have shown that there is no anomalous effect observed when a small droplet of gelatine is quenched. The Probability Distribution Function (PDF) of the trapped particle's positions shows equilibrium-like properties along the sol-gel transition and the Fluctuation Dissipation Theorem (FDT) seems, within experimental errors, to remain valid during this transient dynamics. We have provided some possible explanations for the effects previously seen, and we used another system to study particles at different effective temperatures.

- In chapter 4 we used an Acousto-Optic Deflector (AOD) to modulate the position of one trap to add an external white noise on the trapped particle, which creates an effective temperature. We then studied the hydrodynamic interactions of two particles trapped

nearby, when one is at the fluid equilibrium temperature whereas the other is forced at a high effective temperature. We computed the variances, cross-variances and position cross-correlation functions with an analytic model, and have found a good agreement with the measurements. We also computed the heat exchanged between the two particles, and have shown that the mean heat flux is proportional to the effective temperature difference between the two particles, as it would be in a system with a real temperature gradient. We measured the Probability Distribution Functions (PDF) of the heat to see if an exchange Fluctuation Theorem (xFT) could be applied, but the experimental data have not yet allowed us to conclude on its validity.

- In chapter 5 we constructed microfluidic cells designed to create a shear-flow with zero-mean velocity. The idea was to use the shear-flow as a physical source of coloured noise for the trapped particle. We have not yet achieved a fully functional microfluidic cell, but we built some encouraging prototypes. We have also shown that we can mimic a shear-flow with the use of an Acousto-Optic Deflector (AOD) in the same way that we created an effective temperature in chapter 4. With this "effective" shear-flow, we have observed a very clear violation of the Fluctuation-Dissipation Theorem (FDT) that cannot be interpreted as an effective temperature because the relation between the response function and the auto-correlation function is not linear.

We believe that our work can easily be extended and that some questions remain unanswered. For example, the effect of an effective temperature acting on one particle can be experimentally tested in more complex geometries, as arrays or lines of particles. It would also be interesting to compute the theoretical Probability Distributions (PDF) of the heat and work exchanged between two hydrodynamically coupled particles kept at different temperatures, to see if the exchange Fluctuation Theorem (xFT) is verified when the forcing becomes larger than the thermal fluctuations. Our work on the shear-flow could also give interesting results if we manage to build a cell without defects that could be use to effectively create a controllable shear-flow. For example, we could test in this system the application of the Harada-Sasa relation, that links the violation of the Fluctuation-Dissipation Theorem to the energy dissipated by the system. Finally, we are convinced that a lot of other configurations can be created by using multiple optical traps to study (out-of) equilibrium statistical physics of small systems.

Bibliography

[1] T. Lucretius Carus, *De rerum natura*. Circa 60 BC. English translation: *On the Nature of Things* by A. M. Esolen, The Johns Hopkins Univ. Pr. (1995).

[2] R. Brown, "A brief account of microscopical observations made in the months of june, july, and august, 1827 on the particles contained in the pollen of plants, and on the general existence of active molecules in organic and inorganic bodies," *The miscellaneous botanical works of Robert Brown*, vol. 1, 1828.

[3] A. Einstein, "Über die von der molekularkinetischen theorie der wärme geforderte bewegung von in ruhenden flüssigkeiten suspendierten teilchen," *Annalen der Physik*, vol. 322, no. 8, pp. 549–560, 1905. English translation in *Investigations on the Theory of the Brownian Movement* (Dover Publication, Inc.).

[4] M. von Smoluchowski, "Zur kinetischen theorie der brownschen molekularbewegung und der suspensionen," *Annalen der Physik*, vol. 326, no. 14, pp. 756–780, 1906.

[5] P. Langevin, "Sur la théorie du mouvement brownien," *C. R. Acad. Sci. (Paris)*, vol. 146, pp. 530–533, 1908. English translation in *American Journal of Physics*, vol. 6, pp. 1079-1081 (1997).

[6] J. Perrin, *Les atomes*. Librairie Félix Alcan, 1913.

[7] A. Ashkin, "Acceleration and trapping of particles by radiation pressure," *Phys. Rev. Lett.*, vol. 24, pp. 156–159, Jan 1970.

[8] D. G. Grier, "A revolution in optical manipulation," *Nature*, vol. 424, no. 6950, pp. 810–816, 2003.

[9] M. J. Padgett, J. Molloy, and D. McGloin, *Optical Tweezers: methods and applications*. CRC Press, 2010.

[10] K. C. Neuman and S. M. Block, "Optical trapping," *Review of scientific instruments*, vol. 75, no. 9, pp. 2787–2809, 2004.

[11] A. Ashkin and J. M. Dziedzic, "Optical levitation by radiation pressure," *Applied Physics Letters*, vol. 19, no. 8, pp. 283–285, 1971.

[12] A. Ashkin, J. M. Dziedzic, J. E. Bjorkholm, and S. Chu, "Observation of a single-beam gradient force optical trap for dielectric particles," *Opt. Lett.*, vol. 11, pp. 288–290, May 1986.

[13] A. Ashkin, "Forces of a single-beam gradient laser trap on a dielectric sphere in the ray optics regime," *Biophysical Journal*, vol. 61, no. 2, pp. 569 – 582, 1992.

[14] R. Simmons, J. Finer, S. Chu, and J. Spudich, "Quantitative measurements of force and displacement using an optical trap," *Biophysical Journal*, vol. 70, no. 4, pp. 1813 – 1822, 1996.

[15] T. Tlusty, A. Meller, and R. Bar-Ziv, "Optical gradient forces of strongly localized fields," *Phys. Rev. Lett.*, vol. 81, pp. 1738–1741, Aug 1998.

[16] E. Dufresne, G. Spalding, M. Dearing, S. Sheets, and D. Grier, "Computer-generated holographic optical tweezer arrays," *REVIEW OF SCIENTIFIC INSTRUMENTS*, vol. 72, pp. 1810–1816, MAR 2001.

[17] J. E. Curtis, B. A. Koss, and D. G. Grier, "Dynamic holographic optical tweezers," *Optics Communications*, vol. 207, no. 1–6, pp. 169 – 175, 2002.

[18] G. C. Spalding, J. Courtial, and R. D. Leonardo, "Chapter 6 - holographic optical tweezers," in *Structured Light and Its Applications* (D. L. Andrews, ed.), pp. 139 – 168, Burlington: Academic Press, 2008.

[19] D. Blair and E. Dufresne, "The matlab particle tracking code repository." http://site.physics.georgetown.edu/matlab/.

[20] J. C. Crocker and E. R. Weeks, "Particle tracking using idl." http://www.physics.emory.edu/faculty/weeks//idl/.

[21] J. C. Crocker and D. G. Grier, "Methods of digital video microscopy for colloidal studies," *Journal of Colloid and Interface Science*, vol. 179, no. 1, pp. 298 – 310, 1996.

[22] S. Toyabe, T. Sagawa, M. Ueda, E. Muneyuki, and M. Sano, "Experimental demonstration of information-to-energy conversion and validation of the generalized jarzynski equality," *Nature Physics*, vol. 6, no. 12, pp. 988–992, 2010.

[23] K. Berg-Sørensen and H. Flyvbjerg, "Power spectrum analysis for optical tweezers," *Review of Scientific Instruments*, vol. 75, no. 3, pp. 594–612, 2004.

[24] M. Fischer, A. C. Richardson, S. N. S. Reihani, L. B. Oddershede, and K. Berg-Sørensen, "Active-passive calibration of optical tweezers in viscoelastic media," *Review of Scientific Instruments*, vol. 81, no. 1, pp. –, 2010.

[25] H. Faxén, "Der widerstand gegen die bewegung einer starren kugel in einer zähen flüssigkeit, die zwischen zwei parallelen ebenen wänden eingeschlossen ist," *Annalen der Physik*, vol. 373, no. 10, pp. 89–119, 1922.

[26] S. Kim and S. Karrila, *Microhydrodynamics: Principles and Selected Applications*. Butterworth - Heinemann series in chemical engineering, Dover Publications, 2005.

[27] J. Leach, H. Mushfique, S. Keen, R. Di Leonardo, G. Ruocco, J. M. Cooper, and M. J. Padgett, "Comparison of faxén's correction for a microsphere translating or rotating near a surface," *Phys. Rev. E*, vol. 79, p. 026301, Feb 2009.

[28] K. C. Vermeulen, G. J. L. Wuite, G. J. M. Stienen, and C. F. Schmidt, "Optical trap stiffness in the presence and absence of spherical aberrations," *Appl. Opt.*, vol. 45, pp. 1812–1819, Mar 2006.

[29] K. Sekimoto, *Stochastic energetics*, vol. 799. Springer, 2010.

[30] K. Sekimoto, "Langevin equation and thermodynamics," *Progress of Theoretical Physics Supplement*, vol. 130, pp. 17–27, 1998.

[31] U. Seifert, "Stochastic thermodynamics, fluctuation theorems and molecular machines," *Reports on Progress in Physics*, vol. 75, no. 12, p. 126001, 2012.

[32] R. Kubo, "The fluctuation-dissipation theorem," *Reports on Progress in Physics*, vol. 29, no. 1, p. 255, 1966.

[33] C. Jarzynski, "Nonequilibrium equality for free energy differences," *Phys. Rev. Lett.*, vol. 78, pp. 2690–2693, Apr 1997.

[34] C. Jarzynski, "Equilibrium free-energy differences from nonequilibrium measurements: A master-equation approach," *Phys. Rev. E*, vol. 56, pp. 5018–5035, Nov 1997.

[35] G. E. Crooks, "Entropy production fluctuation theorem and the nonequilibrium work relation for free energy differences," *Phys. Rev. E*, vol. 60, pp. 2721–2726, Sep 1999.

[36] G. E. Crooks, "Path-ensemble averages in systems driven far from equilibrium," *Phys. Rev. E*, vol. 61, pp. 2361–2366, Mar 2000.

[37] R. van Zon and E. G. D. Cohen, "Extension of the fluctuation theorem," *Phys. Rev. Lett.*, vol. 91, p. 110601, Sep 2003.

[38] R. Landauer, "Irreversibility and heat generation in the computing process," *IBM journal of research and development*, vol. 5, no. 3, pp. 183–191, 1961.

[39] L. Brillouin, *Science and information theory.* Academic Press, Inc., New York, 1956.

[40] O. Penrose, *Foundations of statistical mechanics: a deductive treatment.* Pergamon Press, Oxford, 1970.

[41] C. H. Bennett, "The thermodynamics of computation—a review," *International Journal of Theoretical Physics*, vol. 21, no. 12, pp. 905–940, 1982.

[42] L. Szilard, "Über die entropieverminderung in einem thermodynamischen system bei eingriffen intelligenter wesen," *Zeitschrift für Physik*, vol. 53, no. 11-12, pp. 840–856, 1929. English translation "On the decrease of entropy in a thermodynamic system by the intervention of intelligent beings" in *Behavioral Science*, vol. 9, no. 4, pp. 301–310, 1964.

[43] H. S. Leff and A. F. Rex, *Maxwell's demon: entropy, information, computing.* Princeton University Press, 1990.

[44] H. Leff and A. F. Rex, *Maxwell's Demon 2 Entropy, Classical and Quantum Information, Computing*. CRC Press, 2002.

[45] J. M. Parrondo, J. M. Horowitz, and T. Sagawa, "Thermodynamics of information," *Nature Physics*, vol. 11, no. 2, pp. 131–139, 2015.

[46] K. Shizume, "Heat generation required by information erasure," *Phys. Rev. E*, vol. 52, pp. 3495–3499, Oct 1995.

[47] R. Dillenschneider and E. Lutz, "Memory erasure in small systems," *Phys. Rev. Lett.*, vol. 102, p. 210601, May 2009.

[48] A. Bérut, A. Arakelyan, A. Petrosyan, S. Ciliberto, R. Dillenschneider, and E. Lutz, "Experimental verification of landauer's principle linking information and thermodynamics," *Nature*, vol. 483, no. 7388, pp. 187–189, 2012.

[49] A. Bérut, A. Petrosyan, and S. Ciliberto, "Detailed jarzynski equality applied to a logically irreversible procedure," *EPL (Europhysics Letters)*, vol. 103, no. 6, p. 60002, 2013.

[50] É. Roldán, I. A. Martínez, J. M. Parrondo, and D. Petrov, "Universal features in the energetics of symmetry breaking," *Nature Physics*, vol. 10, no. 6, pp. 457–461, 2014.

[51] Y. Jun, M. c. v. Gavrilov, and J. Bechhoefer, "High-precision test of landauer's principle in a feedback trap," *Phys. Rev. Lett.*, vol. 113, p. 190601, Nov 2014.

[52] H. Kramers, "Brownian motion in a field of force and the diffusion model of chemical reactions," *Physica*, vol. 7, no. 4, pp. 284 – 304, 1940.

[53] K. Sekimoto and S.-i. Sasa, "Complementarity relation for irreversible process derived from stochastic energetics," *Journal of the Physical Society of Japan*, vol. 66, no. 11, pp. 3326–3328, 1997.

[54] S. Vaikuntanathan and C. Jarzynski, "Dissipation and lag in irreversible processes," *EPL (Europhysics Letters)*, vol. 87, no. 6, p. 60005, 2009.

[55] R. Kawai, J. M. R. Parrondo, and C. V. den Broeck, "Dissipation: The phase-space perspective," *Phys. Rev. Lett.*, vol. 98, p. 080602, Feb 2007.

[56] E. Aurell, K. Gawędzki, C. Mejía-Monasterio, R. Mohayaee, and P. Muratore-Ginanneschi, "Refined second law of thermodynamics for fast random processes," *Journal of statistical physics*, vol. 147, no. 3, pp. 487–505, 2012.

[57] K. te Nijenhuis, *Thermoreversible networks: viscoelastic properties and structure of gels*. Advances in polymer science, Springer, 1997.

[58] M. Djabourov, J. Leblond, and P. Papon, "Gelation of aqueous gelatin solutions. i. structural investigation," *Journal de physique*, vol. 49, no. 2, pp. 319–332, 1988.

[59] M. Djabourov, J. Leblond, and P. Papon, "Gelation of aqueous gelatin solutions. ii. rheology of the sol-gel transition," *Journal de Physique*, vol. 49, no. 2, pp. 333–343, 1988.

[60] H. B. Bohidar and S. S. Jena, "Kinetics of sol–gel transition in thermoreversible gelation of gelatin," *The Journal of Chemical Physics*, vol. 98, no. 11, pp. 8970–8977, 1993.

[61] H. B. Bohidar and S. S. Jena, "Study of sol-state properties of aqueous gelatin solutions," *The Journal of Chemical Physics*, vol. 100, no. 9, pp. 6888–6895, 1994.

[62] O. Ronsin, C. Caroli, and T. Baumberger, "Interplay between shear loading and structural aging in a physical gelatin gel," *Phys. Rev. Lett.*, vol. 103, p. 138302, Sep 2009.

[63] A. Parker and V. Normand, "Glassy dynamics of gelatin gels," *Soft Matter*, vol. 6, pp. 4916–4919, 2010.

[64] J. R. Gomez-Solano, *Nonequilibrium fluctuations of a Brownian particle*. Theses, École normale supérieure de lyon - ENS LYON, Nov. 2011. Available at https://tel.archives-ouvertes.fr/tel-00648099.

[65] J. R. Gomez-Solano, A. Petrosyan, and S. Ciliberto, "Heat fluctuations in a nonequilibrium bath," *Phys. Rev. Lett.*, vol. 106, p. 200602, May 2011.

[66] J. R. Gomez-Solano, A. Petrosyan, and S. Ciliberto, "Fluctuations, linear response and heat flux of an aging system," *EPL (Europhysics Letters)*, vol. 98, no. 1, p. 10007, 2012.

[67] V. Normand, S. Muller, J.-C. Ravey, and A. Parker, "Gelation kinetics of gelatin: A master curve and network modeling," *Macromolecules*, vol. 33, no. 3, pp. 1063–1071, 2000.

[68] E. J. Peterman, F. Gittes, and C. F. Schmidt, "Laser-induced heating in optical traps," *Biophysical journal*, vol. 84, no. 2, pp. 1308–1316, 2003.

[69] K. F. Palmer and D. Williams, "Optical properties of water in the near infrared," *J. Opt. Soc. Am.*, vol. 64, pp. 1107–1110, Aug 1974.

[70] J.-C. Meiners and S. R. Quake, "Direct measurement of hydrodynamic cross correlations between two particles in an external potential," *Phys. Rev. Lett.*, vol. 82, pp. 2211–2214, Mar 1999.

[71] D. Mizuno, D. A. Head, F. C. MacKintosh, and C. F. Schmidt, "Active and passive microrheology in equilibrium and nonequilibrium systems," *Macromolecules*, vol. 41, no. 19, pp. 7194–7202, 2008.

[72] G. Pesce, A. C. D. Luca, G. Rusciano, P. A. Netti, S. Fusco, and A. Sasso, "Microrheology of complex fluids using optical tweezers: a comparison with macrorheological measurements," *Journal of Optics A: Pure and Applied Optics*, vol. 11, no. 3, p. 034016, 2009.

[73] T. Harada and S.-i. Sasa, "Equality connecting energy dissipation with a violation of the fluctuation-response relation," *Phys. Rev. Lett.*, vol. 95, p. 130602, Sep 2005.

[74] G. Verley and D. Lacoste, "Fluctuation theorems and inequalities generalizing the second law of thermodynamics out of equilibrium," *Phys. Rev. E*, vol. 86, p. 051127, Nov 2012.

[75] N. Wiener, "Generalized harmonic analysis," *Acta Mathematica*, vol. 55, no. 1, pp. 117–258, 1930.

[76] A. Khintchine, "Korrelationstheorie der stationären stochastischen prozesse," *Mathematische Annalen*, vol. 109, no. 1, pp. 604–615, 1934.

[77] P. Jop, J. R. Gomez-Solano, A. Petrosyan, and S. Ciliberto, "Experimental study of out-of-equilibrium fluctuations in a colloidal suspension of laponite using optical traps," *Journal of Statistical Mechanics: Theory and Experiment*, vol. 2009, no. 04, p. P04012, 2009.

[78] N. Greinert, T. Wood, and P. Bartlett, "Measurement of effective temperatures in an aging colloidal glass," *Phys. Rev. Lett.*, vol. 97, p. 265702, Dec 2006.

[79] I. A. Martínez, E. Roldán, J. M. R. Parrondo, and D. Petrov, "Effective heating to several thousand kelvins of an optically trapped sphere in a liquid," *Phys. Rev. E*, vol. 87, p. 032159, Mar 2013.

[80] T. Bodineau and B. Derrida, "Current fluctuations in nonequilibrium diffusive systems: An additivity principle," *Phys. Rev. Lett.*, vol. 92, p. 180601, May 2004.

[81] C. Jarzynski and D. K. Wójcik, "Classical and quantum fluctuation theorems for heat exchange," *Phys. Rev. Lett.*, vol. 92, p. 230602, Jun 2004.

[82] C. Van den Broeck, R. Kawai, and P. Meurs, "Microscopic analysis of a thermal brownian motor," *Phys. Rev. Lett.*, vol. 93, p. 090601, Aug 2004.

[83] P. Visco, "Work fluctuations for a brownian particle between two thermostats," *Journal of Statistical Mechanics: Theory and Experiment*, vol. 2006, no. 06, p. P06006, 2006.

[84] D. J. Evans, D. J. Searles, and S. R. Williams, "On the probability of violations of fourier's law for heat flow in small systems observed for short times," *The Journal of Chemical Physics*, vol. 132, no. 2, pp. –, 2010.

[85] A. Crisanti, A. Puglisi, and D. Villamaina, "Nonequilibrium and information: The role of cross correlations," *Phys. Rev. E*, vol. 85, p. 061127, Jun 2012.

[86] K. Saito and A. Dhar, "Fluctuation theorem in quantum heat conduction," *Phys. Rev. Lett.*, vol. 99, p. 180601, Oct 2007.

[87] D. Andrieux, P. Gaspard, T. Monnai, and S. Tasaki, "The fluctuation theorem for currents in open quantum systems," *New Journal of Physics*, vol. 11, no. 4, p. 043014, 2009.

[88] M. Campisi, P. Hänggi, and P. Talkner, "*Colloquium* : Quantum fluctuation relations: Foundations and applications," *Rev. Mod. Phys.*, vol. 83, pp. 771–791, Jul 2011.

[89] S. Ciliberto, A. Imparato, A. Naert, and M. Tanase, "Statistical properties of the energy exchanged between two heat baths coupled by thermal fluctuations," *Journal of Statistical Mechanics: Theory and Experiment*, vol. 2013, no. 12, p. P12014, 2013.

[90] J. Koski, T. Sagawa, O. Saira, Y. Yoon, A. Kutvonen, P. Solinas, M. Möttönen, T. Ala-Nissila, and J. Pekola, "Distribution of entropy production in a single-electron box," *Nature Physics*, vol. 9, no. 10, pp. 644–648, 2013.

[91] M. Stimson and G. Jeffery, "The motion of two spheres in a viscous fluid," *Proceedings of the Royal Society of London. Series A, Containing Papers of a Mathematical and Physical Character*, pp. 110–116, 1926.

[92] G. K. Batchelor, "Brownian diffusion of particles with hydrodynamic interaction," *Journal of Fluid Mechanics*, vol. 74, pp. 1–29, 3 1976.

[93] J. Happel and H. Brenner, "Interaction between two, or more particles," in *Low Reynolds number hydrodynamics*, vol. 1 of *Mechanics of fluids and transport processes*, pp. 235–285, Springer Netherlands, 1983.

[94] D. J. Jeffrey and Y. Onishi, "Calculation of the resistance and mobility functions for two unequal rigid spheres in low-reynolds-number flow," *Journal of Fluid Mechanics*, vol. 139, pp. 261–290, 2 1984.

[95] J. C. Crocker, "Measurement of the hydrodynamic corrections to the brownian motion of two colloidal spheres," *The Journal of Chemical Physics*, vol. 106, no. 7, pp. 2837–2840, 1997.

[96] E. R. Dufresne, T. M. Squires, M. P. Brenner, and D. G. Grier, "Hydrodynamic coupling of two brownian spheres to a planar surface," *Phys. Rev. Lett.*, vol. 85, pp. 3317–3320, Oct 2000.

[97] J.-C. Meiners and S. R. Quake, "Direct measurement of hydrodynamic cross correlations between two particles in an external potential," *Phys. Rev. Lett.*, vol. 82, pp. 2211–2214, Mar 1999.

[98] P. Bartlett, S. I. Henderson, and S. J. Mitchell, "Measurement of the hydrodynamic forces between two polymer–coated spheres," *Philosophical Transactions of the Royal Society of London A: Mathematical, Physical and Engineering Sciences*, vol. 359, no. 1782, pp. 883–895, 2001.

[99] L. A. Hough and H. D. Ou-Yang, "Correlated motions of two hydrodynamically coupled particles confined in separate quadratic potential wells," *Phys. Rev. E*, vol. 65, p. 021906, Jan 2002.

[100] H. Dong-Hui, Y. Tao, L. Wei-Hua, Z. Qing-Lan, and M. Hong-Ru, "Brownian dynamics simulation of two confined colloidal particles," *Chinese Physics*, vol. 16, no. 10, p. 3138, 2007.

[101] R. Di Leonardo, S. Keen, J. Leach, C. D. Saunter, G. D. Love, G. Ruocco, and M. J. Padgett, "Eigenmodes of a hydrodynamically coupled micron-size multiple-particle ring," *Phys. Rev. E*, vol. 76, p. 061402, Dec 2007.

[102] G. M. Cicuta, J. Kotar, A. T. Brown, J.-H. Noh, and P. Cicuta, "Hydrodynamic coupling in polygonal arrays of colloids: Experimental and analytical results," *Phys. Rev. E*, vol. 81, p. 051403, May 2010.

[103] S. Herrera-Velarde, E. C. Euán-Díaz, F. Córdoba-Valdés, and R. Castañeda-Priego, "Hydrodynamic correlations in three-particle colloidal systems in harmonic traps," *Journal of Physics: Condensed Matter*, vol. 25, no. 32, p. 325102, 2013.

[104] M. Polin, D. G. Grier, and S. R. Quake, "Anomalous vibrational dispersion in holographically trapped colloidal arrays," *Phys. Rev. Lett.*, vol. 96, p. 088101, Mar 2006.

[105] J. Kotar, M. Leoni, B. Bassetti, M. C. Lagomarsino, and P. Cicuta, "Hydrodynamic synchronization of colloidal oscillators," *Proceedings of the National Academy of Sciences*, vol. 107, no. 17, pp. 7669–7673, 2010.

[106] A. Curran, M. P. Lee, M. J. Padgett, J. M. Cooper, and R. Di Leonardo, "Partial synchronization of stochastic oscillators through hydrodynamic coupling," *Phys. Rev. Lett.*, vol. 108, p. 240601, Jun 2012.

[107] N. Koumakis and R. Di Leonardo, "Stochastic hydrodynamic synchronization in rotating energy landscapes," *Phys. Rev. Lett.*, vol. 110, p. 174103, Apr 2013.

[108] J. Kotar, L. Debono, N. Bruot, S. Box, D. Phillips, S. Simpson, S. Hanna, and P. Cicuta, "Optimal hydrodynamic synchronization of colloidal rotors," *Phys. Rev. Lett.*, vol. 111, p. 228103, Nov 2013.

[109] Y. Sokolov, D. Frydel, D. G. Grier, H. Diamant, and Y. Roichman, "Hydrodynamic pair attractions between driven colloidal particles," *Phys. Rev. Lett.*, vol. 107, p. 158302, Oct 2011.

[110] Y. Sassa, S. Shibata, Y. Iwashita, and Y. Kimura, "Hydrodynamically induced rhythmic motion of optically driven colloidal particles on a ring," *Phys. Rev. E*, vol. 85, p. 061402, Jun 2012.

[111] J. R. Gomez-Solano, L. Bellon, A. Petrosyan, and S. Ciliberto, "Steady-state fluctuation relations for systems driven by an external random force," *EPL (Europhysics Letters)*, vol. 89, no. 6, p. 60003, 2010.

[112] A. Bérut, A. Petrosyan, and S. Ciliberto, "Energy flow between two hydrodynamically coupled particles kept at different effective temperatures," *EPL (Europhysics Letters)*, vol. 107, no. 6, p. 60004, 2014.

[113] M. Doi and S. F. Edwards, *The Theory of Polymer Dynamics*. International series of monographs on physics, Clarendon Press, 1988.

[114] R. Zwanzig, *Nonequilibrium Statistical Mechanics*. Oxford University Press, USA, 2001.

[115] J. Farago, "Injected power fluctuations in langevin equation," *Journal of Statistical Physics*, vol. 107, no. 3-4, pp. 781–803, 2002.

[116] T. Li, S. Kheifets, and M. G. Raizen, "Millikelvin cooling of an optically trapped microsphere in vacuum," *Nature Physics*, vol. 7, no. 7, pp. 527–530, 2011.

[117] J. Gieseler, B. Deutsch, R. Quidant, and L. Novotny, "Subkelvin parametric feedback cooling of a laser-trapped nanoparticle," *Phys. Rev. Lett.*, vol. 109, p. 103603, Sep 2012.

[118] C. Van Den Broeck, J. M. Sancho, and M. San Miguel, "Harmonically bound brownian motion in flowing fluids," *Physica A: Statistical Mechanics and its Applications*, vol. 116, no. 3, pp. 448 – 461, 1982.

[119] T. van de Ven, "Diffusion of brownian particles in shear flow," *Journal of Colloid and Interface Science*, vol. 62, no. 2, pp. 352 – 355, 1977.

[120] M. S. Miguel and J. Sancho, "Brownian motion in shear flow," *Physica A: Statistical Mechanics and its Applications*, vol. 99, no. 1–2, pp. 357 – 364, 1979.

[121] Y. Drossinos and M. W. Reeks, "Brownian motion of finite-inertia particles in a simple shear flow," *Phys. Rev. E*, vol. 71, p. 031113, Mar 2005.

[122] H. Orihara and Y. Takikawa, "Brownian motion in shear flow: Direct observation of anomalous diffusion," *Phys. Rev. E*, vol. 84, p. 061120, Dec 2011.

[123] J.-L. Barrat and L. Berthier, "Fluctuation-dissipation relation in a sheared fluid," *Phys. Rev. E*, vol. 63, p. 012503, Dec 2000.

[124] L. Berthier and J.-L. Barrat, "Nonequilibrium dynamics and fluctuation-dissipation relation in a sheared fluid," *The Journal of Chemical Physics*, vol. 116, no. 14, pp. 6228–6242, 2002.

[125] A. Ziehl, J. Bammert, L. Holzer, C. Wagner, and W. Zimmermann, "Direct measurement of shear-induced cross-correlations of brownian motion," *Phys. Rev. Lett.*, vol. 103, p. 230602, Dec 2009.

[126] L. Holzer, J. Bammert, R. Rzehak, and W. Zimmermann, "Dynamics of a trapped brownian particle in shear flows," *Phys. Rev. E*, vol. 81, p. 041124, Apr 2010.

[127] D. Kienle, J. Bammert, and W. Zimmermann, "Shear-flow-enhanced barrier crossing," *Phys. Rev. E*, vol. 84, p. 042102, Oct 2011.

[128] B. Lander, U. Seifert, and T. Speck, "Mobility and diffusion of a tagged particle in a driven colloidal suspension," *EPL (Europhysics Letters)*, vol. 92, no. 5, p. 58001, 2010.

[129] B. Lander, U. Seifert, and T. Speck, "Effective confinement as origin of the equivalence of kinetic temperature and fluctuation-dissipation ratio in a dense shear-driven suspension," *Phys. Rev. E*, vol. 85, p. 021103, Feb 2012.

[130] D. Bartolo, G. Degre, P. Nghe, and V. Studer, "Microfluidic stickers," *Lab Chip*, vol. 8, pp. 274–279, 2008.

[131] B. Levaché, *Imbibition dynamics in confined media.* Theses, Université Pierre et Marie Curie - Paris VI, Mar. 2014. Available at https://pastel.archives-ouvertes.fr/pastel-00966910.

[132] D. C. Duffy, J. C. McDonald, O. J. A. Schueller, and G. M. Whitesides, "Rapid prototyping of microfluidic systems in poly(dimethylsiloxane)," *Analytical Chemistry*, vol. 70, no. 23, pp. 4974–4984, 1998. PMID: 21644679.

[133] J. C. McDonald, D. C. Duffy, J. R. Anderson, D. T. Chiu, H. Wu, O. J. A. Schueller, and G. M. Whitesides, "Fabrication of microfluidic systems in poly(dimethylsiloxane)," *ELECTROPHORESIS*, vol. 21, no. 1, pp. 27–40, 2000.

[134] J. C. McDonald and G. M. Whitesides, "Poly(dimethylsiloxane) as a material for fabricating microfluidic devices," *Accounts of Chemical Research*, vol. 35, no. 7, pp. 491–499, 2002. PMID: 12118988.

[135] S. Bhattacharya, A. Datta, J. Berg, and S. Gangopadhyay, "Studies on surface wettability of poly(dimethyl) siloxane (pdms) and glass under oxygen-plasma treatment and correlation with bond strength," *Microelectromechanical Systems, Journal of*, vol. 14, pp. 590–597, June 2005.

[136] J. Zhou, A. V. Ellis, and N. H. Voelcker, "Recent developments in pdms surface modification for microfluidic devices," *ELECTROPHORESIS*, vol. 31, no. 1, pp. 2–16, 2010.